

BRNO UNIVERSITY OF TECHNOLOGY

VYSOKÉ UČENÍ TECHNICKÉ V BRNĚ

FACULTY OF MECHANICAL ENGINEERING FAKULTA STROJNÍHO INŽENÝRSTVÍ

INSTITUTE OF MATERIALS SCIENCE AND ENGINEERING ÚSTAV MATERIÁLOVÝCH VĚD A INŽENÝRSTVÍ

THEORETICAL STUDY OF MAGNETIC STATES IN ALLOYS WITH DIFFERENT LEVELS OF ORDERING

TEORETICKÉ STUDIUM MAGNETICKÝCH STAVŮ VE SLITINÁCH S RŮZNOU ÚROVNÍ US-POŘÁDÁNÍ

PHD THESIS
DISERTAČNÍ PRÁCE

AUTHOR AUTOR PRÁCE

Ing. PAVEL PAPEŽ

SUPERVISOR

Mgr. MARTIN FRIÁK, Ph.D.

ŠKOLITEL

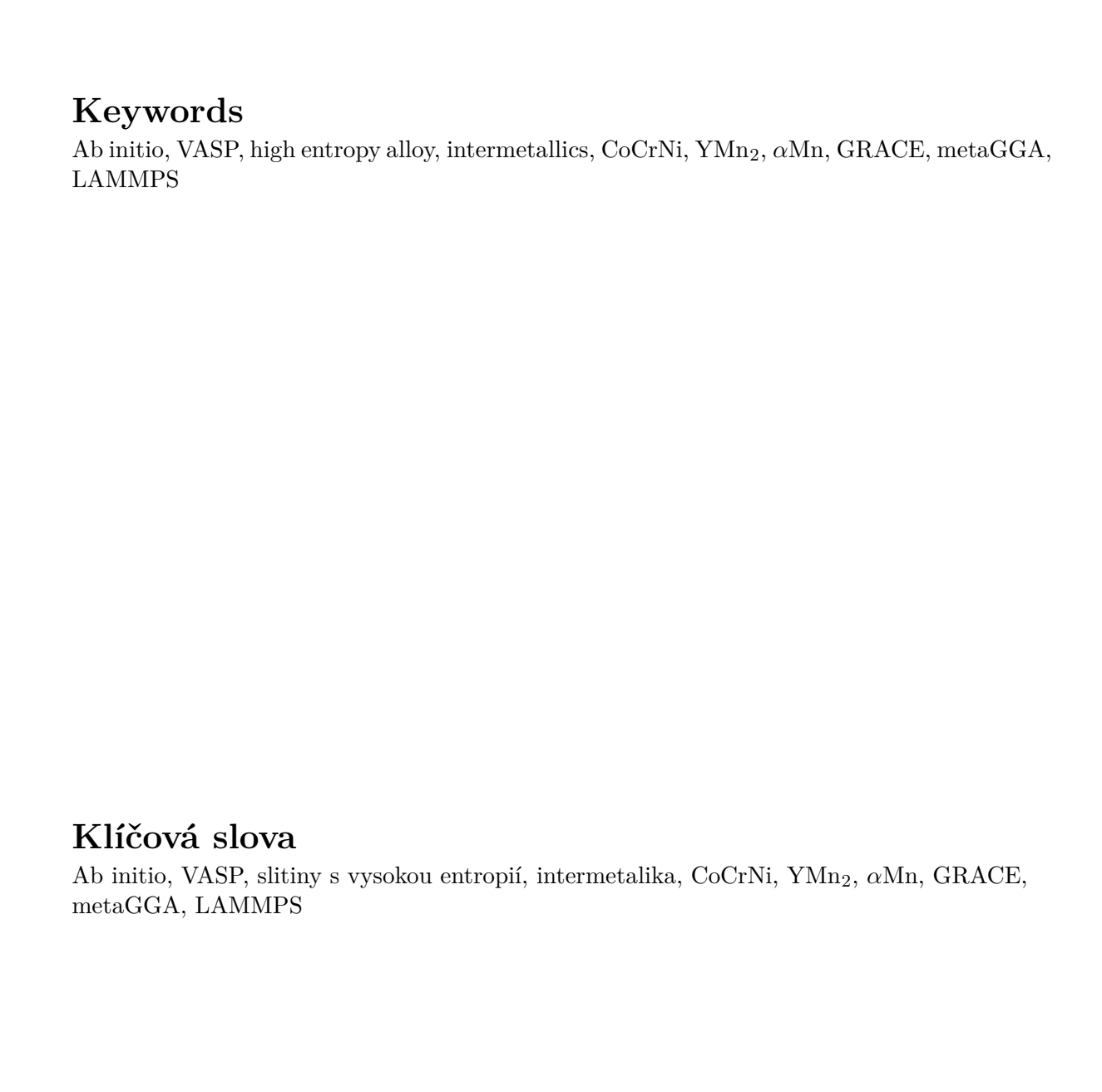
BRNO 2025

Abstract

This work is focused on ab initio study of magnetism in three different materials, high entropy alloy CoCrNi, pure α Mn and intermetallic compound YMn₂. Ab initio methods allow for easy access to materials properties without the need for experimental measurements. All ab initio calculations in this work were done using the Vienna Ab initio Simulation Package (VASP) and the projector augmented waves (PAW) method while the molecular dynamics simulations were done in the program LAMMPS in combination with the GRACE universal machine learned potential. This work employed the ab initio methods to describe the effect of short-range order on magnetic moments, charge transfer and the phase stability in CoCrNi alloy. Some of these results were compared to one of the universal machine learned potential to parse its performance. The relative phase stability was further evaluated by the molecular dynamics simulation to obtain its temperature dependence. Furthermore, different possible magnetic arrangements in the intermetallic compound YMn₂ were calculated in order to find the ground state magnetic arrangements. After successfully obtaining the complicated magnetic structure of pure Mn by metaGGA functional, the same functional was used on YMn₂ as well in order to obtain experimental magnetic structures

Abstrakt

Tato práce se zabývá studiem magnetismu pomocí ab initio metod. Tyto metody umožňují jednoduchý přístup k materiálovým vlastnostem bez nutnosti experimentálních měření. Ab initio výpočty v této práci byly provedeny programem Vienna Ab initio Simulation Package (VASP) pomocí projektovaných přidružených vln (PAW) zatímco výpočty molekulové dynamiky byly provedeny programem LAMMPS v kombinaci s univerzálním potenciálem GRACE. Výpočty byly provedeny na třech materiálech, slitině s vysokou entropií CoCrNi, intermetaliku YM n_2 a základnímu alotropu prvku α Mn. Pro slitinu CoCrNi byly výpočty použity k popisu vlivů uspořádání na krátkou vzdálenost na magnetické momenty a přenos náboje v materiálu. Dále pak byly tyto získané výsledky provázány s fázovou stabilitou této slitiny, jejíž teplotní závislost byla dále simulována pomocí molekulové dynamiky. Také proběhlo porovnání získaných výsledků pomocí ab initio metod s univerzálními potenciály k zjištění jejich přesnosti. Pro intermetalikum YMn₂ byly výpočty provedeny pro několik možných uspořádání magnetických momentů s cílem získat základní stav. Tyto výpočty byly provedeny s nekolineárními magnetickými momenty. Po úspěšném popisu komplikované magnetické struktury čistého Mn pomoci metaGGA funkcionálu byl následně použit na intermetalikum YMn₂ k zisku experimentálně měřených magnetických struktur.



| Declaration | |
|--|-----------------------------|
| Here I declare that the doctoral thesis on Theoretical study of magnetic with different levels of ordering was written independently by myself we sources and literature all listed in references. | |
| | |
| | Pavel Papež June 30 2025 |
| | |
| | |
| | |

Acknowledgements

Firstly I would like to thank my supervisor Mgr. Martin Friák Ph.D. for his support and leadership throughout my doctoral studies and all the fruitful consultations. I would also like to thank my supervisor specialist Ing. Martin Zelený Ph.D. who was always there to offer help with scientific problems that I have encountered throughout my PhD studies.

Another thanks should go to doc. RNDr. Ilja Turek , DrSc. for including me in his project from Czech Science Foundation and providing many helpful consultations. Furthermore, I would like to thank Priv.-Doz. Mgr. David Holec, Ph.D. from Montannuniversität Leoben for a very warm welcome and for making my stay in their research group both possible and very pleasant, even though my coffee addiction just got worse. And, of course, I can not forget to thank my dear friends Ing. Ondřej Fikar Ph.D. and Mgr. Ivana Miháliková for so many helpful conversations and other support throughout the whole doctoral studies. Even more thanks goes to mu friends outside of academic background who had to listen to my rambles that they did not understand at all.

Many thanks also go to my family and girlfriend, who unsuccessfully tried to understand my studies but still supported me. And thanks to my cat Micoušková without who it would be very hard to find the mental strength to continue the studies as well as thanks to all the other cats in cat café Schrödinger, where many days have been spent writing this thesis with their emotional support. Thanks also has to go to all my friends and colleagues at both of the institutes, especially Mgr. Valentína Berecová, Mgr. Dávid Mikšík, Ing. Jakub Judas Ph.D., Ing. Ondřej Adam Ph.D., Ing. Tomáš Straka and Ing. Daniel Valášek, who made them quite nice friendly places instead of just workplaces.

I would also like to gratefully acknowledge the Financial supports from the Czech Academy of Science (the Praemium Academiae awarded to Mgr. Martin Friák, Ph.D., from the Institute of Physics of Materials, v. v. i., Czech Academy of Sciences, in Brno, Czech Republic) and the Czech Science Foundation (Projects Nos. 19-22016S, 22-22187S and 23-04746S). The computational resources were partly provided by the Ministry of Education, Youth and Sports of the Czech Republic under the Projects e-INFRA CZ (ID:90254) at the IT4Innovations (IT4I) National Supercomputing Center in Ostrava (Czech Republic) and e-Infrastruktura CZ (e-INFRA, ID:90254) at the MetaCentrum and the CERIT Scientific Cloud in Brno (CZ). I would also like to acknowledge the Czech Science Foundation, Czechia for awarding this project access to the LUMI supercomputer, owned by the EuroHPC Joint Undertaking, hosted by CSC (Finland) and the LUMI consortium through IT4Innovations, Czechia.

| Bibliographic reference PAPEŽ, Pavel. Theoretical study of magnetic states in alloys with different levels of ordering Online, doctoral Thesis. Martin FRIÁK (supervisor). Brno: Brno University of Technology, Faculty of Mechanical Engineering, 2025. Available at: https://www.vut.cz/en/students/final-thesis/detail/166654. |
|---|
| |

Contents

| 1 | Intr | roduction | 1 |
|---|------------------------|---|----------|
| 2 | Ord | lering in alloys | • |
| | 2.1 | Theory of ordering in alloys | • |
| | 2.2 | Warren-Cowley parameters | 4 |
| 3 | $\mathbf{A}\mathbf{b}$ | initio calculations | ŀ |
| | 3.1 | Density Functional Theory | ļ |
| | | 3.1.1 General description | ٦ |
| | | 3.1.2 Exchange-correlation functionals | 7 |
| | | 9 | 1(|
| | 3.2 | 1 | 10 |
| | J | | 1(|
| | | | 11 |
| | 3.3 | 0 0 | 14 |
| | 0.0 | | 15 |
| | | | 17 |
| | 3.4 | * | 23 |
| | 5.4 | v e | 2: 2: |
| | 3.5 | | 2. 24 |
| | 3.6 | 9 | 25 25 |
| | 5.0 | · | 25 25 |
| | | | |
| | | | 26 |
| | 9.7 | | 27 |
| | 3.7 | 9 | 27 |
| | | | 33 |
| | | 3.7.2 GRACE | 34 |
| 4 | CoC | CrNi alloy calculations | 36 |
| | 4.1 | CoCrNi literature review | 36 |
| | 4.2 | Methods and models | 36 |
| | | 4.2.1 Computational cells | 36 |
| | | 4.2.2 Calculation settings | 38 |
| | | | 36 |
| | | 4.2.4 Optimization using internal coordinates - Gadget tool | 42 |
| | | | 46 |
| | 4.3 | ** | 46 |
| | | | 46 |
| | | · | 48 |
| | | _ | 52 |
| | | | 56 |
| | | 1 | 62 |
| | | | _ |
| 5 | | = | 38 |
| | 5.1 | | 36 |
| | 5.2 | Methods and models | ςc |

| | | 5.2.1 | Models | 69 |
|-------------|-----|---------|--|------------|
| | | 5.2.2 | GGA calculations | 71 |
| | | 5.2.3 | Meta-GGA calculations | 71 |
| 5.3 Results | | | | |
| | | 5.3.1 | GGA results | 73 |
| | | 5.3.2 | Meta-GGA results - α -Mn | 76 |
| | | 5.3.3 | $Meta-GGA\ results\ -\ YMn_2 .\ .\ .\ .\ .\ .\ .$ | 76 |
| 6 | Goa | ıls | | 78 |
| | 6.1 | CoCrN | Ni calculations | 78 |
| | 6.2 | YMn_2 | calculation | 78 |
| 7 | Con | clusio | ns | 7 9 |
| 8 | Pub | licatio | ons and other activities | 82 |
| | 8.1 | Public | eations | 82 |
| | 8.2 | Other | activities | 82 |
| | | 8.2.1 | Conferences | 82 |
| | | 8.2.2 | Workshops and schools | 82 |
| | | 8.2.3 | Research stays | 83 |
| | | | | |

List of Figures

| Difference between intermetallics and solid solution alloy [24] | 3 |
|---|--|
| | |
| | 7 |
| | 13 |
| | 14 |
| | 14 |
| · | 15 |
| , | 18 |
| , | 10 |
| | |
| · · | |
| | |
| | |
| | |
| | |
| | 18 |
| | |
| functionals [39] | 19 |
| | 20 |
| MAPE and MAE in determination of band gaps taken from [46] | 21 |
| Comparison between TASK, SCAN metaGGAs and PBE functional for band | |
| gap accuracy taken from [47] | 21 |
| Comparison between SCAN and PBE in accuracy of magnetic moment pre- | |
| | 22 |
| | |
| | 24 |
| | 26 |
| | |
| | 20 |
| | 30 |
| | 31 33 |
| | Je |
| | 35 |
| • • | |
| | 37 |
| | 37 |
| | 40 |
| · · | 41 |
| • | |
| | 42 |
| | 47 |
| | Jacob's Ladder for Exchange-Correlation Functionals [30] |

| 4.7 | Ni and Co local to average in 1st NN magnetic moments in randomly ordered | |
|------|--|----|
| | structures | 49 |
| 4.8 | Cr magnetic moment distribution in randomly ordered structures | 49 |
| 4.9 | Co and Ni Local to average in 1st NN magnetic moments in ordered structures. | 50 |
| 4.10 | Cr magnetic moment distribution in ordered structures | 51 |
| 4.11 | Magnetic moment dependence on Co in 1st NN shell | 51 |
| 4.12 | Magnetic moment dependence on Cr in 1st NN shell | 52 |
| 4.13 | Magnetic moment dependence on Ni in 1st NN shell | 52 |
| 4.14 | Co charge transfer dependence on 1st NN composition | 53 |
| 4.15 | Cr charge transfer dependence on 1st NN composition | 54 |
| 4.16 | Ni charge transfer dependence on 1st NN composition | 55 |
| 4.17 | Magnetic moment dependence on charge transfer | 56 |
| 4.18 | Comparison between energies obtained via DFT and via CHGNet UMLIP | 57 |
| 4.19 | Errors obtained for all the calculated structures | 58 |
| 4.20 | CHGnet energy predictions | 59 |
| 4.21 | Comparison between forces obtained via DFT and via CHGNet UMLIP | 59 |
| 4.22 | Errors obtained for forces for all the calculated structures | 60 |
| 4.23 | Comparison between magnetic moments obtained via DFT and via CHGNet | |
| | UMLIP | 60 |
| | Errors obtained for magnetic moments for all the calculated structures | 61 |
| | Enthalpy obtained from MD runs | 62 |
| 4.26 | Radial distribution function for fcc | 64 |
| | Common neighbour analysis obtained from MD run at 1100 K for fcc | 65 |
| 4.28 | Radial distribution functions for hcp | 66 |
| 4.29 | Common neighbour analysis obtained from MD run at 1100 K for hcp | 67 |
| 4.30 | CNA visualisations, fcc structure is green, hcp is red, white are the displaced | |
| | atoms, blue is some displacements into bcc structure | 67 |
| 5.1 | Comparison between densities of states via GGA, GGA+U and SCAN for | |
| | pure Mn, taken from [19] | 69 |
| 5.2 | Different antiferromagnetic orderings used for YMn ₂ calculations, purple | |
| | atoms are Mn, turquoise atoms are Y, black vector highlights the [0 0 1] | |
| | crystallographic direction | 70 |
| 5.3 | The α -Mn crystal lattice with the magnetic sublattices differentiated by | |
| | colours, dark blue is the I, orange is the II, light blue and purple are the IIIa | |
| | and IIIb respectively and finally, dark green and dark blue are the IVa and | |
| | IVb sublattices | 71 |
| 5.4 | Results from collinear calculations | 73 |
| 5.5 | YMn_2 energy-volume curves with Birch-Murnaghan equation of states fit | 74 |
| 5.6 | YMn_2 equillibrium energies and volumes | 75 |
| 5.7 | Magnetic moments dependence on volume | 76 |

1. Introduction

Magnetism and magnetic materials play a huge role in modern industry and life. For that it is crucial to understand how can magnetism be influenced and employed. Here we focus on magnetism related to the electrons and their spin moments. Magnetic materials can be divided into basic categories based on the internal ordering of magnetic moments, $e.\ g.$ paramagnetic, ferromagnetic or antiferromagnetic. There are also diamagnetic materials which, instead of having their own specific ordering, orient their magnetic moments to turn against external applied field [1-3].

As we focus on magnetism related to electrons it can be easily accessible by the means of ab initio calculation methods. These methods compute the electronic structure of materials with no need for previous experimental data. The method of ab initio calculations used in this work employed the density functional theory (DFT) which was proposed by Hohenberg, Kohn and Sham in the 1960s. DFT describes a multielectron system as a system of non-interacting electrons employing several approximations. In particular, the electron density of the multielectron system is equal to that of the non-interacting single-electron system [4, 5]. Calculations in this work were done through the Viena Ab initio Simulation Package (VASP) that allows to compute ferromagnetic and antiferromagnetic states. Different noncollinear structures can be computed as well but with the increased computational cost. Paramagnetic materials are usually approximated by a system of disordered collinear states or, alternatively, by non-spin polarised calculations, in other words not considering the spin matrix at all in the calculations and not splitting the electron density into spin-up and spin-down parts [1, 2, 6–8].

This work focuses on two different materials, one of them is a high entropy alloy (HEA) CoCrNi. Sometimes it is reffered to as a medium entropy alloy (MEA) because it is composed of only 3 elements. This group of materials was first described in 2004 by two groups independently [9, 10]. Since then, high entropy alloys have become quite popular in research. They are related to the following four aspects:

- high configurational entropy,
- particular lattice distortion,
- sluggish diffusion,
- and so-called "cocktail effect".

Additionally, they should result in a solid solution and in a single phase structure with a crystal lattice of fcc, bcc or hcp. There can be multi-phase alloys but these have been lately termed as compositionally complex alloys (CCAs). The high configurational entropy, which they received their name from, is tied to the fact that these alloys are based on equiatomic compositions. This approach is completely different in comparison to classical alloys which usually have one main element and other alloying elements in lesser concentrations. With the equiatomic composition the configurational entropy term can be rewritten as

$$S_{conf} = R \ln n, \tag{1.1}$$

where R is the universal gas constant and n is the number of elements. It describes the fact that in solid solution these elements have high amount of possibilities to occupy different crystallographic sites with no preferred sub-lattices as would be the case, for example in

intermetallic compounds. Further research showed some preference in short-range order between some elements in the alloys but to a lesser extent and still far away from element-specific sub-lattices. One of those alloys is the CoCrNi alloy which exhibits a Cr ordering trend tied to its magnetic properties, even though the alloy has Curie temperature around $4~\mathrm{K}$ [11].

Interest in HEAs raises because of their usually superior mechanical properties gained by the lattice distortions and cocktail effect. The distorted lattice stems from the different atomic sizes and causes variations in the dislocation energy, shape and speed as the dislocations move through the crystal. The CoCrNi alloy has some interesting mechanical properties as well and these are tied to low stacking fault energy and easy twinning [12].

The sluggish diffusion principle is again caused by mixing many elements as the energies related to atoms swapping their positions can be higher for some pairs and that is making the diffusion slower. The last principle, the cocktail effect, describes any other property that is gained by combining many different elements, be it twinning, thermal or electric conductivities, catalysis effect or corrosion resistance of a specific alloy [13–15].

The second material in this work is the YMn₂ intermetallic compound. It is an antiferromagnet with Néel temperature around 100 K. At the Néel temperature it undergoes a phase transformation to the paramagnetic state which is accompanied by an abnormal volume change of 5%. The origin of this volume change is thought to be tied to the increase of magnetic entropy with the increase of randomness in magnetic moments after reaching the Néel temperature but it is still yet to be explained thoroughly. There are also some conflicting reports on the magnetic structure of the alloy and it seems that it may have very similar energetics for multiple antiferromagnetic and helimagnetic orderings [16–18]. In 2020 Pulkkinen et al. [19] have successfully done calculations on pure α -Mn via metaGGA functional. The α -Mn state is notorious for being unobtainable just by DFT due to its complicated noncollinear magnetic structure consisting of 4 sublattices [20]. It appears that metaGGA functionals can be up to the challenge.

Recently, machine learning has made its name in the field of materials simulations. Over the last two years the machine learning potentials have reached DFT levels of accuracy[21]. What is maybe even more important, the so-called universal machine learned potentials were introduced and now they can reproduce these levels of accuracy without the need for the user to train their own potential or, at worst, learn just parts of their problem to do so-called refitting [21].

2. Ordering in alloys

2.1 Theory of ordering in alloys

In metals there are two typical atomic orderings that can be encountered - solid solutions and intermetallic compounds. The basic difference is that solid solutions are usually composed of atoms occupying lattice sites at random or with slight energetic preferences in one of the components while intermetallic compounds occupy very specifically determined positions in the crystal lattice while also having crystal structures different from the components.

Solid solutions can be of different types with the two main being substitional solid solutions and interstitial solid solutions. The substitional solid solution can be randomly ordered, clustered or ordered, all depending on which configuration minimizes the Gibbs free energy. In long range ordered structures (for example CuAu) [22] the entropy of mixing is extremely low and with increasing temperature it will cease the long range order. There is a possibility to have a perfect mixing between two elements and thus have a solid solution over the whole composition range. This is determined by the Hume-Rothery rules:

- the size factor the difference of atomic sizes of the components must be within 15%,
- components have to have the same crystal structure,
- components have to have the same valence configurations,
- the electronegativity of components must be very similar.

These conditions must be met should the solid solution have unlimited solubility but are not sufficient to guarantee it [23]. Similarly, interstitial solid solutions have to follow modified rules [24]:

- atomic radius of the interstitial atom should be smaller than 59% of the matrix atom,
- interstitial and matrix atoms should have similar valency,
- atoms must have similar electronegativity.

Interstitial solid solutions can also have preferences for their positions as they may prefer one element over the other in their nearest neighbours.

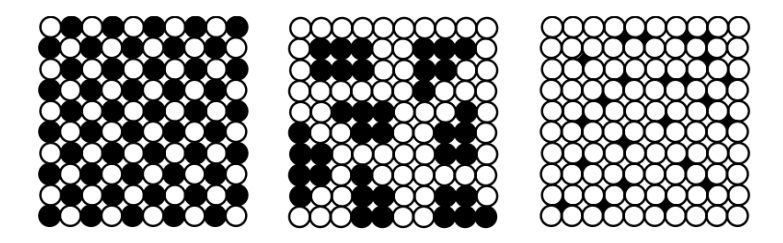


Figure 2.1: Examples of solid solutions with, from left side, ordered, random clustering, random interstitial [22].

Intermetallic compounds are formed if the configuration with the lowest Gibbs free energy has a completely different crystal lattice from the components [23, 24]. They can be

found in either stoichiometric, *i. e.* they have some type of A_mB_n formula, or with some composition range allowed. The resulting structure is dependent on three factors, relative atomic sizes, valency and electronegativity. If the atomic size ratio is in between 1.1 to 1.6 it is possible that a most efficiently filled structure for the atoms will be formed, for example Laves phases based on the $MgCu_2$, $MgZn_2$, $MgNi_2$ archetypes. Interstitial compounds are possible as well for the correct size ratios, the archetypes are then MX, M_2X , MX_2 , M_6X where M can be Zr, Ti, V, Cr etc. and X can be H, B, C, N, i.e. one of the few possible small enough atoms [22, 23]. In this archetypes the M atoms form either cubic or hcp lattice and the X atoms fit in between them. Hume-Rothery phases are on the other hand dependent on the valence configurations of the components and can then form α or β phases. Valency compounds depend on the electronegativity of the components, if they have large enough electronegativity difference a ionic bound can be formed as the type of Mg_2Sn [24].

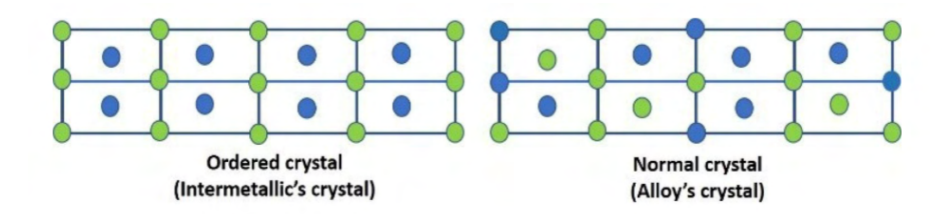


Figure 2.2: Difference between intermetallics and solid solution alloy [24].

2.2 Warren-Cowley parameters

Parameter α to describe the short-range order in alloys was first proposed in 1950 by J.M. Cowley [25]. One of the possible ways to calculate the parameter to describe ordering between two elements i and j is

$$\alpha_{ij} = 1 - \frac{N_{ij}}{x_j N_i},\tag{2.1}$$

where N_{ij} is the number of j-type atoms around a particular i-type atom (i.e. the number of bonds between element i and j), x_j is the atomic concentration of element j and N_i is the coordination number of the calculated cell for the i-type atom. This description is not limited to alloys consisting of just two elements but basically any amount. It is also beneficial for ab initio calculations as the amount of atoms of the elements in nearest neighbour shells is easily accessible by the means of VASP output files or by using external tools like aflow [26] or pymatgen [27].

For perfectly random alloy the parameter will result in zero $\alpha_{ij} = 0$, other results will indicate some tendency of elements to order. Negative values indicate clustering as the bonds between the chosen elements are more prevalent in comparison to random order. Positive values indicate preference in lower amount of bonds between chosen elements in comparison to a randomly ordered structure.

3. Ab initio calculations

The ab initio calculation methods allow us to compute material properties without any experimental data. They are based on the basic principles of quantum mechanics and the Schrödinger equation:

$$\mathcal{H}\psi = \varepsilon\psi. \tag{3.1}$$

Writing down the components of the Hamiltonian it has the shape of:

$$\left(V(r) - \frac{\hbar^2}{2m_e} \nabla^2\right) \psi(r) = \varepsilon \psi(r) \tag{3.2}$$

where V is the potential acting on the electron, m_e is the mass of electron, \hbar is the reduced Planck constant and $\psi(r)$ are the wavefunctions [4]. However, solving it exactly for more than one electron becomes too complex and thus some approximations have to be made.

First such approximation is the Born-Oppenheimer adiabatic approximation. This takes into account the fact that protons have a mass approximately 1836 times higher than electrons thus electrons are going to react instantly to any motion of the nucleus. With this we can say that the protons are fixed in space while we solve the electronic structure for this positions of ions. After the electronic structure is solved the ions can be moved and new electronic structure is calculated for the new positions of ions.

3.1 Density Functional Theory

3.1.1 General description

Density Functional Theory (DFT) allows calculation of large systems by replacing the many electron wavefunctions $\psi(r)$ with electron density $\rho(r)$. The electron density $\rho(r)$ for a system of N_{el} electrons is:

$$\rho(r) = N_{el} \int \psi^*(r, r_2, ..., r_{N_{el}}) \psi(r, r_2, ..., r_{N_{el}}) dr_2 dr_3 ... dr_{N_{el}}^3.$$
(3.3)

The density is independent on which electrons are chosen to integrate over which follows the required antisymmetry from Pauli principle (described further in Equation (3.30)). Normalization of the wavefunction then gives the equation:

$$\int \rho(r)dr^3 = N_{el}. \tag{3.4}$$

Now the dependence is not on $3N_{el}$ parameters as for the original Schrödinger equation but only on 3 parameters of space, the 4th one can be spin if it is chosen to be included. Another advantage in DFT is the fact that the Hamiltonian can be taken as a Hamiltonian of a single, non-interacting electron with effective potential that replaces the external one. This was all proposed by Hohenberg, Kohn and Sham in 1960s. The theory and the previously mentioned advantages are based on two theorems [4, 5].

First theorem (existentional) is that the density $\rho(r)$ of the system of N_{el} electrons determines all the ground state electronic properties because the ground state wavefunction Ψ_0 is an unique functional of electron density. Further physical properties can then be derived from this wavefunction, importantly, the ground state energy:

$$\varepsilon_0[\rho(r)] = \langle \Psi_0 | \mathcal{T} + \mathcal{V} + \mathcal{U} | \Psi_0 \rangle, \qquad (3.5)$$

where \mathcal{T} and \mathcal{V} represent one electron kinetic and potential energy and \mathcal{U} is representing the two-electron interactions [1, 4, 5].

Second theorem (variational) states that the energy for the ground state density is lower than for any other state. It means that the energy is inherently dependent on the electronic density and thus can be minimized by its variations. The only problem that arises is the fact that the correct density functional is unknown and thus it must be reached by further approximations [1, 4, 28].

The new Hamiltonian is now a function of electron density instead [4]:

$$\langle \psi | \mathcal{H} | \psi \rangle = T_{el} + V_{ZZ} + V_{ext} + V_{ee}, \tag{3.6}$$

where the first term represents the kinetic energy of electrons, second term represents interactions between atomic nuclei, third term is interactions between electrons and external potential and last term is the interaction between electrons themselves composed of the Coulomb interactions between the electrons and the exchange correlation effects. The Coulomb interactions can be written in forms of Hartree energy as:

$$\varepsilon_H(\rho) = \frac{1}{2} \int \rho(r) V_H(r) dr, \qquad (3.7)$$

where V_H is the Hartree potential [4].

$$V_H(r) = \frac{\partial \varepsilon_H}{\partial \rho}.$$
 (3.8)

Another part of the Kohn Sham theory is taking the electrons as non-interacting particles. The exchange-correlation term now becomes:

$$\varepsilon_{xc} = \widetilde{\varepsilon_{xc}} + (T_{el} - T_s),$$
(3.9)

where it now includes the kinetic energy of non-interacting electrons T_s and the correction that handles the interaction T_{el} . This can be again defined as an exchange-correlation potential [4, 5]:

$$V_{xc} = \frac{\partial \varepsilon_{xc}}{\partial \rho}.$$
 (3.10)

With this all the potentials influencing the electron density can be taken into one variable - the effective potential [4, 28]:

$$V_{eff}(r,\rho) = V_H(r,\rho) + V_{xc}(r,\rho) + V_{ext}(r).$$
 (3.11)

This allows to use a single-electron Hamiltonian \mathcal{H}_{sp} subjected to the same effective potential as the multielectron system.

$$\mathcal{H}_{sp} = V_{eff}(r, \rho) + \frac{p^2}{2m_c},\tag{3.12}$$

or in the terms of wavefunctions as:

$$H_{sp}\psi_i(r) = [-\nabla^2 + V_{eff}(r)]\psi_i(r) = \varepsilon_i\psi_i(r), \qquad (3.13)$$

with the one particle density as [28]:

$$\rho(r) = \sum_{i=1}^{N} |\psi_i(r)|^2. \tag{3.14}$$

3.1.2 Exchange-correlation functionals

However, there is still problem with the exact energy functional, specifically its exchange-correlation part, which is not known. This is practically solved by approximations [5, 28]. There are multiple approaches of approximating the exchange-correlation and they can be described via the so called Jacob's ladder [29].

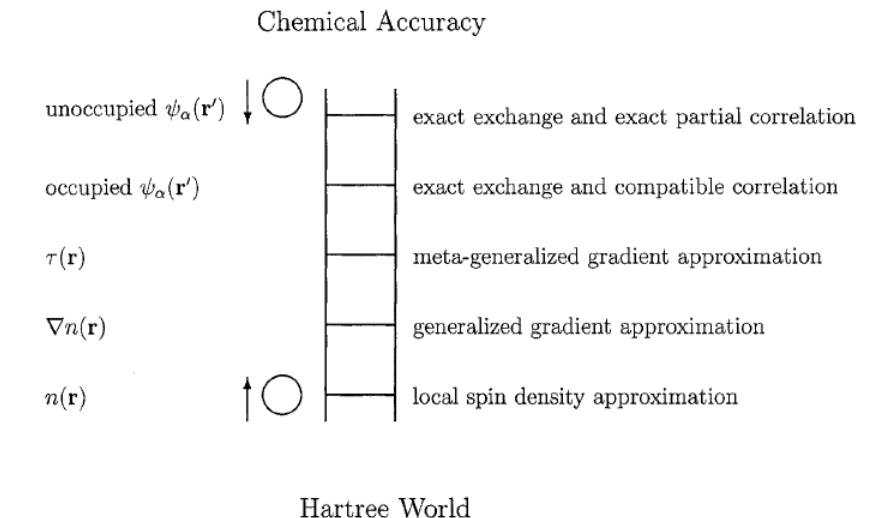


Figure 3.1: Jacob's Ladder for Exchange-Correlation Functionals [30].

Here, from top to bottom, the approaches are ordered from the most robust and computationally expensive to the simplest. First and simplest method found at the bottom of Jacob's ladder is the local-density approximation (LDA):

$$E_{xc}[\rho] = \int \rho(r)\varepsilon_{xc}[\rho(r)]d^3r, \qquad (3.15)$$

where $\varepsilon_{xc}[\rho(r)]$ is the exchange-correlation energy per particle in a homogenous system of electron density $\rho(r)$ [28]. It takes the solids as being close to the limit of the homogenous electron gas (nearly-free-electron metals) and thus takes the effects of exchange and correlation as local [5]. The local spin density approximation (LSDA) is received by including spin and the integral in Equation (3.15) changes to incorporate the densities of spin-up and spin-down electrons and the vector of magnetization density [1]. Because of its local character this method fails for systems with strong density gradients, for example it can not predict the correct ground state of Fe and can not be applied to systems containing elements with f-electron shells [28].

Improvement of LDA is the generalized gradient approximation (GGA) which takes into account not just the value of the local density but its gradient as well. The generalized form of the functional is:

$$E_{xc}[n_{\uparrow}, n_{\downarrow}] = \int \varepsilon_{xc}(n_{\uparrow}, n_{\downarrow}, |\nabla n_{\uparrow}|, |\nabla n_{\downarrow}|, ...) d^{3}rn(r)$$

$$= \int \varepsilon_{x}^{hom}(n) F_{xc}(n_{\uparrow}, n_{\downarrow}, |\nabla n_{\uparrow}|, |\nabla n_{\downarrow}|, ...) d^{3}rn(r),$$
(3.16)

where F_{xc} is a dimensionless parameter and ε_x^{hom} is the exchange energy of unpolarised electron gas. The multiple commonly used functionals like Perdew, Burke and Ernzerhof (PBE), Perdew and Wang (PW91) or Lee-Yang-Parr (LYP) differ in the parametrization of the F_{xc} parameter [5].

Another step on the ladder is the meta-GGA functional. The addition here is the kinetic energy density or its Laplacian. Furthermore, there are other conditions - exact constraints, which these meta-GGAs should satisfy. Out of the available approaches Strongly Constrained and Appropriately Normed (SCAN) functional [31] is the first that satisfies all of them. Following its success regularized versions of SCAN were created to improve numerical stability. These are the rSCAN, r²SCAN and r⁴SCAN where r²SCAN is taken as the best performing. The semilocal approximation to the exact functional in meta-GGAs are as follows:

 $E_{xc}[n_{\uparrow}, n_{\downarrow}] = \int d^3 r \, n \, \epsilon_{xc}(n_{\uparrow}, n_{\downarrow}, \nabla n_{\uparrow}, \nabla n_{\downarrow}, \tau_{\uparrow}, \tau_{\downarrow}), \qquad (3.17)$

where the τ_{σ} are the kinetic energy densities which are implicitly nonlocal functionals of the electron spin densities. Kinetic energy density is not represented directly but instead by a dimensionless variable α . Reason for this variable is to eliminate order-of-limits that caused lower accuracy for the first few meta-GGA functionals like TPSS. This dimensionless variable is defined as:

$$\alpha = \frac{(\tau - \tau^W)}{\tau^{unif}} > 0, \tag{3.18}$$

where $\tau^W = |\nabla n|^2/8n$ is the single orbital limit of the kinetic energy density and $\tau^{unif} = (3/10)(3\pi^2)^{(2/3)}n^{(5/3)}$ is the uniform density limit [31]. This α can recognize if there is a covalent single bond ($\alpha = 0$), metallic bond ($\alpha \approx 1$) and weak bond ($\alpha >> 1$). The SCAN pseudopotential then uses these α parameters to tune the performance in accordance with local chemical environment as well as satisfying constraints that would be contradictory to the GGA. On the other hand, this parameter can introduce certain numerical sensitivities as well as introducing issues with quite high requirements for integration grids in localized basis function based codes [32]. To eliminate the grid sensitivity there were proposed regularizations of the functional [32, 33] which introduce modified, regularized, parameter α :

$$\tilde{\alpha} = \frac{\tau - \tau^W}{\tau^{unif} + \tau_r},\tag{3.19}$$

$$\alpha' = \frac{\tilde{\alpha}^3}{\tilde{\alpha}^2 + \alpha_r}. (3.20)$$

In the modification the $\tau_r = 10^{-4}$ and $\alpha_r = 10^{-3}$ are regularization constants for rSCAN [33]. This introduced some issues with accuracy as the α' does not retain correct uniform and nonuniform scaling properties of the original α as well as the correct uniform density limit [32]. The regularized-restored SCAN (r²SCAN) takes the same approach but at the same time restores the uniformity of the original SCAN via the modified parameter $\overline{\alpha}$:

$$\overline{\alpha} = \frac{\tau - \tau^W}{\tau^{unif} + \eta \tau^W},\tag{3.21}$$

where $\eta=10^{-3}$ is the regularization parameter. Regularization in this way leads to the same range for $\overline{\alpha}$ as was for the original α . Another change is for the exchange part by, again, adding dependence on the η parameter to eliminate errors for $\overline{\alpha} \to 1$. This way r²SCAN recovers one of the exact constraints lost by previous regularization in rSCAN.

The so called "deorbitalization" of the previously mentioned metaGGA functionals turns the exact orbital-dependent non-local Kohn-Sham kinetic energy density into a Laplacian. This will speed up the calculations while simultaneously sacrificing some of the accuracy except for one area - magnetism. The deorbitalized versions usually lead to improved accuracy in magnetic moments of metals, where the non-locality of τ as the semi-local approximations to valence-valence exchange correlation may be better to represent metallic screening [32].

The first deorbitalized functional was the Lee-Yang-Parr (LYP) correlation functional with mixed success [34]. The strategy to deorbitalize a functional is to take the orbital dependent parameter and approximate it via orbital independent kinetic energy density functional with proper parametrization [34]. Four kinetic energy density functionals were chosen by Mejia-Rodriguez [34] by how well they reproduced Pauli term obtained via accurate Hartree-Fock methods, they are as follows: Perdew and Constantin metaGGA (PC), Cancio and Redd mGGA (CRloc), Thomas-Fermi plus Laplacian mGGA (TFLreg) and modified VT84F plus Laplacian (MVT84F+L), which was discarded because of its difficult integration of the density overlap region indicator. The remaining three kinetic energy density functionals had their parameters reoptimized against the first 18 neutral atoms test set [34]. The SCAN functional has the orbital dependence in the parameter α for both exchange and correlation making it easier to deorbitalize than others (like TPSS) which can have multiple [34]. The α is included in the exchange enhancement factor $F_x^{SCAN}(s,\alpha)$ as

$$f_x(\alpha) = e^{-c_{1x}\alpha/(1-\alpha)}\theta(1-\alpha) - d_x e^{c_{2x}/(1-\alpha)}\theta(\alpha-1), \tag{3.22}$$

and

$$h_x^1(s,\alpha) = 1 + \frac{k_{1X}}{k_1 + x},$$
 (3.23)

$$x = \mu_{GE} s^2 \left[1 + \frac{b_4 s^2}{\mu_{GE}} e^{-b_4 s^2 / \mu_{GE}} \right] + \left[b_1 s^2 + b_2 (1 - \alpha) e^{-b_3 (1 - \alpha)^2} \right]^2, \tag{3.24}$$

and in the correlation part through

$$f_c(\alpha) = e^{-c_{1c}\alpha/(1-\alpha)}\theta(1-\alpha) - d_c e^{c_{2c}/(1-\alpha)}\theta(a-1).$$
(3.25)

The chosen kinetic energy density functional for SCAN-L was the reoptimized PC (PCopt) reaching very similar values for mean errors as the original SCAN functional [34]. In their publication, Mejia-Rodriguez and Trickey [34] mention the basis set dependence of both SCAN and the new SCAN-L but since their usage of local basis set code it is an expected behaviour of these functionals [32].

Further up along the Jacob ladder are the hybrids. These take into account the exact Hartree exchange energy and thus their computational cost gets quite high. They combine Hartree-Fock and Kohn-Sham theories in variable ways. The exchange correlation energy is defined as:

$$E_{xc}^{hybrid} = \alpha E_x^{HF} + (1 - \alpha)E_x^{GGA} + E_c^{GGA}, \qquad (3.26)$$

where α determines the relative amount of Hartree-Fock and semilocal exchange [8]. The functionals are further divided into categories in accordance to the interelectronic range at which are the Hartree-Fock exchange is applied. Full range are so called unscreened, short range and long range - screened or range separated hybrids.

3.1.3 Wavefunction expansion

The basis functions into which the Kohn-Sham wavefunctions are expanded are periodic in crystals and thus this expansion can be done by using plane waves. Further, strong Coulomb potentials and tightly bound core electrons are replaced by an effective potential acting on the valence electrons. These so-called pseudopotentials and related pseudo-wavefunctions of valence electrons have the big advantage of reducing the number of computed electrons to the electronic valence states which, in contrast to core electrons, are responsible for most of chemical bonds. The original idea was the orthogonalized plane wave method (OPW) that was further reformulated to projector augmented wave (PAW) method for DFT usage. The valence wavefunctions are expressed as a sum of smooth functions plus core functions with generalized eigenvalue equations in both OPW and PAW methods. The PAW method then retains the entire set of all-electron core functions instead of just empirical values as is the case in OPW method. The matrix elements involving core functions are treated as muffin-tin spheres [5].

3.2 Magnetism in DFT

3.2.1 General definitions

Magnetism of material in DFT originates primarily from electrons and it is defined by their magnetic moment. To describe the magnetic moments the unit of Bohr magneton (μ_B) is used and defined as:

$$\mu_B = \frac{e\hbar}{2m_e},\tag{3.27}$$

and $1 \mu_B = 9.274 \times 10^{-24} \,\mathrm{Am^2}$. The magnetic moment is created by two distinct sources, the orbital motion of electron and its spin. These are coupled by the spin-orbit interaction which is heavily dependent on the proton number and thus scales into an important contributor for heavy elements and their inner electron shells. The interaction in terms of the single electron Hamiltonian results in:

$$\mathcal{H}_{so} = \lambda \hat{\boldsymbol{l}} \cdot \hat{\boldsymbol{s}}, \tag{3.28}$$

where λ is the spin-orbit coupling energy and $\hat{\boldsymbol{l}}$ and $\hat{\boldsymbol{s}}$ are dimensionless operators [1]. With magnetic systems having a small number of basis states v each denoted by a different magnetic quantum number m_i they can then be described by a hermitan matrices $v \times v$ which for angular momentum with quantum number ℓ becomes $v = (2\ell + 1)$. Similarly for spin with the basis states $m_s = \pm \frac{1}{2}$ the spin angular momentum is then represented by a 2×2 spin operator $\hat{\boldsymbol{s}}$ with three components $\hat{\boldsymbol{s}_x}$, $\hat{\boldsymbol{s}_y}$ and $\hat{\boldsymbol{s}_z}$. The $\hat{\boldsymbol{s}_z}$ is the diagonal part with eigenvalues $\frac{1}{2}\hbar$ and $-\frac{1}{2}\hbar$ representing $m_s = \pm \frac{1}{2}$. The two possible states of electron are then defined as spin-up or spin-down eigenvalues of the matrix $\hat{\boldsymbol{s}_z} = \begin{bmatrix} 1 & 0 \\ 0 & -1 \end{bmatrix} \frac{1}{2}\hbar$.

The eigenvectors of the matrices are known as spinors. By multiplying the \hat{s} by $2/\hbar$ a dimensionless operator $\hat{\sigma}$ is gained with components known as the Pauli spin matrices [1]

$$\hat{\boldsymbol{\sigma}} = \left(\begin{bmatrix} 0 & 1 \\ 1 & 0 \end{bmatrix}, \begin{bmatrix} 0 & -i \\ i & 0 \end{bmatrix}, \begin{bmatrix} 1 & 0 \\ 0 & -1 \end{bmatrix} \right). \tag{3.29}$$

To describe spin-orbit interaction in many electron system the term for total angular momentum J needs to be introduced. It is formed by coupling L and S as J = L + S, the

L and S are sums of the orbital angular momentum ℓ and spin angular momentum s [1, 2]. In multielectron systems the electrons occupy the different shells according to Hund's rules, first to maximize S, then maximizing L and, finally, coupling L and S to form J [1].

3.2.2 Magnetic orderings

For DFT the collinear magnetic structures are paramagnetic, ferromagnetic and antiferromagnetic. Ferromagnetism describes material with all the magnetic moments oriented in one direction raising spontaneous magnetization. Antiferromagnetism has at least two sublattices with equal magnetic moments oriented in opossite directions thus giving no magnetization as a whole.

Paramagnetism relates to a material in which the magnetic moments are oriented randomly unless some external magnetic field is present. When external field is applied the moments allign themselves along the axis of applied field. To calculate paramagnetic states in DFT multiple approaches can be used. It is possible to use non-spin-polarised calculations but this approach can lead to errors in the resulting electronic structure or even incorrect predictions of the ground states [35]. It is possible to use the SQS method described in Section 3.5 to simulate paramagnetic states. This will create a pseudo-random distribution of equal number of antiparallel magnetic moments resulting in zero magnetization for the whole cell, similarly to antiferromagnetism but without specific sublattices for magnetic moment orientations. It is the best to use a set of these SQS spin configurations and then average over the results instead of using only one distribution as a model for paramagnetic state. It is even possible to use collinear spins for these simulations and just assign spin-up and spin-down values. Similar method is the magnetic sampling method, where the non-collinear magnetism can be used and multiple cells with randomly oriented moments are calculated and averaged over. Both of these approaches can be quite time and computational resource consuming for many systems as the number of random configurations can be quite high for disordered alloys (for example the HEAs) or large calculation cell with low symmetry. They can get even more computationally expensive when one wants to calculate the temperature dependencies and include lattice vibrations, which are quite important for the paramagnetic ordering [35–37].

The determination whether the moments will allign ferromagnetically or antiferromagnetically is tied to their exchange interactions with each other. The most basic interaction is the magnetic dipolar interaction [2] where two magnetic dipoles μ_1 and μ_2 are separated by r. The dipole interaction is quite weak as for two moments of size $1 \mu_B$ separated by r = 1 Å, the energy is in order of 10^{-23} J, thus can not in itself be responsible for the ordering but can have an effect at mK temperatures [1]. Stronger exchange interactions come from the electrostatic interactions arising from charges of the same sign being close together or far apart. There is thus energy difference between $\uparrow_i \uparrow_j$ and $\uparrow_i \downarrow_j$ configurations of the spins of neighbouring atoms. Electrons are indistinguishable so exchange of two electrons must give the same electron density. Because electrons are fermions the only solution to comply with Pauli principle is for the total wave function of the two electrons to be antisymmetric

$$\Psi(1,2) = -\Psi(2,1). \tag{3.30}$$

The wavefunction is a product of functions of space coordinates $\phi(\mathbf{r}_1, \mathbf{r}_2)$ and spin coordinates $\chi(s_1, s_2)$. To satisfy Equation (3.30) the symmetric space functions must multiply the anti-symmetric spin function and vice versa. If the two electrons have parallel spin (spin triplet state) there is a low chance of finding them close to each other as electrons with

parallel spins will avoid each other. If the two electrons have antiparallel spins there is a higher probability of finding them in the same place as the spatial part of the wave function is symmetric under exchange of electrons. Energies of the two states can be evaluated from the Hamiltonian as [1]

$$\mathcal{H} = -2\mathcal{J}\mathbf{S}_1 \cdot \mathbf{S}_2,\tag{3.31}$$

where \mathcal{J} is the exchange constant, often divided by Boltzmann constant and expressed in Kelvins, and S_1 and S_2 are spin operators similar to Pauli spin matrices. If the exchange constant $\mathcal{J} > 0$ it indicates a ferromagnetic interaction, if $\mathcal{J} < 0$ it indicates antiferromagnetic interaction [1, 2]. This Hamiltonian needs to be generalised if there is a lattice to sum over all pairs of atoms on lattice sites i, j [1]

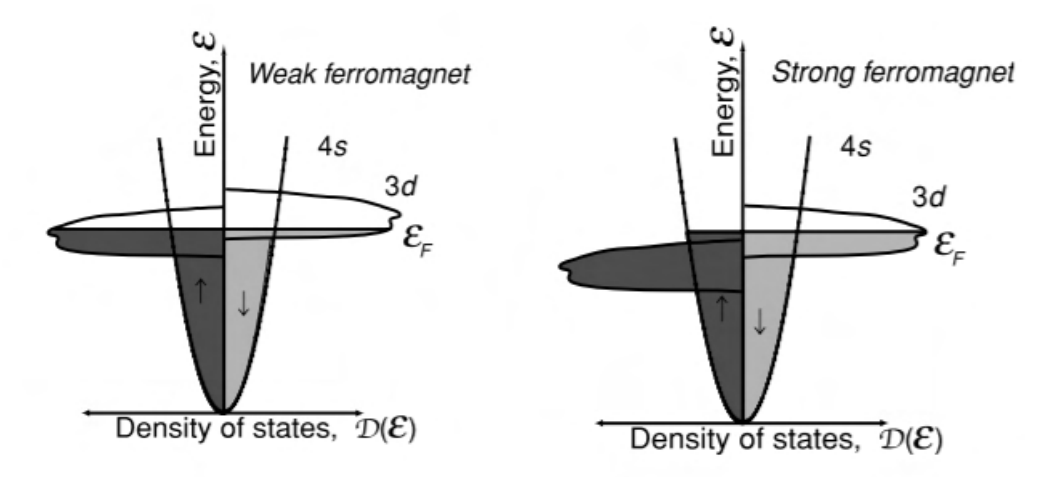
$$\mathcal{H} = -2\sum_{i>j} \mathcal{J}_{ij} \mathbf{S}_i \cdot \mathbf{S}_j. \tag{3.32}$$

In this Hamiltonian this sum is simplified to only count the first nearest neighbour interactions and there is only single exchange constant \mathcal{J} [1, 2]. There are different types of exchange interactions. Superexchange can be found in insulators where the electrons are localized and it is an indirect interaction between non-neighbouring magnetic ions mediated by a non-magnetic ion between them. The origin of this interaction is the kinetic energy advantage for antiferromagnetism [2]. Antisymmetric exchange appears in materials with low symmetry and the weak antisymmetric coupling is called Dzyaloshinski-Moriya interaction. It requires the ions to be already coupled by superexchange. The coupled spins are perpendicular to each other and it can result in antiferromagnetic ordering but with moments pushed away by 1° from their axis resulting in a weak ferromagnetic moment. Direct exchange occurs between electrons on two neighbouring magnetic ions. It depends on how the bands are filled, if they are roughly half-filled the interaction will be antiferromagnetic, if they are nearly filled or nearly empty they will allign ferromagnetically, this describes for example Cr and Mn as antiferromagnetic and Fe and Co as ferromagnetic [1]. On-site interactions between conduction electrons and core spins causes s-d coupling. This introduces ferromagnetic coupling between ions [1]. Double exchange happens between 3dions which have both localized and delocalized d electrons. Compared to ferromagnetic superexchange, a mixed valence configurations are required but they are restricted to two configurations. It is ferromagnetic because the transfer is zero when the ions on adjacent sites are antiparallel [1, 2].

Ferromagnetism manifests itself by a spontaneous magnetization M_s that is present even in the absence of applied magnetic field, i. e. all the magnetic moments are aligned along the same direction. Ferromagnetism is due to the exchange interactions with positive exchange constants. Heating above a certain temperature - Curie temperature - results in collapse of the spontaneous magnetization. Spontaneous magnetization can be described by the Stoner criterion. The narrower the bands in metal, the higher the susceptibility as it depends on the density of states at Fermi level. If the density of states is high enough, the metal will become ferromagnetic as it is energetically favourable for the bands to split. The criterion for ferromagnetism, i. e. when the susceptibility diverges spontaneously, is then defined from the density of states per atom for each spin state

$$\mathcal{IN}_{\uparrow,\downarrow}(\varepsilon_F) > 1,$$
 (3.33)

where \mathcal{I} is the Stoner exchange parameter and it is equal to 1 eV for 3d ferromagnets. Only Fe, Co and Ni satisfy the Stoner criterion [1–3, 5]. Satisfying the Stoner criterion means



(a) Weak ferromagnet density of states [1] (b) Strong ferromagnet density of states [1]

Figure 3.2: Difference between density of states spiltting in strong and weak ferromagnet.

that the spin-up d-subbands get pushed completely below Fermi level and the spin-down stay above, thus creating a split for a strong ferromagnet. Otherwise the ferromagnet will be weak. This means that out of the three elements satisfying the Stoner criterion Co and Ni are strong ferromagnet while Fe is a weak one.

Antiferromagnetism describes a situation of two equal magnetic moments but in two opposite directions. It is caused by the negative exchange $\mathcal{J} < 0$ and, similarly to ferromagnetism, disappears at a specific temperature - Néel temperature T_N . There can be a specific case of two unequal opposite magnetic sublattices in which one has a larger magnetic moment than the other, this specific case is called ferrimagnetism. Thus ferrimagnets are technically antiferromagnets with two equal sublattices with unequal magnetic moments [1, 2]. Their net magnetization is nonzero and it falls to zero at critical temperature T_C which is called ferrimagnetic Néel temperature but it is also possible that the two sublattice magnetizations cancel each other exactly at a different temperature - the compensation temperature T_{comp} [1].

In some crystal structures (tetragonal, fcc etc.) it may be impossible for magnetic moments to allign parallely perfectly [1–3]. A consequence of that is the change in exchange energy and that the Néel temperature is much lower than the paramagnetic Curie temperature θ_p ($T_N << |\theta_p|$). It also increases the ground state degeneracy and promotes forming of non-collinear spin structures to relieve the frustration. For simple cubic crystal lattice there are four possible antiferromagnetic orderings and the frustrations usually depend on the formula unit and supercell of the compound. The G ordering is unfrustrated, A and C are frustrated and F ordering is ferromagnetic.

For bcc structure either nearest neighbour or next-nearest neighbour interactions can be completely satisfied and there is no frustration as these are two decoupled simple cubic antiferromagnetic structures, they are denoted as type I and type II respectively. If both antiferromagnetic interactions are present some frustrations will arise. In fcc the nearest neighbour exchange is always frustrated. It divides into four simple cubic sublattices each with their own magnetizations, each atom then has 4 nearest neighbours on each of the other three sublattices. This results in three possible modes, alternating ferromagnetic

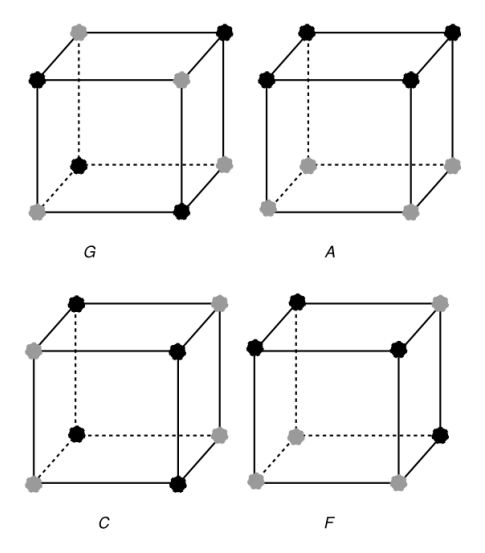


Figure 3.3: Possible antiferromagnetic orderings in simple cubic lattice [1].

planes [0 0 1] is type I, alternating ferromagnetic planes [1 1 1] is type II and alternating antiferromagnetic planes [0 0 1] is type III[1].

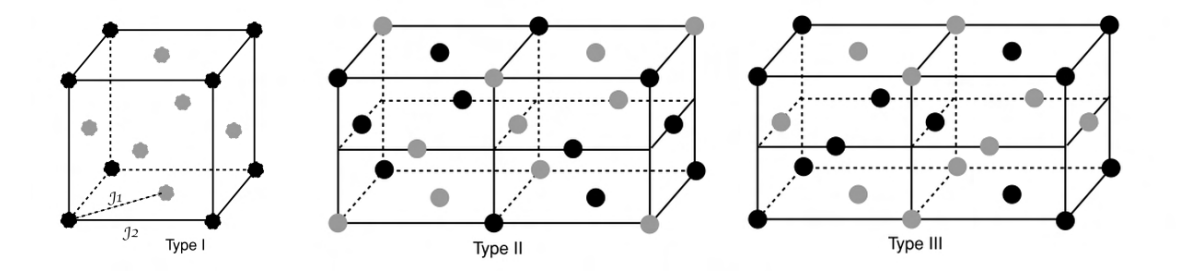


Figure 3.4: Antiferromagnetic modes for fcc [1].

3.3 Vienna Ab initio Simulation Package (VASP)

For all calculations in this work the program Vienna Ab initio Simulation Package (VASP) developed by the team of prof. Georg Kresse was used. The package uses the variational theorem of the DFT described in previous section to find the ground state of the electron density given by the input crystal structure. Solution of the Kohn-Sham equations is iterative by a self-consistent cycle (Figure 3.5). It begins with creation of some initial electron density given by the crystal structure, elements on the sites and pseudopotentials used. Then it evaluates the effective potential V_{eff} affecting the electrons and solves the Kohn-Sham equations. From the received wavefunctions it derives the total energy and forces acting on ions. The process is then repeated to minimize the energy until a given convergency criterion for either forces or energy is reached. To reach the energy minimum different algorithms can be used, an example in the self-consistency diagram is denoted as RMM-DIIS and Davidson (Figure 3.5). These differ in treatment of orbitals and their

optimization and are not the only ones available in VASP, just two of the most commonly used [8]. The forces are approximated by the means of Hellman-Feynman theorem as a derivation of the total energy [6, 7].

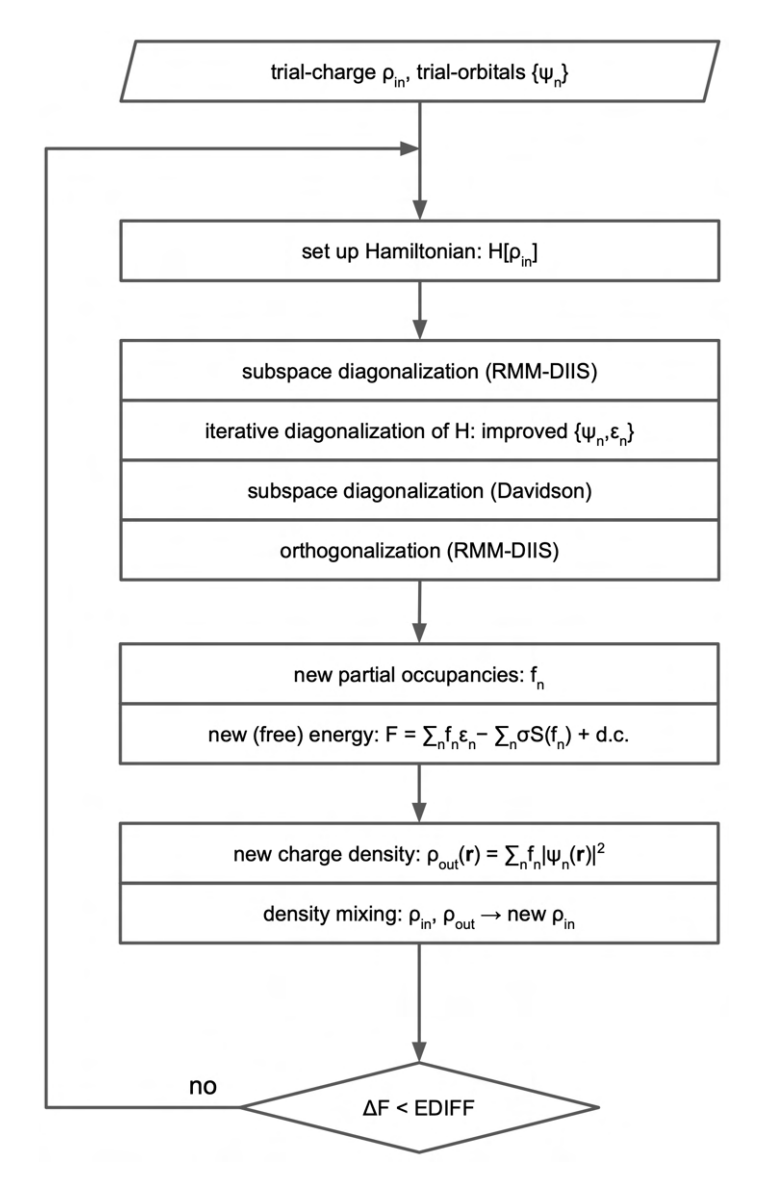


Figure 3.5: Self consistency cycle of VASP [8].

3.3.1 Modelling magnetism in VASP

Magnetism in VASP can be treated as a collinear or non-collinear. The spin degrees of freedom can be treated in a spin-polarised calculation by using the setting ISPIN = 2 in the INCAR input file. As in standard DFT the electron has an effective potential applied to it but now it has an additional spin component σ :

$$V_{eff}^{\sigma} = V_{ext}(r) + V_{H}(r) + V_{xc}^{\sigma}(r). \tag{3.34}$$

The exchange-correlation potential is now:

$$V_{xc}^{\sigma} = \frac{\partial E_{xc}[n_{\uparrow}, n_{\downarrow}]}{\partial n_{\sigma}},\tag{3.35}$$

where n_{σ} is the spin charge density. This spin dependent effective potential then goes into the Kohn-Sham equations and leads to a spin-dependent solutions:

$$\left[-\nabla_n^2 + V_{eff\uparrow}(r_n) \right] \psi_{\uparrow n} = \varepsilon_n \psi_{\uparrow n},
\left[-\nabla_n^2 + V_{eff\downarrow}(r_n) \right] \psi_{\downarrow n} = \varepsilon_n \psi_{\downarrow n}.$$
(3.36)

Then the self-consistent cycle continues with updated spin-up and spin-down charge densities until desired convergence criterion is reached [8].

Non-collinear magnetism requires additional extension to the Hohenberg-Kohn-Sham DFT by, again, introducing an additional spin index. The non-collinear magnetism is turned on by the tag LNONCOLLINEAR = .TRUE. in the INCAR file and this time running a different executable - vasp_ncl. The spin-density matrix is introduced as:

$$n_{\sigma',\sigma}(r) = \sum_{i=1}^{N} \psi_{\sigma'n}(r)\psi_{\sigma n}^{\star}(r), \qquad (3.37)$$

and the effective potential becomes a 2×2 matrix:

$$v_{\sigma'\sigma}^{eff}(r) = v_{\sigma'\sigma}^{ext}(r) + \delta_{\sigma'\sigma}v^{H}(r) + v_{\sigma'\sigma}^{xc}(r). \tag{3.38}$$

The received Kohn-Sham equations now have KS orbitals with two-component spinors:

$$\sum_{\sigma} \left[-\delta_{\sigma'\sigma} \nabla_n^2 + V_{eff}^{\sigma'\sigma}(r_n) \right] \psi_{\sigma n} = \varepsilon_{\sigma'n} \psi_{\sigma'n}. \tag{3.39}$$

Noncollinear magnetism allows for simulation of spin-orbit coupling. In VASP the setting is LSORBIT = .TRUE. and it couples the spin degrees of freedom with the lattice degrees of freedom by adding:

$$H_{eac}^{\alpha\beta} \propto \boldsymbol{\sigma} \cdot \boldsymbol{L},$$
 (3.40)

to the Hamiltonian. This couples the Pauli-spin operator σ with the angular momentum operator L. The spin-orbit coupling (soc) in VASP is treated predominantly in the close vicinity of nuclei and thus is calculated only for the all-electron one-center contributions:

$$E_{soc}^{ij} = \delta_{\mathbf{R}_{i}\mathbf{R}_{j}} \delta_{l_{i}l_{j}} \sum_{n\mathbf{k}} w_{\mathbf{k}} f_{n\mathbf{k}} \sum_{\alpha\beta} \langle \tilde{\psi}_{n\mathbf{k}}^{\alpha} | \tilde{p}_{i} \rangle \langle \phi_{i} | H_{soc}^{\alpha\beta} | \phi_{j} \rangle \langle \tilde{p}_{j} | \psi_{n\mathbf{k}}^{\beta} \rangle, \qquad (3.41)$$

where $\phi_i(r) = R_i(|\mathbf{r} - \mathbf{R}_i|)Y_{l_i m_j}(\theta, \varphi)$ are the partial waves of an atom centered at \mathbf{R}_i , and $\psi_{nk}^{\tilde{\alpha}}$ is the spinor component $\alpha = \uparrow, \downarrow$ of the pseudo-orbital with band index n and Bloch vector \mathbf{k} , f_{nk} are the Fermi weights and w_k are the \mathbf{k} -weights [8].

3.3.2 Implementation and performance of metaGGA functionals

Usage of metaGGA functionals in the VASP code is quite straightforward. The kinetic energy density values are written in the pseudopotential POTCAR files, one only needs to check if the selected pseudopotential actually contains them, as some older versions do not. It is also recommended to use the pseudopotentials that treat more of the core states as the valence to obtain results comparable to all electron codes [8]. Then the basic setup is as simple as including new tags in the INCAR file - METAGGA = desired functional and LASPH = .TRUE. which introduces aspherical contributions to the PAW one-centre terms [8]. Furthermore, including the kinetic energy density in the density mixer helps with convergence so it is convenient to be turned on via LMIXTAU = .TRUE. in the INCAR file.

In reality moving from PBE GGA to metaGGA can get a bit complicated. Convergency tests should be done again and usually the cutoff energy needed for metaGGAs is higher than for PBE. The integration grid over the Brillouin zone is even more important, especially for the r²SCAN. Even though the original numerical instability for SCAN was observed in local basis set codes [32], in VASP - a plane wave basis set code, there is still requirement of a slightly higher amount of k-points compared to the value expected from PBE. Interestingly, we have found the r²SCAN to be more sensitive to the settings of k-points than the SCAN, a complete opposite behaviour than observed in the local basis set codes [32]. If there are convergency issues, one can also set a different electronic minimalization algorithm - the conjugate gradient for orbitals (setting ALGO = All in the INCAR file) instead of the default blocked-Davidson-iteration scheme.

Multiple studies evaluated the performance of the metaGGAs, mostly focusing on the SCAN family of functionals [38–43]. Both SCAN and r²SCAN promise improvements over GGA thanks to lower self-interaction errors by reproducing the Couloumb interaction with higher accuracy [43]. SCAN also correctly represents the H₂ molecule binding curve better than Hartree-Fock methods [43]. Kingsbury et al. [38] examined the performance of SCAN and r²SCAN functionals via automated workflow in which the structures were prerelaxed with GGA PBE and PBEsol and then subsequently run with SCAN and r²SCAN respectively, all within the VASP code (Figure 3.6). In their calculations they have used pseudopotentials from the dataset version 54, which is not the most recent. The recommended version is 64 released in September 2024 [7]. Their results show a decrease of mean average error (MAE) for mixing enthalpies for both metaGGAs in comparison to PBEsol as well as for band gaps. For volumes, the MAE is mostly the same, sometimes slightly larger than in PBEsol [38]. In terms of computational performance, even though their analysis was skewed by their methodology of pre-relaxation with GGA and different settings for different calculations [38], the r²SCAN had better performance, not only in computational hours but also in completion rate. Both of the metaGGAs took 4 times more CPU hours in comparison to PBEsol [38].

Liu et al. [39] looked at the performance of r²SCAN for 3d, 4d and 5d transition metals employing VASP and quasiharmonic approximation in combination with Phonopy [44, 45] (Figure 3.8). They have encountered an issue with simulation of Co hcp crystal lattice, the phonon calculations result in imaginary modes, thus unstable, while for the fcc Co showed no imaginary modes. For volumes, it improves the accuracy over the PBE GGA functional, and, in some cases, the PBEsol as well, the MEA and mean percentage error (MAPE) is then slightly better 0.42% for r²SCAN and -2.59% for PBEsol [39]. This goes slightly against the result of previously mentioned publication by Kingsbury et al. [38], where the volumes were very similar but their data set was much larger. Generally, in the work of

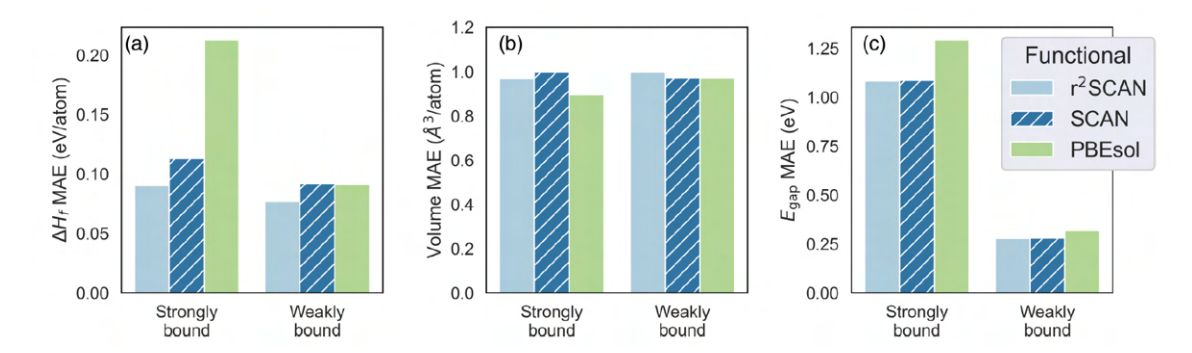


Figure 3.6: MAEs for a) mixing enthalpy, b) volumes and c) band gap energies for r²SCAN, SCAN and PBEsol taken from [38]

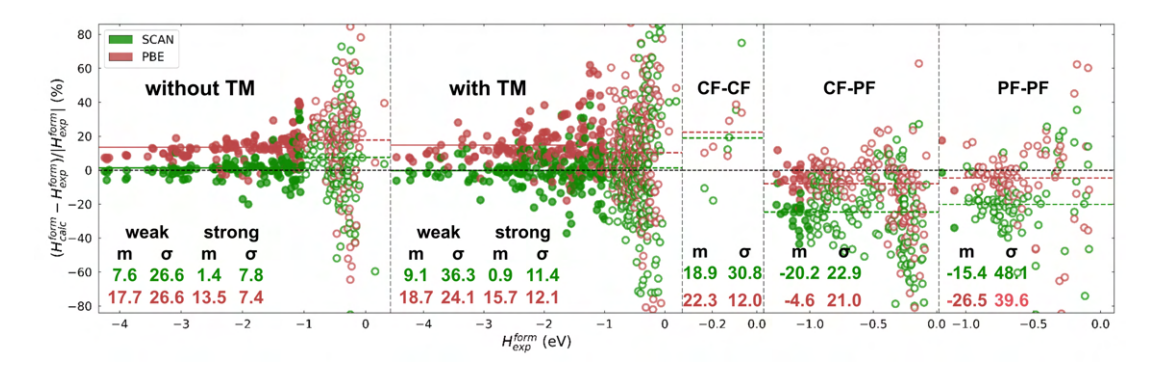


Figure 3.7: Comparison between mixing enthalpy obtained by experiment, SCAN and PBE for binary intermetallics taken from [40], first panel on the left are intermetallics without transition metals (TM), second is with one transition metal ion, third one (CF-CF) are with completely filled d-shell, CF-PF is completely filled and partially filled d-shell for the transition metal and PF-PF is partially filled for both ions in the intermetallic. Values m and σ denote the mean and standard deviation from experimental mixing enthalpy respectively.

Liu et al. [39], the r²SCAN mostly improves or is at least as good as PBEsol. Similarly, Sokolovskiy et al. [40] in their review looked at the mixing enthalpy of binary intermetallics reported in literature (Figure 3.7). For mixing enthalpies without transition metals SCAN improves the results over PBE by a quite large margin, for strongly coupled compounds it reaches only 1.4% compared to 13.5% by PBE. For weakly coupled compounds the situation is very similar, the improvement here comes from the van der Waals chemical bond that SCAN can distinguish and include [40]. In addition, SCAN also predicts some intermetallics correctly stable while PBE does not [40]. For compounds containing one transition metal ion there is improvement over PBE as well, especially for strongly bound cases (similar results were reported in [39]), where the error is smaller by 94% [40]. Weakly coupled systems show some improvement, which Liu et al. [39] did not observe. For the last three panels, SCAN improves the results for both completely filled d-shells but the case is much more complicated for partially filled d-shell by one or both ions [40].

One of the very important areas that metaGGAs propose improvements are the band gap energies. These are severely underestimated in GGAs due to the self-interaction errors and derivative discontinuity raising from the difference of Kohn-Sham band gap E_G^{KS} and

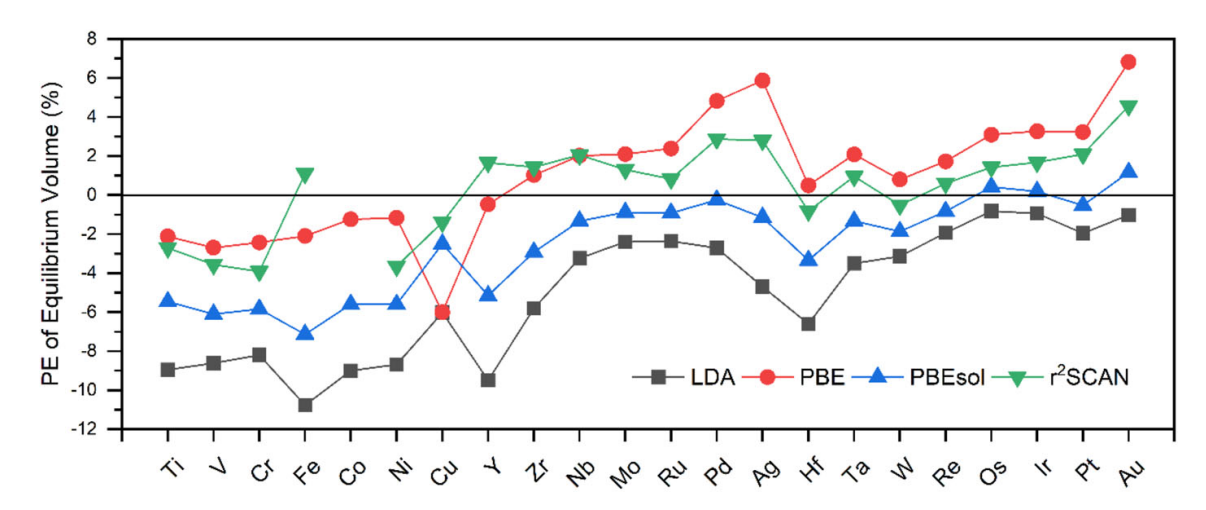


Figure 3.8: Percentage errors of equillibrium volume obtained via r²SCAN and other functionals [39].

the fundamental gap E_G of system with N electrons. Kohn-Sham band gap is a difference between the eigenvalues of conduction band minimum (CBM) and valence band maximum (VBM) while the fundamental band gap is difference between ionization potential I and electron affinity A.

$$E_G = I - A, (3.42)$$

$$E_G^{KS} = \epsilon_{CBM} - \epsilon_{VBM} \tag{3.43}$$

$$E_G = E_G^{KS} + \Delta_{xc}. (3.44)$$

Functionals LDA and GGA have the derivative discontinuity Δ_{xc} equal to zero. The metaG-GAs depend on orbitals via generalized Kohn-Sham formalism, as described in previous section Section 3.1.2, which is a direct approximation to the fundamental gap E_G . Borlido et al. [46] performed a thorough investigation of many different functionals via VASP to obtain the band gap accuracies. In their results they have shown most metaGGAs outperform GGAs in band gap accuracy. The SCAN functional has approximately halved the errors that PBEsol and PBE have and thus eliminating some of the underestimations. Most importantly, SCAN and r²SCAN have fixed the errors of PBE in Ge, where PBE predicts negative band gap, a semimetal with inverted band ordering. Using the metaG-GAs the band gap is now correctly ordered but still with underestimated values (0.385eV in comparison to experimental 0.74eV) [43]. Looking at the band gap values specifically in Figure 3.11, SCAN potential shows general increase of the band gap energy and opens some band gaps without the need of + U correction [43] but it is still not enough to exactly reproduce the experimental gap, although the potential for further improvements of metaGGAs is shown by the TASK functional, which was constructed specifically to represent the band gaps correctly and achieves very good fit [47] Figure 3.11.

Description of magnetism via metaGGAs is of a complicated nature [40], for some materials they provide improved results over PBE but for others PBE results are closer to the experiments. For Fe SCAN overestimates the magnetic moment by 17% while PBE underestimates it only by 2%. For Co the overestimation is 8%, which is closer to the experimental value than PBE [40]. On the other hand, SCAN successfully predicts the correct non-collinear magnetic configuration of α -Mn where GGA fails completely [19]. Despite that, the magnetic moments are overestimated and it was shown that SCAN prefers

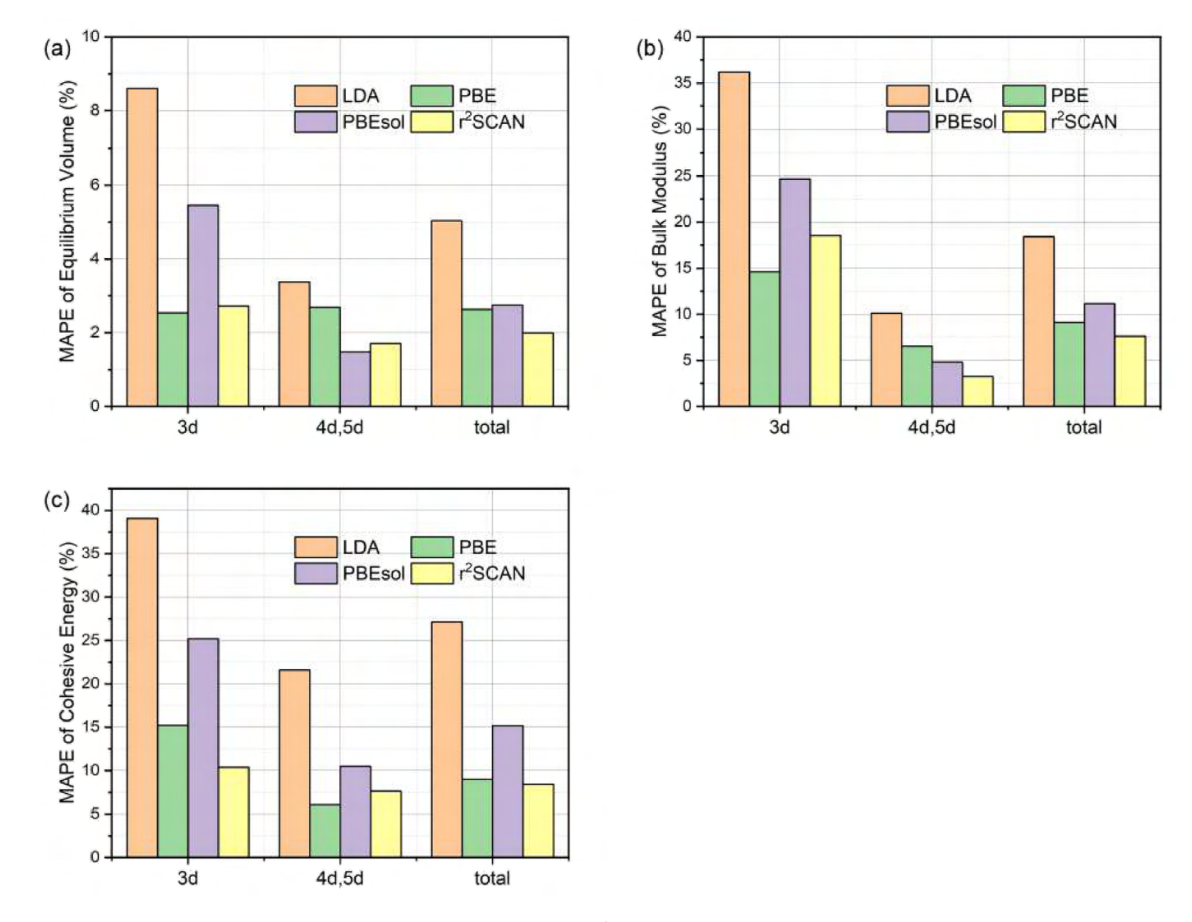


Figure 3.9: MAPE of r²SCAN taken from [39].

structures with large magnetic moments so there may be some exaggerated corrections in SCAN [40]. For Heusler alloys, SCAN overestimates the magnetic moment heavily for alloys with full metallic band structures, see Figure 3.12, while for the half-metallic Heusler alloys it mostly underestimates the magnetic moment [40].

Mejia-Rodriguez and Trickey examined the performance of deorbitalized functional SCAN-L in VASP [42] and found that the deorbitalized version reproduces the values obtained by the orbital-dependent version (SCAN) with basically no difference. Cohesive energies are reproduced similarly well [42], as well as the ground state configuration for all elements except Hf where one has to pre-relax with PBE and then continue with SCAN-L, probably because of the occupancies near the Fermi level of f elements [34]. Even for band gaps, the representation of the values from SCAN works well with only a few cases being slightly more underestimated [42]. Computational performance wise, Mejia-Rodriguez and Trickey [42] did calculations on diamond carbon in VASP with the same settings and SCAN-L is approximately 20% faster than the original SCAN. Tran et al. [41] did a similar study but in an all-electron code Wien2k. For strongly bound solids they have not found any difference to the results by Mejia-Rodriguez and Trickey [42] but for weakly bound rare gasses, the cohesive energy changes quite a lot [41]. Sokolovskiy et al. [40] reported on a machine-learned deorbitalized SCAN but it results in slightly worse performance than the analytical deorbitalization done by Mejia-Rodrigez and Trickey [34].

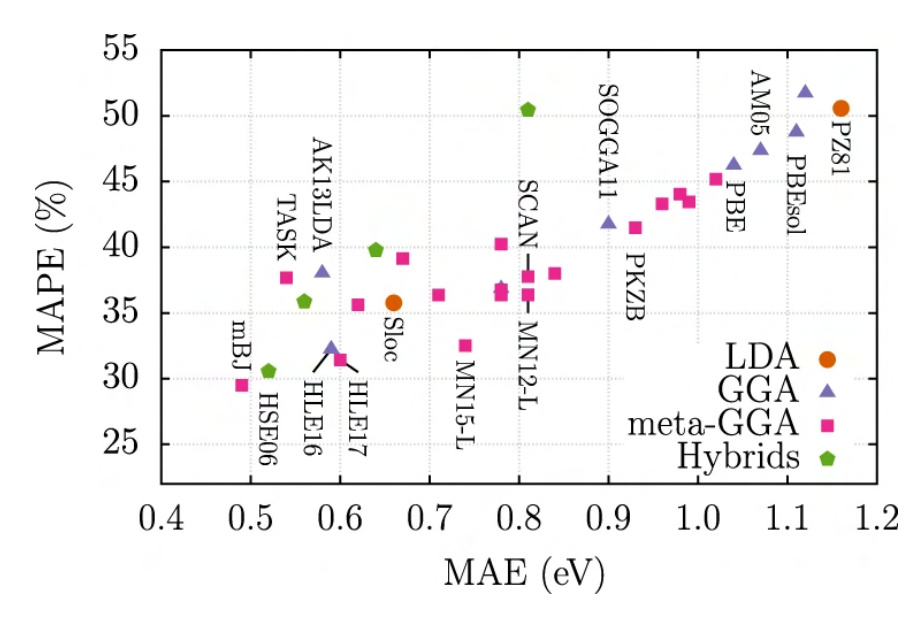


Figure 3.10: MAPE and MAE in determination of band gaps taken from [46]

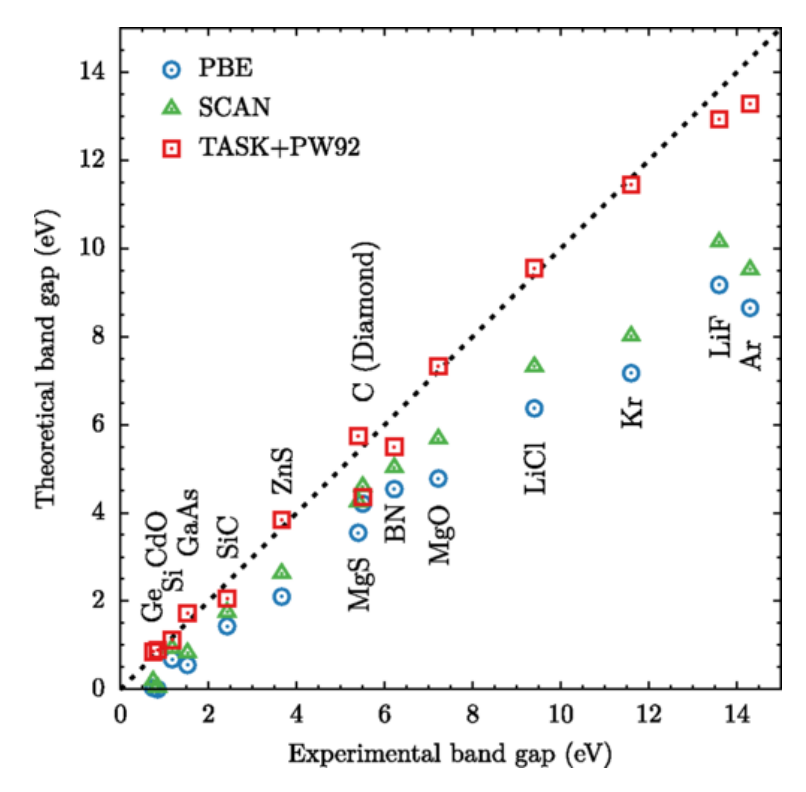


Figure 3.11: Comparison between TASK, SCAN metaGGAs and PBE functional for band gap accuracy taken from [47]

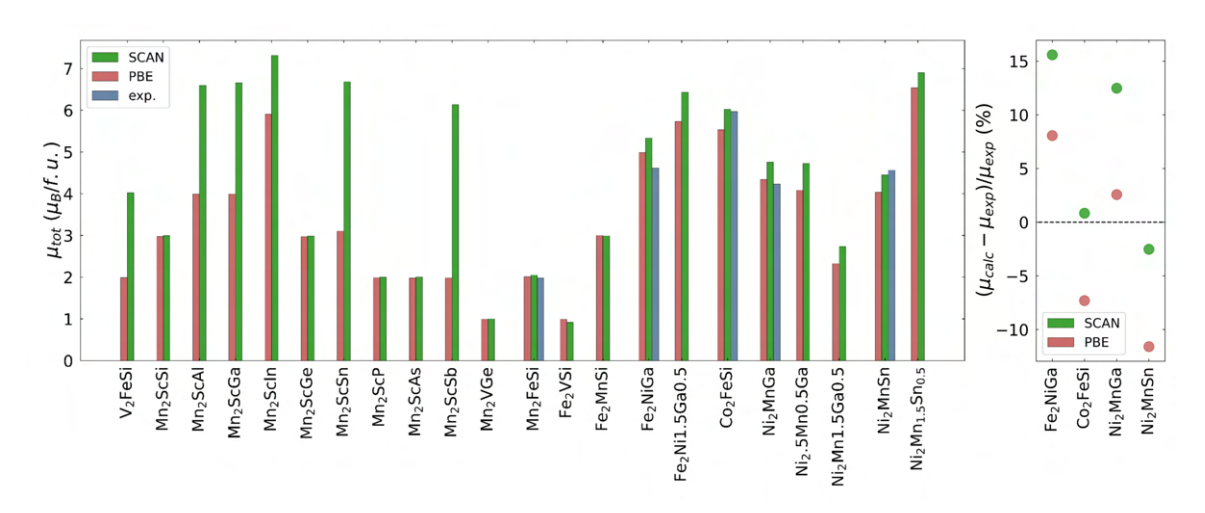


Figure 3.12: Comparison between SCAN and PBE in accuracy of magnetic moment prediction, taken from [40]

3.4 Thermodynamics for modelling

3.4.1 General definitions

Even though the DFT works in principle at T=0 K, thermodynamics is still important to use. The first law of thermodynamics describes the change in internal energy based on the heat Q absorbed or released as well as work W done as:

$$dU = \delta Q - \delta W, \tag{3.45}$$

where U refers to the internal energy of the system [1, 22]. The heat can be related to the entropy S. For reversible transformation the heat is dQ = TdS, where T is the temperature. Systems are usually defined by fixing one of the variables out of the (T, S) and (p, V) pairs thus getting four different thermodynamic properties - internal energy U(V, S), enthalpy H(p, S), Helmholtz free energy F(V, T) and Gibbs free energy G(p, T) all in units of J/m^3 . Entropy is given by second law of thermodynamics and for every reversible transformation it is:

$$dS = \frac{1}{T}\partial Q. \tag{3.46}$$

For irreversible transformations the entropy will always increase [22]. Entropy has many contributions like configurational, excess, magnetic and others. One definition for entropy can be tied to a probability p_i of a system occupying a state i with energy E_i at temperature T [2]:

$$S = -k_B \sum_{i} p_i \ln p_i, \tag{3.47}$$

where k_B is the Boltzmann constant. The variation of entropy with temperature can be taken from the specific heat C_p from classical thermodynamics:

$$S = \int_0^T \frac{C_p}{T} dT. \tag{3.48}$$

For the other two properties for fixed temperature F = U - TS and G = F - TS thus:

$$dF = -pdV - SdT, (3.49)$$

$$dG = Vdp - SdT. (3.50)$$

The value of total energy received from a DFT calculation has little physical meaning and it is thus needed to get either the formation energy E_F or the mixing enthalpy H_{mix} . The formation energy of compound is obtained from the total energy of the compound AB and then the total energy of the elements A and B in their ground state. The formation energy is obtained in eV per atom as:

$$E_{F,AB} = \frac{E_{tot,AB} - (n_A E_{tot,A} + n_B E_{tot,B})}{n_{AB}},$$
(3.51)

where the n_A and n_B is the amount of atoms of their respective elements in the computational cell of the studied material, n_{AB} is the total amount of atoms of all elements in the computational cell of the studied material and $E_{tot,AB}$, E_{tot_A} , E_{tot_B} are the total energies of the compound, ground states of elements A and B respectively. For more elements the approach is the same with additional terms corresponding to the remaining elements. Even

though formation energy and mixing enthalpy can have different physical and chemical meaning, the approach to gain the mixing enthalpy from the DFT results is completely the same (at $T=0~\rm K$) with the difference of units as the enthalpy is in kJ/mol:

$$H_{mix}^{AB} = E_{F,AB} \times N_A \times 1.602176565 \times 10^{-22},$$
 (3.52)

where N_A is the Avogadro number $(6.023 \cdot 10^{23})$ and the last term is the conversion from eV to kJ.

3.5 Modelling different levels of ordering

One of the most popular methods to simulate disordered alloys for ab initio calculations is the Special Quasirandom Structures (SQS) method. It imitates the random distributions of atoms on crystallographic sites, while it is also possible to choose selective occupation of the lattice sites. As the interactions between the distant neighbours generally influence the total energy less than between the close neighbours, the SQS principle works on close reproduction of random network for the first few neighbour shells only [48].

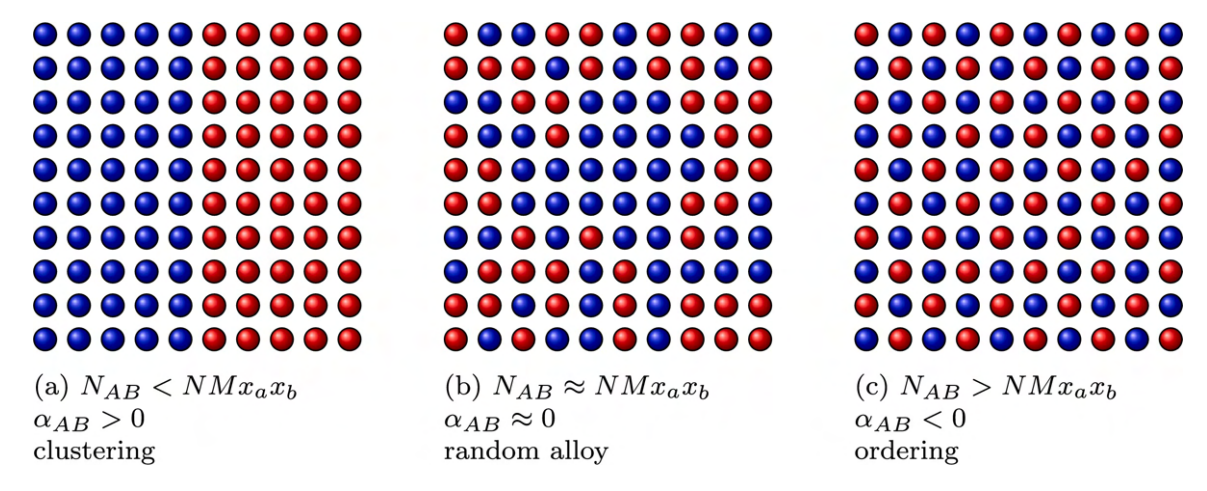


Figure 3.13: Different values of Warren Cowley parameters and what they represent in the structure [49].

To efficiently generate structures that are compositionally complex, like high entropy alloys, a tool sqsgenerator made by D. Gehringer *et al.* [49] was used. It uses the Warren-Cowley parameter (Equation (2.1)) to describe the nearest neighbour for a selected lattice sites, although the formula is used in generalized form taking into account multiple coordination shells [49]

$$\alpha_{\xi\eta}^{i}(\sigma) = 1 - \frac{N_{\xi\eta}^{i}(\sigma)}{NM^{i}x_{\xi}x_{\eta}}.$$
(3.53)

Here $N_{\xi\eta}$ is the number of $\xi-\eta$ pairs, N is the number of lattice sites, M is the number of neighbours for the given site, the value of the index i indicates the nearest neighbour shell (i. e. 1 - first, 2 - second etc.) and the x_{ξ}, x_{η} are the mole fractions of their specific element in index. The parameters are then mapped to a function which is used for minimization either by employing the Monte Carlo approach or a systematic approach, which generates permutation of small cells.

3.6 Molecular Dynamics

3.6.1 General definition

Molecular dynamics (MD) is a method to simulate materials at finite temperatures with all atoms in motion. The simulation boxes now usually include many more atoms than what DFT can simulate. It treats the atomic nuclei as classical Newtonian particles [4] instead of quantum particles which is the case in DFT. They follow the equation of motion:

$$m^{\alpha}\ddot{r}^{\alpha} = \mathbf{f}^{\alpha}, \alpha = 1, ..., N, \tag{3.54}$$

where N is the number of atoms, m^{α} is the mass of atom α , r^{α} is the position of atom α and \mathbf{f}^{α} is the time-dependent force acting on atom α due to external effects and neighbours [4]. This time dependence enforces a limit of maximal simulation time, usually in units of nanoseconds [4, 50, 51]. The forces are given by [4]:

$$f^{\alpha} = -\frac{\partial \mathcal{V}}{\partial r^{\alpha}},\tag{3.55}$$

where \mathcal{V} is the potential energy of the system that consists of internal part reflecting the interactions between atoms making up the system and external part reflecting external fields and constraints. With descibed forces acting on atoms, their motion can be obtained by integrating the equation of motion. The temperature in the simulation box can be monitored as an output as the time-averaged vibrational kinetic energy of the system [4]:

$$T = \frac{2}{3Nk_B}\overline{T_{\text{vib}}} = \frac{2}{3Nk_B}\sum_{\alpha=1}^{N} \frac{1}{2}m^{\alpha}||v_{rel}||^2,$$
 (3.56)

where v_{rel}^{α} is the velocity of atom α relative to the center of mass velocity. Instantaneous temperature can also be obtained based on the instantaneous vibrational energy of the system, which is not the true temperature, as that can only be obtained as the average, but will fluctuate around the true temperature [4]:

$$T_{inst}(\boldsymbol{v}_{rel}) = \frac{2}{3Nk_B} \left(\sum_{\alpha=1}^{N} \frac{1}{2} m^{\alpha} ||\boldsymbol{v}_{rel}^{\alpha}||^2 \right). \tag{3.57}$$

The approach is always tied to an interatomic potential representing the forces acting on ions - a force field - however, sometimes the accuracy can be unsatisfactory, for example lacking the polarization effects [50]. A solution to this can be a combined approach - ab initio molecular dynamics (AIMD) which combines the electronic structure calculations with finite temperature MD [50]. These calculations are however very computationally expensive and lately could be pushed away by machine learning approaches described further in Section 3.7.

The flow chart of a typical MD run can be seen in Figure 3.14. Initial step 0 requires the given structure, periodic boundary conditions and velocities of atoms - the temperature of simulation box. Then the main integration loop of equations of motions goes through until the set simulation time (t_{max}) passes. Depending on the desired results the simulation may require a period of time to equilibrate the system before collecting the data so the "equilibrated?" decision has to be implemented (see Figure 3.14). Throughout the integration there are three main steps of the simulation, first the potential and kinetic energies

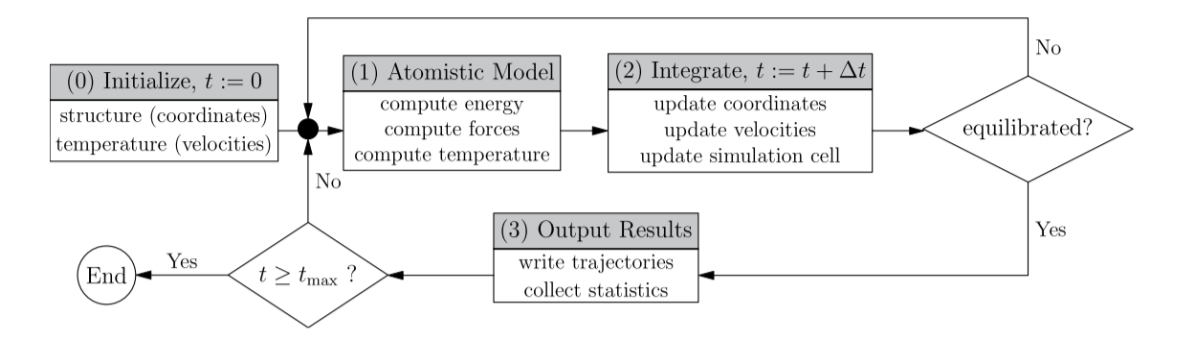


Figure 3.14: General flow chart of a Molecular Dynamics run taken from [4].

are evaluated and the forces acting on ions are calculated based on the initial positions and velocities, this is dependent on the force model used. Second step is the update of coordinates and velocities of atoms according to the integration algorithm. If allowed, the shape and size of the simulation box can change as well. Finally, the third step provides the output of the simulation, i. e. collection of statistical data of the MD run like temperatures, stresses, trajectories for visualization etc. How these steps are undertaken depends on the used ensemble [4].

3.6.2 Ensembles

Different ensembles are commonly denoted via the state variables that are set to constant. The easiest ensemble to employ is the NVE ensemble with constant number of atoms N, volume V and energy E [4]. This is basically an isolated system in statistical mechanics called a microcanonical ensemble. The total energy given by the Hamiltonian, that is dependent on the kinetic and potential energy, is kept constant for the whole MD run. Though this ensemble is a bit further away from real experiments and the applicability is then limited [4, 51].

Another commonly used ensemble is the canonical NVT ensemble with constant temperature T instead of energy E. Here another dependency arises, the so-called thermostat to keep the simulation box temperature at the desired value [4]. Langevin thermostat is one of the more commonly used ones. It incorporates random forces into the equation of motion to represent a heat bath, i. e. heat transfer between free electron gas in a solid metal crystal [4]. The random numbers for the forces are chosen from Gaussian distribution [8]. Similar approach is the Andersen thermostat, which imposes the random forces as well, but only for small number of time steps and at random intervals [4]. Another common thermostat is the Nosé-Hoover thermostat [4]. It is a different approach than the previously described thermostats called extended system method [4]. The basic principle of this method is an introduction of fictious particles with their own positions and momentum and determine the equation of motion for a system containing them. This requires a reality check of the system after the run to see if it behaves in accordance to physical reality [4]. Both Langevin and Nosé-Hoover have one free parameter, the damping coefficient and the mass of the fictious atoms, respectively. Careful selection of these is needed to obtain good results [4]. Nosé-Hoover can also suffer from incomplete sampling of phase space which can be mitigated by using a so-called chain of thermostats where a single thermostat particle

is replaced by a chain of particles [4, 8]. This ensemble is closer to experimental conditions and one can simulate ion diffusion in solids, reactions on slabs and clusters [50].

The last commonly used ensemble is the isothermal-isobaric NPT ensemble - constant pressure at constant temperature. Similarly to thermostats in previous ensembles, here arises the need for a barostat. Usually user sets up only one and it tries to control both the pressure and the temperature [52]. These methods usually include the Parinello-Rahman [8] or Berendsen barostats [52]. The Parinello-Rahman barostat is similar to Nosé-Hoover thermostat in principle, there is now a related system with its own pressure and temperature that then modifies the equations of motion [51]. The phenomena that can be simulated via this ensemble include for example thermal expansion, melting point predictions and phase transitions in solids [51].

3.6.3 **LAMMPS**

The code used in this work to perform MD runs was LAMMPS (Large-scale Atomic/Molecular Massively Parallel Simulator). It uses spacial decomposition techniques to parallelize simulations and cut the computational time quite significantly [52]. Especially, over the last few years with hardware development (mostly GPUs) the MD simulations received huge speedups and thus increase in popularity [52]. It is possible to simulate with manybody potentials, longer length and time scales via coarse grained models, but most importantly for this work, it is possible to use machine learning interatomic potentials (Section 3.7). Furthemore, LAMMPS contains a variety of Monte Carlo techniques that allow exploration of different configurations via randomly generated moves that then get either accepted or rejected in dependence on the potential energy change [52]. Multiple ensembles are included in the package, all the previously described ones plus NPT, NPH as well as grand canonical, which keeps constant chemical potential instead of number of atoms. They are set up together with a thermostat or barostat with a command fix [52]. For simulation of magnetic materials LAMMPS contains a SPIN package that allows either spin dynamics or coupled spin and lattice dynamics [52]. It allows variety of spin-lattice Hamiltonians to be constructed and the user input is then a unit vector of classical spin $\vec{s_i}$. The coupled spin and lattice dynamics is approximately only 4 times slower than classical MD run with an embedded atom method potential (EAM) [52]. There is also an option to apply external magnetic fields and to apply a spin thermostat, which transforms the equations of motion into a classical Landau-Lifshchitz equation [52]. To visualize results the package offers its own GUI or one can use third party applications like Ovito [52, 53].

3.7 Machine Learning Interatomic Potentials

In recent years there has been a boom in the field of machine learning potentials that learn the potential energy surface from available DFT data. This has been allowed by the works of Behler and Parinello in 2007 on artificial neural networks [54] as well as Bartók et al. in 2010 on Kernel-based approaches [55] and combined with hardware advancements, especially GPUs [21]. Typically, the machine learned potentials (MLPs) are composed of two components, an encoding of the molecular structure, *i. e.* the descriptors, and a regression technique that maps the atomic configurations onto the potential energy surface [21]. These potentials are trained on some database of electronic structure calculations, of which there are now many different ones, and then they can be used to extrapolate or interpolate new results. The difference between extrapolation and interpolation lies within

the examined problem. If the examined configurations are similar to the data the model was trained on, it is interpolation. On the other hand, the more interesting application is extrapolation, where the examined configurations are significantly different than the training data [21]. Generally, extrapolation can lead to some untrue or even unphysical results, so one needs to be careful [21].

The descriptors can exploit some intrinsic properties of the PES dependence on structure, like translational and rotational symmetries as well as invariance to permutations, as the order of the atoms does not matter as long as it is the same atoms. To describe the chemical structure multiple methods can be employed, simply using atomic Cartesian coordinates or a $N \times N$ matrix of atomic distances in the system or their inverse - the Coulomb matrices [21].

The originally popular descriptors (Smooth Overlap of Atomic Positions and Atom-Centered Symmetry Functions, SOAP and ACSFs respectively) suffer from some shortcomings. They both have unfavourable scaling with the number of species in the system with limits of 5 to 6 different chemical species [21]. A solution to this is introducing element-dependent weighing functions into the descriptors instead of using separate functions to describe the combinations of elements [21]. Additional issues arise from the basic definition of the descriptors. They are limited by the set cutoff and thus result in a short range description. This can pose a big problem for systems where the long range interactions, such as Coulomb interactions, are important as these models by definition cannot include them [21]. Some models make the descriptors part of the machine learning process as in message-passing neural networks (MPNNs) [21].

After the descriptors are set, the actual learning of their relation to PES starts via regression [21]. This means that an actual physical property, e. q. atomic energy, is now being put onto these descriptors, which up until now just describe the lattice. The two most common approaches are neural networks and kernel-based methods [21] (Figure 3.15). The artificial neural networks are based on layers of connected nodes and associated weights. Input layers hold the provided mathematical description of the input (descriptors) and are connected to the output layers via so-called hidden layers. Behler and Parinello [54] solved the computational inefficiency of direct input of descriptors by representing every element type of the system by a separate neural network [21, 54]. The output layers contain the potential energy associated with the input [21]. Additional bias nodes can be included to all nodes except the input nodes which serve as an adjustable shift via bias weights b[21]. The evaluation of a node value is in principle a linear dependence on all node values of the previous layer that is activated by an activation function f_i^j [21]. This function is usually a sigmoid function in the hidden layers and introduces the flexibility of the network by fitting arbitrary functional forms to previously linear information [21]. The predictions then happen via forward-passing of the input information through the different layers of the network. In the Behler and Parinello neural network, the total potential energy of a particular configuration gets separated into sums of the contribution of individual atoms to construct a relation to the output and atomic configurations [54]:

$$E_{tot} = \sum_{i=1}^{N_{atom}} E_i = \sum_{s=1}^{N_{ele}} \sum_{i_s=1}^{N_{atom_s}} E_{NN_s}(G_{i_s}).$$
 (3.58)

In this each atomic configuration for element s out of the total number of elements N_{ele} is represented by a single neural network E_{NN} shared for all atoms of that element N_{atom_s} . This enables systems of different sizes to be represented by the same model as well as

applying the trained model to a larger system [21, 54]. This model is again inherently local as the total potential energy is tied only to the atoms in the cutoff radius [21]. This approach is called high-dimensional neural network [21, 54].

Obtaining forces from trained energies is not as straightforward as from DFT. Since the coordinates have been transformed into symmetry functions, the Cartesian coordinates need to be regained from Equation (3.58) [21]. In modern machine learning libraries the partial derivation of energy by the Cartesian coordinate α can be obtained just by calling a "backdrop" function that goes through backpropagation in the neural network [21]. Calculating the derivation takes a few more steps but after it the forces are recovered. Similar approach can be used to obtain the stress tensor via another suitable partial differentiation [21].

The training on this model is then done by minimizing the loss function L comparing the reference and the model's predicted energies [21]:

$$L = \frac{1}{2N} \sum_{i=1}^{N} (E_i^{ref} - E_i^{model})^2.$$
 (3.59)

This loss function can also be enhanced by including forces which usually leads to improved fits as they provide additional information about the shape of the PES as well as simply increasing the information content of a single configuration quite heavily [21]. The loss function is minimized by changing the weights in the neural network via some optimization technique, e. g. steepest descent [21]:

$$w_{new} = w_{old} - \eta \frac{\partial L}{\partial w_{old}},\tag{3.60}$$

where w_{old} and w_{new} are the old and new weights respectively and η is an adjustable learning rate. The quality of the fit is then evaluated by comparison to a testing set which can provide an estimate for the transferability as it can include structures not contained in the training set [21].

Kernel based methods have some similarities to the neural networks. The total energy is again decomposed into a sum of the atomic energies like in Equation (3.58) but here the atomic energies are calculated via linear combination of d-dimensional terms [21, 55]:

$$E_{tot} = \delta^{(2B)} \sum_{ij} E^{(2B)} (\mathbf{q}_{ij}^{(2B)}) + \delta^{(MB)} \sum_{i} E^{(MB)} (\mathbf{q}_{i}^{(MB)}).$$
(3.61)

This involves two-body terms (2B) and many-body terms (MB) which are represented as separate Gaussian process regression [21] with their suitable descriptors q^d . Each term is also weighted by a scaling factor $\delta^{(d)}$ which then acts as an additional hyperparameter. Usually, the two-body term has the largest contribution to the energy and is set up five to fifty times larger than the many-body terms [21]. The two-body term uses descriptor of a distance between two atoms while the many-body terms uses the SOAP kernel [21]. Inputing a set of the SOAP configurations leads to this expression for energy [21]:

$$E_{tot} = \delta^{(2B)} \sum_{ij} \sum_{m=1}^{M^{(2B)}} c_m^{(2B)} \exp\left[-\frac{|R_{ij} - R_m|^2}{2\theta^2}\right] + \delta^{(MB)} \sum_i \sum_{m=1}^{M^{(MB)}} c_m^{(MB)} (\boldsymbol{\xi}_i \cdot \boldsymbol{\xi}_m)^{\zeta},$$
(3.62)

where θ is a hyperparameter related to the two-body descriptor, ξ is the normalized power spectrum vector from SOAP, $c_m^{(d)}$ are the coefficients of the individual Gaussian regression

models that are obtained during the fitting process. The Gaussian regression then again minimizes a loss function [21]:

$$\mathcal{L} = [\boldsymbol{y} - \boldsymbol{K}_{NM} \boldsymbol{c}]^T \boldsymbol{\Sigma} [\boldsymbol{y} - \boldsymbol{K}_{NM} \boldsymbol{c}] + \boldsymbol{c}^T \boldsymbol{K}_{MM} \boldsymbol{c}, \tag{3.63}$$

where K_{NM} is the kernel matrix which represents the similarity between each pair of input locations and Σ is a diagonal matrix composed of regularisers σ_n . The regulariser choice depends on multiple factors, e.~g. the property that is being modelled, location in the phase space. Since VASP is used in this work it has to be mentioned that VASP employs a kernel based on-the-fly machine learning method built upon modified SOAP descriptors [56, 57]. These allow the user to train their own force fields for the specific problems and are thus not universal. On the other hand, they have an advantage of using whatever settings the user wishes to, like different functionals that may not be contained in the databases. Unfortunately, it does not learn and thus cannot predict magnetic moments similarly to other universal machine learning potentials (UMLIPs). The interface with other MD simulation codes is also very recent and still in beta version, so the transferability is also slightly worse.

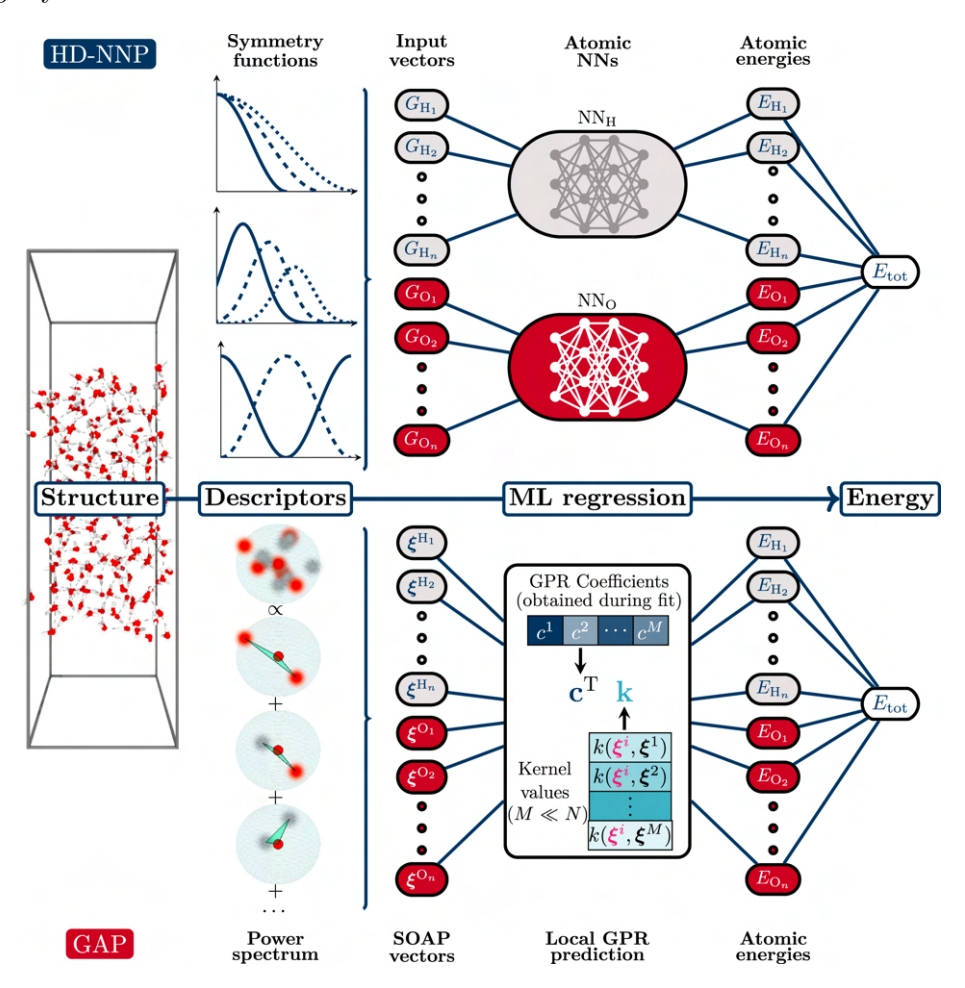


Figure 3.15: Schematic of the two described methods for the description of slab of water - High-Dimensional Neural Network and Gaussian approximation potential [21].

Another approach is the Atomic Cluster Expansion (ACE) [58]. This approach takes the atomic energy in a many-body expansion expression [58]:

$$E = V_0 + \sum_{i} V^{(1)}(\boldsymbol{r}_i) + \frac{1}{2} \sum_{ij} V^{(2)}(\boldsymbol{r}_i, \boldsymbol{r}_j) + \frac{1}{3!} \sum_{ijk} V^{(3)}(\boldsymbol{r}_i, \boldsymbol{r}_j, \boldsymbol{r}_k) \dots,$$
(3.64)

where $V^{(i)}$ are the chemical potentials and V_0 is a constant offset. Generally, this expansion has unfavourable scaling and performance [21, 58]. The difference begins at the local descriptors based on the spin cluster expansion [58] by introducing basis functions $\phi_v \mathbf{r}$ for the expansion of energy that depend only on a single bond \mathbf{r} . Combining these bond basis functions into a cluster α with a basis function $\Phi_{\alpha v}$ that contains \mathbf{K} elements. From this a kernel may be obtained and the expansion can be modified by it [58]. After including the invariance to permutation the atomic energy from Equation (3.64) can be rewritten as [58]:

$$E_{i}(\boldsymbol{\sigma}) = \sum_{v} c_{v}^{(1)} A_{iv} + \sum_{v_{1}v_{2}}^{v_{1} \geq v_{2}} c_{v_{1}v_{2}}^{(2)} A_{iv_{1}} A_{iv_{2}} + \sum_{v_{1}v_{2}v_{3}}^{v_{1} \geq v_{2} \geq v_{3}} c_{v_{1}v_{2}v_{3}}^{(3)} A_{iv_{1}} A_{iv_{2}} A_{iv_{3}} + \dots,$$
 (3.65)

where A_{iv} are the atomic bases, *i. e.* the projections of basis functions on the atomic density, and $c_v^{(K)}$ are the expansion coefficients. The computational cost to construct the atomic base scales linearly with the number of neighbours, while the evaluation of the energy is independent of them. This results in independence on the order of expansion that overcomes the poor scaling of the original expression [58]. To satisfy the radial and angular symmetry functions, an appropriate single-bond basis function has to be set that result in the final equation for the energy as [58]:

$$E_i(\boldsymbol{\sigma}) = \sum_{Knl} c_{nl}^{(K)} \boldsymbol{B}_{inl}^{(K)}, \qquad (3.66)$$

where \boldsymbol{B} is the product of atomic base reduction that takes into the account the invariance. Forces may be obtained with similar efficiency as the energy by derivation of the energy [58]. It should be noted that the basis functions are quite similar in principle to the symmetry functions described above and some can even be expanded into the basis functions [58]. Similarly, SOAP descriptors can be expressed in the atomic cluster expansion terms kernel but they neglect self-interaction corrections [58].

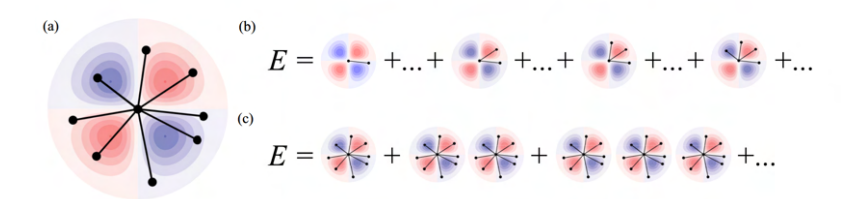


Figure 3.16: Example of the ACE methodology, taken from [58].

Another option for machine learning potentials is to use the molecular graphs and fit them upon the graph neural networks (GNN). The graphs are constructed from nodes=atoms and edges connecting them to other atoms [21]. Each atom is associated with a latent state h_i that gets updated with each message-passing iteration t [21]. Message m_i^{t+1} is constructed on a node i by "pulling" the information about the states from all neighbouring

atoms $N_{(i)}$ connected via edges e_{ij} using the message function [21]:

$$m_i^{t+1} = \sum_{j \in N_{(i)}} M_t(h_i^{(t)}, h_j^{(t)}, e_{ij}).$$
(3.67)

The updated state can be expressed via equation [21]:

$$h_i^{t+1} = U_t(h_i^t, m_i^{(t+1)}), (3.68)$$

where U_t is a learnable node update function. Unlike the previous models the GNNs can contain semi-local information via the message passing although it will increase the computational cost significantly, especially if not implemented well [21].

Recent progress leads to advances in the more promising part - universal machine learning potentials (UMLIPs). These potentials employ the descriptors and training methods described in previous section. They take huge datasets from different published databases of quantum mechanical calculations, train on them and promise accurate extrapolation to systems it may have not encountered in the training [21]. The most used datasets are the MPtrj dataset [59], Alexandria database [60, 61] and recently completed OMaT24 database by META [62] which contains more than a 100 million calculated structures [62]. The limitations of these models are usually brought on by those databases, *i. e.* if the database has calculations done only with PBE, then the model will run into the same issues described in Section 3.1.2. For most cases of these problems, *e. g.* underestimated band gaps, that is not a problem, as the models are mostly not trained on more than energies and forces, but in the future a need for a more accurate exchange-interaction functional database may raise. This also gives a goal for the future - to train a model that will be able to predict the charge distribution as well as its derivatives [21].

In case the universal model fails to predict the correct structures, the big advantage of some of the UMLIPs is the option to refit/retrain the model. This means that the pretrained universal model can be further trained on the specific problem that the user is interested in. The required number of calculations that need to be included in refit can be quite low. Žguns et al. [63] found out that lower tens of additional calculations to retrain the CHGnet and MACE [59, 64] are more than enough to get the model accuracy to the level of DFT accuracy. As the number of these models keeps increasing, there arises a need to benchmark/compare them, and for that a Materials Project benchmark was set-up called the Matbench Discovery [65]. It compares the models performance (speed and accuracy) in multiple scenarios, where the accuracy is evaluated primarily with phonon predictions, as that requires very accurate forces prediction. At the moment of writing, there is only one model in the leaderboard that can predict magnetic moments - CHGNet (see Figure 3.17). One important thing to notice is the "Date Added" column, where one can see how dynamic this field is. New models or new databases appear quite frequently and if one wants to use the best state-of-the-art model, it may change in a month. On the other hand some models, like GRACE, already achieve the error levels of DFT and thus a better model will not cause a huge difference in accuracy, but may be better in performance. One more thing about magnetism has to be mentioned, its influence is inherently obtained in the models as they are usually trained on calculations with spin-polarization enabled. Thus the prediction of nonmagnetic/magnetic phase stability should be correct purely based on the expected volumes. And of course, none of the databases are done with anything else than GGA PBE or PBEsol functionals, so if one wants to use metaGGAs they have to train their own models, for example via VASP [56, 57].

| Model | r _{cut} | Date Added | Targets | Params | Training Set | RMSD ↓ | K _{SRME} ↓ | R ² ↑ | MAE ↓ | Prec ↑ | DAF ↑ | F1 ↑ | Acc ↑ | CPS 1 |
|---------------------|------------------|------------|---------|--------|--------------------------------|--------|---------------------|------------------|-------|--------|-------|-------|-------|-------|
| eSEN-30M-OAM | 6 Å | 2025-03-17 | EFSG | 30.2M | 6.6M (113M) OMat24+MPtrj+sAlex | 0.061 | 0.170 | 0.866 | 0.018 | 0.928 | 6.069 | 0.925 | 0.977 | 0.888 |
| ORB v3 | 6Å | 2025-04-05 | EFSG | 25.5M | 6.47M (133M) MPtrj+Alex+OMat24 | 0.075 | 0.210 | | 0.024 | 0.904 | 5.912 | 0.905 | 0.971 | 0.861 |
| SevenNet-MF-ompa | 6Å | 2025-03-13 | EFSG | 25.7M | 6.6M (113M) OMat24+sAlex+MPtrj | 0.064 | 0.317 | 0.867 | 0.021 | 0.890 | 5.825 | 0.901 | 0.969 | 0.845 |
| GRACE-2L-OAM | 6Å | 2025-02-06 | EFSG | 12.6M | 6.6M (113M) OMat24+sAlex+MPtrj | 0.067 | 0.294 | 0.862 | 0.023 | 0.883 | 5.774 | 0.880 | 0.963 | 0.837 |
| AlphaNet-v1-OMA | 5 Å | 2025-05-12 | EFSG | 4.65M | 6.6M (113M) OMat24+sAlex+MPtrj | 0.032 | 0.644 | 0.868 | 0.020 | 0.883 | 5.777 | 0.909 | 0.971 | |
| DPA-3.1-3M-FT | 6Å | 2025-06-05 | EFSG | 3.27M | 163M OpenLAM | 0.069 | | 0.869 | 0.023 | 0.866 | 5.667 | 0.884 | 0.963 | |
| eSEN-30M-MP | 6 Å | 2025-03-17 | EFSG | 30.1M | 146k (1.58M) MPtrj | 0.075 | 0.340 | | | 0.804 | 5.260 | | | |
| MACE-MPA-0 | 6 Å | 2024-12-09 | EFSG | 9.06M | 3.37M (12M) MPtrj+sAlex | 0.073 | 0.412 | 0.842 | | 0.853 | 5.582 | | 0.954 | |
| MatterSim v1 5M | 5 Å | 2024-12-16 | EFSG | 4.55M | 17M MatterSim | 0.073 | | 0.863 | 0.024 | 0.895 | 5.852 | | 0.959 | 0.767 |
| GRACE-1L-OAM | 6Å | 2025-02-06 | EFSG | 3.45M | 6.6M (113M) OMat24+sAlex+MPtrj | 0.072 | | 0.842 | | 0.803 | 5.255 | 0.824 | | 0.761 |
| Eqnorm MPtrj | 6 Å | 2025-05-26 | EFSG | 1.31M | 146k (1.58M) MPtrj | 0.084 | 0.408 | 0.799 | 0.040 | 0.741 | 4.844 | 0.786 | | 0.756 |
| DPA-3.1-MPtrj | 6 Å | 2025-06-05 | EFSG | 4.81M | 146k (1.58M) MPtrj | 0.080 | 0.650 | | | 0.768 | 5.024 | 0.803 | | 0.718 |
| SevenNet-I3i5 | 5 Å | 2024-12-10 | EFSG | 1.17M | 146k (1.58M) MPtrj | 0.085 | 0.550 | 0.776 | 0.044 | 0.708 | 4.629 | 0.760 | 0.920 | 0.714 |
| MatRIS v0.5.0 MPtrj | 6 Å | 2025-03-13 | EFSGM | 5.83M | 146k (1.58M) MPtrj | 0.077 | 0.861 | | | 0.772 | 5.049 | 0.809 | | 0.681 |
| GRACE-2L-MPtrj | 6 Å | 2024-11-21 | EFSG | 15.3M | 146k (1.58M) MPtrj | 0.090 | 0.525 | 0.741 | 0.052 | 0.636 | 4.163 | 0.691 | 0.896 | 0.681 |
| MACE-MP-0 | 6Å | 2023-07-14 | EFSG | 4.69M | 146k (1.58M) MPtrj | 0.091 | 0.647 | 0.697 | 0.057 | 0.577 | 3.777 | 0.669 | 0.878 | 0.644 |
| eqV2 M | 12 Å | 2024-10-18 | EFSD | 86.6M | 3.37M (102M) OMat24+MPtrj | 0.069 | 1.771 | 0.848 | 0.020 | 0.924 | 6.047 | 0.917 | 0.975 | 0.558 |
| ORB v2 | 10 Å | 2024-10-11 | EFSD | 25.2M | 3.25M (32.1M) MPtrj+Alex | 0.097 | 1.732 | 0.824 | | 0.924 | 6.041 | 0.880 | 0.965 | 0.529 |
| eqV2 S DeNS | 12 Å | 2024-10-18 | EFSD | 31.2M | 146k (1.58M) MPtrj | 0.076 | 1.676 | 0.788 | 0.036 | 0.771 | 5.042 | 0.815 | | 0.522 |
| ORB v2 MPtrj | 10 Å | 2024-10-14 | EFSD | 25.2M | 146k (1.58M) MPtrj | 0.101 | 1.725 | 0.756 | 0.045 | 0.719 | 4.702 | 0.765 | 0.922 | 0.470 |
| M3GNet | 5 Å | 2022-09-20 | EFSG | 228k | 62.8k (188k) MPF | 0.112 | 1.412 | 0.585 | 0.075 | 0.441 | 2.882 | 0.569 | 0.813 | 0.428 |
| CHGNet | 5 Å | 2023-03-03 | EFSGM | 413k | 146k (1.58M) MPtrj | 0.095 | 1.717 | 0.689 | 0.063 | 0.514 | 3.361 | 0.613 | 0.851 | 0.400 |
| GNoME | 5 Å | 2024-02-03 | EFG | 16.2M | 6M (89M) GNoME | n/a | n/a | 0.785 | 0.035 | 0.844 | 5.523 | 0.829 | 0.955 | NaN |

Figure 3.17: Current status of the Matbench Discovery leaderboard (May 2025) [65].

3.7.1 CHGNet

CHGNet is a universal machine learning potential that employs the Graph Neural Networks described in previous section. It is trained on the Materials Project Trajectory Database (MPtrj) [59]. The atomic structures are taken in as graph descriptors, where there is a search from node in a set up cutoff radius of 3 Å for neighbouring atoms. Here, an additional step is performed, a "charge decorated" structure is created which estimates the charges on the atoms [59]. After neighbouring atoms are found, the edges are drawn and then the basis expansion is done as described in ACE section previously. It takes crystal structure with unknown charges as an input and provides prediction of energies, forces and magnetic moments. The neural network regularizes the node feature v_i^{t-1} at the convolution layer to preserve the magnetic moment information. This convolution layer then contains not only information about magnetic moments, but about charge distribution as well, which results in the predicted values of energy, forces and stresses to be charge constrained. The prediction is again done by minimizing the loss function, which contains energy, forces, stresses as well as magnetic moments in a weighted sum. The magnetic moments are the culprits for charge prediction as well. As was described in Section 3.2 it is the difference between spin-up and spin-down localized electrons [59]. So in a sense, this model "cheats" around the learning of charge distribution and instead approximates it from the other way, the known magnetic moments. This of course leads to some concern about accuracy for non-magnetic materials as where there is no magnetic moment, the model basically has no information about the charge distribution [59]. On the other hand, it is still the only model on the Matbench discovery that can predict at least magnetic moments with quite good accuracy $(0.032 \mu_B)$ [59]. One important caveat of this approach is the fact that it cannot predict the orientation of the magnetic moment, but only its size. This requires either previous knowledge or educated guess about the antiferromagnetic sublattices if one wants to employ this model on any other than ferromagnetic materials.

The database the model was trained on is from September 2022 [59]. It contains DFT calculations of 146 000 inorganic materials and 89 elements [59]. The calculations obtained

were done with GGA functionals with just GGA or GGA + U setup. There was attention to keep the same settings between calculations in a task, so that the energy difference of the final frame cannot be larger than 20 meV, and in the case of +U usage that the setting has to be the same as the primary task. No structures without energy and forces convergence steps were taken into training. Most importantly, structures that had energy higher than 1 eV/atom or lower than 10 meV/atom than in Materials Project ThermoDoc were not considered to eliminate differences that were caused by different settings for the calculations [59]. To minimize bias and keep data distribution, duplicate structures were removed as well [59]. Final number of considered structures was 1.5 million with 42 million of force data, 14 million of stresses and slightly below 8 million of magnetic moments.

The model can be obtained via pip and then used as any other python package. It relies on external packages as pymatgen [27] and ASE [66] to handle the input of user structures. Molecular dynamics simulation can be run either through ASE or LAMMPS but at the time of writing the LAMMPS interface was not working and the github page is no longer available. Model allows fine-tuning via pytorch but it requires to apply the same conditions that were mentioned in previous paragraph. The static prediction from the pretrained data will give the energy per atom of the given structure, which can be in VASP format, forces acting on each atom in eV/Å, the stress matrix and magnetic moment sizes on each atom. Getting forces in this format allows a construction of force constants and applying Phonopy afterwards without the need of any DFT calculation. The model also allows a structure optimization that will provide a prediction of relaxed crystal structure and atomic magnetic moments which can be used as a "pre-step" and input for before DFT calculations.

3.7.2 GRACE

A model that is in principle a continuation of ACE described in Section 3.7, the name is abbreviation of Graph Atomic Cluster Expansion. The difference arrives in the setup of graphs, where the original descriptors are tied to the node atom but here, they are not. This allows for a description of semi-local interactions [67]. The basis functions are constructed in similar way as in ACE but this time not localized on single atom only. Remaining steps are again very similar, the algebra is identical to ACE, but the cluster basis functions are again not centered on a single atom as the expansion coefficient is independent of atomic positions [67]. This allows the graph construction to be quite different now (see Figure 3.18). The nodes are then defined as trees and each of the node in a tree can be a root node. These can then be divided into subtrees that are attached into a root node and the distances are ordered to describe the paths to reach each node. For example, a subtree can branch at node 2 into 234 and 25 subtrees. The evaluated atomic properties - the energy - is now slightly more complicated than in ACE case (Equation (3.65) as it now has to describe not just the simple clusters but all the trees possible so the expansion gets quite long [67]:

$$E_{i} = E_{0} + \sum_{kv} c_{kv}^{(1)} A_{ikv}^{(1)} + \sum_{kv_{1}v_{2}} c_{kv_{1}v_{2}}^{(11)} A_{ikv_{1}v_{2}}^{(11)} + \sum_{kv_{1}v_{2}} c_{kv_{1}v_{2}}^{(12)} A_{kv_{1}v_{2}}^{(12)} \dots$$

$$(3.69)$$

This expansion continues with all the possible trees. This provides a complete property E as it is now dependent on multiple graph basis function [67]. This also means that local ACE is a subset of global ACE described here and that is by limiting it to only star descriptions [67]. Graph ACE provides a overcomplete set of cluster basis functions to describe the system which in turn leads to some self-interaction, but it can lead to some beneficial increase in accuracy [67]. There is one more simplification available by the fact that local ACE is a

subset of global ACE. Drautz called it Floret picking and Dandelion approximation and it involves evaluation of global ACE via layered evaluation of ACE. Basically taking the outermost stars into local ACE and then continuing further and further into the center via tensor decomposition and message passing [67].

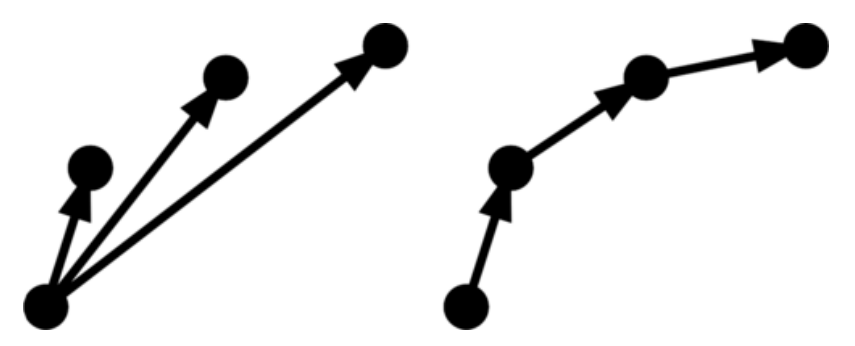


Figure 3.18: Example of the two cluster basis functions on the same nodes but with different topology allowed by GRACE [67].

At the time of writing, the GRACE UMLIPs offer three options of databases that were used in their training. First option are the ones trained on the OMat24 database [62, 67] with either two-layer semi-local graphs or one-layer local graphs. This database contains 101 million structures for 3.23 million of materials calculated by DFT via VASP code. The most accurate options are the "OAM" ones which are initially trained on the OMat24 database [62] but then were refitted on the MPTraj and Alexandria databases [59–61]. This models are again divided into two-layer and one-layer with two-layer version being the most accurate one. Alexandria database that the model was trained on contained at the time 10.4 million structures for 3.23 million materials. Even though they are the most accurate, they can be quite performance heavy as they are trained on an extreme amounts of data and thus using just the OMat24 models can be fine. Then there is also a just MPtraj model that is trained on the previously described database [59].

In contrast to the CHGnet model, GRACE does not allow any static predictions and is completely dependent on MD simulation codes (ASE, LAMMPS [52, 66]). Usage in LAMMPS requires a special compilation that is available on the Gracemaker github [67]. The model allows not only fine tuning, where again user has to be careful to be as close as possible to the settings of the databases, as well user trained models from scratch, i. e. users data. This allows to employ the GRACE approach on DFT calculations with different functionals than GGA although the number of calculation needed for a proper trained model can reach quite high values. The training also should not be done on just equilibrium structures but on a whole range of volumes, crystal lattice deformations and, at best, as well structures with defects so the computational cost can easily get quite high. It has to be noted that access to gpu is basically necessary as cpus do struggle heavily with fine-tuning or learning. From experience, 20 seconds for iteration on two 64 core cpus will turn into 50 iterations per second on one nVidia A100 gpu. This model also allows complicated models and simulations in LAMMPS, e. g. Monte Carlo MD run.

Interesting development of the method could be the extension to magnetism/charge. There were already attempts to train non-collinear magnetic vectors to ACE on Fe [68] alas they were not implemented into the main model yet.

4. CoCrNi alloy calculations

4.1 CoCrNi literature review

Previous publications show that this alloy has two possible phases with two different crystal structures - low temperature hcp and high temperature fcc. Previous DFT results show as the more stable the hcp crystal lattice at 0 K and experimental results at room temperatures observe fcc structure [69–71]. Results of previous calculations indicate that the fcc structure could be stabilised over the hcp by phonon interactions with rising temperature as well as at 0 K by tuning short-range order [72–75]. Oh et al. [75] has linked mechanical properties of high-entropy alloys to the electronegativities of the components. If the atoms have large electronegativity difference they have a tendency to short-range order which can lead to strengthening as the dislocation motion is hindered. These short-range orderings have even been observed experimentally even in CoCrNi alloy [76–81] by different methods. Zhang et al. [76] used energy filtered TEM to find short-range ordered domains through diffraction patterns. In the work [78] they have used x-ray, neutron total scattering and extended x-ray absorption fine structure techniques (EXAFS) to describe the tendencies of Cr to create short-range order as it wants to bond with Co and Ni more than with itself. Zhou et al. [77] used electron diffraction and atomic-resolution chemical mapping to determine the atomic columns. They have described a proposed lattice model out of their 3D atomic scans showing two sites, Co and Ni enriched and Cr enriched, showing the separation tendencies between Cr. Bacurau et al. [82] have done combined experimental and theoretical study. Theoretical part was done via machine learned potentials of moment tensor potential type specifically created from DFT to predict SRO. Experimental parts included DSC, TEM and mechanical testing. They have described a temperature of the Cr - Cr ordering somewhere between 800 - 900 K [82]. Tang et al. [79] have described a chemical variation around the intrinsic stacking-faults. These variations increased Cr concentration around stackingfaults while Ni and Co had lower concentrations, hinting at the fact that Cr ordering may influence the stacking-fault energy. Hsiao et al. [80] have observed diffraction patterns in their samples fitting an L₁₂ ordered structure. It was hinted that the cause for the orderings could be caused by magnetism and Cr - Cr bonds in the alloy [72–74]. Furthermore, Tan et al. [83] have measured the XANES spectra and the local electron structure flexibility describing Cr as quite a flexible element in this alloy.

4.2 Methods and models

4.2.1 Computational cells

To determine the effect of short-range ordering multiple 216 atom calculation cells were constructed (Figure 4.1). Each cell had equiatomic concentrations, i. e. 72 Co atoms, 72 Cr atoms and 72 Ni atoms. Three fcc structures were constructed by the **sqsgenerator** [49] and one ordered structure by hand. Ordered structure was created in such a way that the ordered element had always exactly two other atoms of the same element in its 1st nearest neighbour (NN) shell. These fcc cells were created in a way that the crystallographic direction [1 1 1] was parallel to the z axis, i. e. [0 0 1] direction. This allows to create hcp structures from the fcc structures by just moving the planes and thus keep as much of the short-range ordering parameters same between the fcc and hcp. The short-range ordering

parameters were calculated according to the Equation (2.1). The structures were created with the target maximizing the randomness in both 1st and 2nd NN shell.

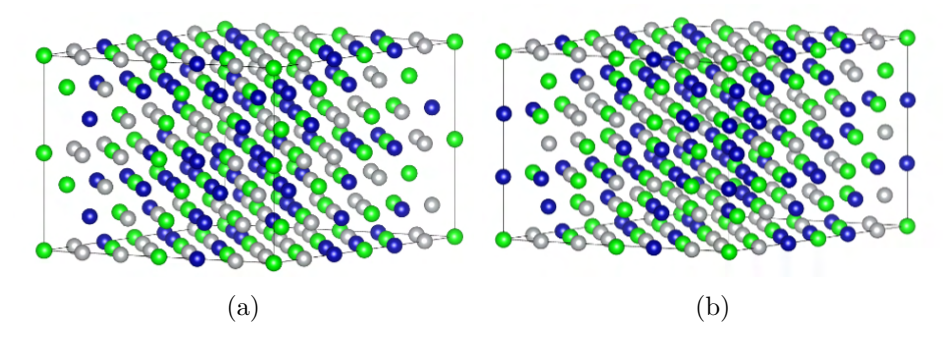


Figure 4.1: The 216 atom simulation cells - a) fcc b) hcp.

In total there were 12 calculation cells, randomly ordered cells were given the number 1, 2 and 3 for the fcc and hcp pair (fcc 1 and hcp 1 etc.) and the ordered cells were given their designation by the ordered element - Cr-o for Cr ordered and so on again with the pairs being fcc Cr-o and hcp Cr-o. The ordered sublattice was occupied by all the possible elements creating another 3 structures, Co ordered, Cr ordered and Ni ordered. The other sublattice (Randomly ordered element in Figure 4.2) was randomly occupied by the other two remaining elements (e. g. by Cr and Ni for Co ordered and so on), this was done by using the sqsgenerator only on these specific positions.

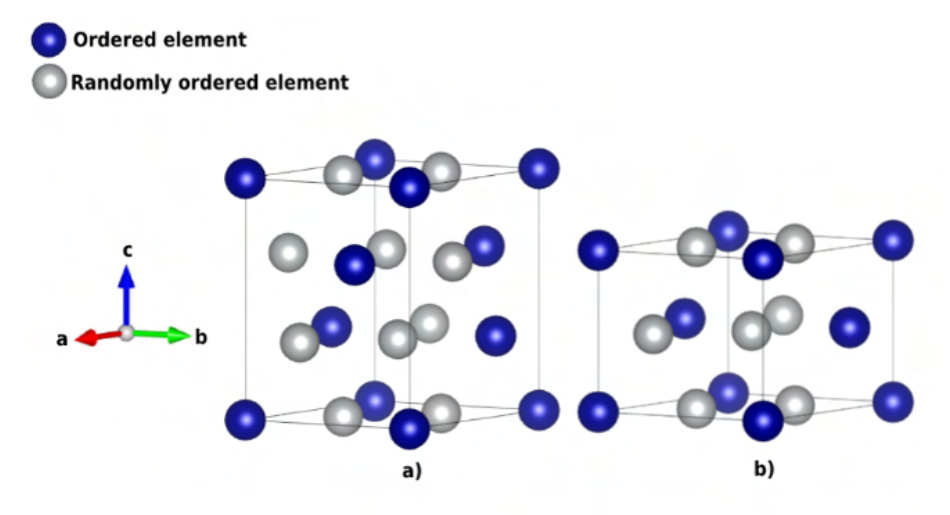


Figure 4.2: Primitive cells for the a) fcc ordered structure and b) hcp ordered structure.

Structure with the biggest interest was the Cr ordered one as it should be prefferable for Cr magnetic ordering. As an antiferromagnetic element, Cr wants to be antiferromagnetically ordered but in the randomly ordered structures it is hardly possible with many Cr - Cr bonds. In the Cr ordered structure there were always just two Cr atoms in another ones 1st NN shell and thus allowing to reach antiferromagnetic ordering. In the ordered structures, there was no optimization of 2nd NN shells and all the values received are very close to zero except structure hcp 3 where Cr - Cr and Co - Co had slightly higher W-C parameters. The resulting W-C parameters for the first two NN shells can be found in

Table 4.1 and Table 4.2. For the structures 1 and 3 created by sqsgenerator, the resulting W-C parameters are very close to zero indicating a random short-range ordering. The structure 2 had slightly higher values of Co - Ni and Ni - Ni W-C parameters indicating less bonds of Co - Ni and more abundant Ni - Ni bonds which hints at small form of Ni clustering. For the ordered structures the Warren Cowley (W-C) parameters between the ordered elements was always 0.50 and -0.25 for the ordered element - other element in both fcc and hcp cells. For the unordered - unordered element W-C parameters, there was a small difference between fcc and hcp as the parameters were 0.16 and 0.10 respectively.

| | | | | | α_i | j in 1st | NN sh | ell | | | | |
|-----------|-------|-------|-------|-------|------------|----------|-------|-------|---------------------|-------|-------|-------|
| Structure | Co - | - Co | Co · | - Cr | Co | - Ni | Cr · | - Cr | Cr | - Ni | Ni - | - Ni |
| | fcc | hcp | fcc | hcp | fcc | hcp | fcc | hcp | fcc | hcp | fcc | hcp |
| 1 | 0.05 | 0.04 | -0.02 | -0.04 | -0.02 | 0.00 | -0.01 | 0.01 | 0.04 | 0.03 | -0.01 | -0.03 |
| 2 | -0.02 | -0.06 | -0.08 | -0.09 | 0.10 | 0.15 | 0.01 | 0.01 | 0.08 | 0.08 | -0.18 | -0.23 |
| 3 | 0.05 | 0.01 | -0.05 | 0.01 | 0.00 | -0.02 | 0.04 | -0.02 | 0.00 | 0.01 | 0.00 | 0.01 |
| Cr-o | 0.16 | 0.10 | -0.25 | -0.25 | 0.09 | 0.15 | 0.50 | 0.50 | -0.25 | -0.25 | 0.16 | 0.10 |
| Со-о | 0.50 | 0.50 | -0.25 | -0.25 | -0.25 | -0.25 | 0.16 | 0.10 | 0.09 | 0.15 | 0.16 | 0.10 |
| Ni-o | 0.16 | 0.15 | 0.09 | 0.10 | -0.25 | -0.25 | 0.16 | 0.10 | -0.25 | -0.25 | 0.50 | 0.50 |

Table 4.1: Warren-Cowley parameters of 1st NN shell.

| | α_{ij} in 2nd NN shell | | | | | | | | | | | | |
|-----------|-------------------------------|-------|-------|-------|-------|-------|-------|-------|-------|-------|-------|------|--|
| Structure | Co · | - Co | Co | - Cr | Co | - Ni | Cr - | - Cr | Cr · | - Ni | Ni - | Ni | |
| | fcc | hcp | fcc | hcp | fcc | hcp | fcc | hcp | fcc | hcp | fcc | hcp | |
| 1 | -0.01 | 0.06 | -0.01 | 0.02 | 0.00 | -0.08 | 0.08 | 0.10 | -0.10 | -0.12 | 0.10 | 0.19 | |
| 2 | 0.01 | -0.01 | 0.03 | 0.02 | -0.05 | -0.01 | -0.08 | -0.01 | 0.05 | -0.01 | 0.00 | 0.00 | |
| 3 | 0.03 | 0.14 | -0.06 | -0.13 | 0.03 | -0.01 | 0.07 | 0.18 | -0.01 | -0.05 | -0.01 | 0.06 | |
| Cr-o | 0.04 | 0.04 | 0.00 | 0.00 | -0.04 | -0.04 | 0.00 | 0.00 | 0.00 | 0.00 | 0.04 | 0.04 | |
| Со-о | 0.00 | 0.00 | 0.00 | 0.00 | 0.00 | 0.00 | 0.04 | 0.04 | -0.04 | -0.04 | 0.04 | 0.04 | |
| Ni-o | 0.04 | 0.04 | -0.04 | -0.04 | 0.00 | 0.00 | 0.04 | 0.04 | 0.00 | 0.00 | 0.00 | 0.00 | |

Table 4.2: Warren-Cowley parameters of 2nd NN shell.

4.2.2 Calculation settings

For the calculations, the projector augmented waves potentials (PAW) [84] were used with a generalized gradient approximation (GGA) of exchange and correlation energy as described by Perdew, Burke and Ernzerhof (PBE) [85]. The k-space was integrated over by Methfessel-Paxton smearing method with a width of 0.1 eV [86]. The Brillouin zone was set to a Monkhhorst-Pack mesh in a size of 4x4x4. Plane wave cutoff energy was set to 450 eV. The calculations were done in both non-spin-polarised states and in spin-polarised state. For the spin-polarised the initial magnetic moments were set as follows, for Co 1 μ_B , for Cr 1 and -1 μ_B distributed to get as high antiferromagnetic ordering as was possible for the structure and for Ni 0.5 μ_B . Relaxations were carried out with the external tool Gadget [87] that utilizes internal coordinates to preserve fcc and hcp parameters of the cells and improving performance as described in Section 4.2.4.

The pure elements were calculated in their ground states with relaxations done by the internal VASP optimizer and not with Gadget. Ferromagnetic Co was calculated in hcp

lattice with parameters of a = 2.507 Å and c = 4.069 Å, antiferromagnetic Cr in bcc lattice with a = 2.883 Å and Ni in diamond structure $Fd\bar{3}m$ with a = 2.515 Å.

4.2.3 Bader method for charge analysis

Local charges and magnetic moments on ions were determined by employing the method developed by R. Bader [88] which gives more accurate results compared to the VASP outputs. This method partitions the electrons to specific ions on basis of gradient of charge density at a particular point to the maximum that is usually at the center of an ion, the division of these spaces is placed at the zero of the gradient [89]. These spaces are called either Bader volumes or Bader spaces. Furthermore, integrating over these Bader volumes gives atomic charges and kinetic energies. These Bader volumes all contain a single electron density maximum and are separated from each other by a zero flux surface of the gradients of the electron density $\nabla \rho(\bar{r}) \cdot \hat{n} = 0$ where the electron density is $\rho(\bar{r})$ and \hat{n} is the unit vector perpendicular to the dividing surface at any surface point. Each volume is then defined by a set of points that for the trajectory of maximizing electron density reach the same unique fixed point maximum. This gives much more precise approximation to which electrons belong to which ion in comparison to VASP, where PAW potential calculations define the occupancies into a PAW spheres which can also overlap, thus giving some errors for the values [84, 85, 90]. VASP also employes the frozen core approximation, which is not an inherent feature of PAW potentials, this makes all the electrons in the core kept frozen in the configuration for which the PAW dataset was generated. This means that only the valence charge density is written out into the CHGCAR output file and because Bader requires the charge density maximum it needs the core electrons output as well. Thus requiring another run after relaxation with the LAECHG setting in the INCAR file and also quite fine fast-Fourier transformation grid to accurately represent these core charges.

The used method to get Bader charges was implemented by Henkelman et al. and Yu et al. [89, 91] and it uses the steepest ascent trajectories over a fine enough grid that are confined to the grid points to identify Bader regions. The total electronic charge within a Bader region is then approximated by summing over the grid points belonging to the specific Bader region. Bader regions without a nucleus are not a problem in this method as it does not use nucleus coordinates. The algorithm limits the paths as it can go from one grid point only to one of the neighbouring other points to improve performance. The step from a grid point (i, j, k) is made along the direction that will maximize the charge density gradient $\nabla \rho$ which is calculated for all the possible neighbouring directions \hat{r} using the formula:

$$\nabla \rho(i,j,k) \cdot \hat{r}(di,dj,dk) = \frac{\Delta \rho}{|\Delta \overrightarrow{r}|}, \tag{4.1}$$

where di, dj, dk are each assigned values -1, 0, 1 but excluding di = dj = dk = 0. The changes in density and in the distance are then calculated and evaluated between neighbours as:

$$\Delta \rho = \rho(i+di, j+dj, k+dk) - \rho(i, j, k), \tag{4.2}$$

$$\left| \Delta \overrightarrow{r} \right| = \left| \overrightarrow{r} (i + di, j + dj, k + dk) - \overrightarrow{r} (i + j + k) \right|, \tag{4.3}$$

where $\overrightarrow{r}(i,j,k)$ is the Cartesian vector to the grid point (i,j,k). The steepest ascent step selected is the one that maximises the positive values of $\nabla \rho(i,j,k)$, in case of no positive values, the point is considered to be the charge density maximum.

The function of the algorithm is illustrated in Figure 4.3, starting point (i_1, j_1, k_1) (Figure 4.3 A) from which the steepest ascent path is followed until a charge density maximum

 m_1 is reached. The number 1 assigned to the maximum describes the Bader volume 1 and all the points along the path are then assigned to the Bader volume 1, as well as all the paths from each of these points that terminate at this point. Then another point (i_2, j_2, k_2) is selected from the grid that has not been used for the paths to get the m_1 point and the steepest path search begins anew. Now the only difference is that the path is extended until it reaches either maximum or a point that has already been assigned, i. e. a border with another volume. In the example in Figure 4.3 B the second path is terminated after just 2 ascent steps as it reaches a point already assigned to a Bader region 1. Each point is then assigned again to the Bader region 1 with the maximum m_1 as that would be the maximum for the origin point as well. Then this is done again for all the remaining points (i_n, j_n, k_n) (Figure 4.3 C) until it reaches a new maximum m_2 , new charge density maximum is added and all the points along the path are assigned to it. This is repeated until all the grid points are analyzed over (Figure 4.3 D).

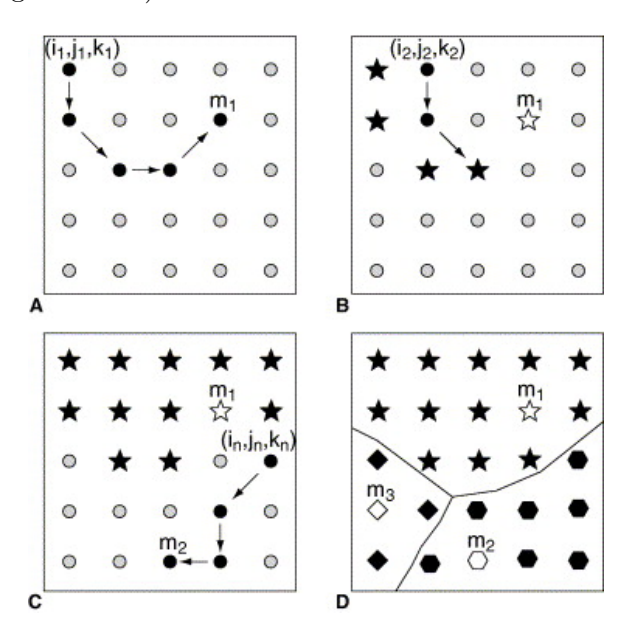


Figure 4.3: Illustration of the steepest ascent paths on the charge density grid [91].

The disadvantage of the original Henkelman method is its lattice bias as it is constrained to these grid points. Yu et al. [89] improved the method by introducing a weight to the grid points representing how much they belong to which Bader volume. The local maxima now has a basin of attraction A_n that describes how many of the points flow to the maxima along the charge density gradient. This means that for any point \overrightarrow{r} trajectory is given as $\overrightarrow{x}(t) = \nabla \rho(\overrightarrow{x})$ which then can be integrated over with the initial condition $\overrightarrow{x}(0) = \overrightarrow{r}$ to find $\lim_{x\to\infty} \overrightarrow{x}(t)$. The basin of attraction A_n are then all the points whose trajectory $\lim_{x\to\infty} \overrightarrow{x}(t)$ ends at \overrightarrow{x}_n .

The weight method then uses the Voronoi polyhedra (Figure 4.4) created by the grid points X with volume V_X into which a point in Cartesian space \overrightarrow{r} belongs to, if X is the closest point. Each polyhedra is defined by

- the nearest neighbouring points X' with distance $l_{X\to X'}$,
- facets at the midpoint between X and X' $\delta V_{X \to X'}$ that have a normal $\hat{n}_{X \to X'}$ pointing from X to X',

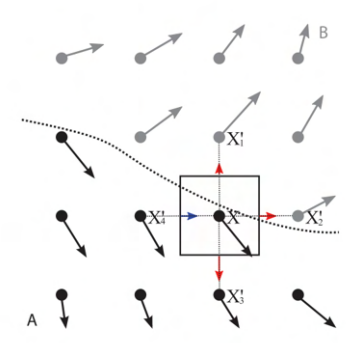


Figure 4.4: Schematic of the weight method with Voronoi polyhedra [89].

• an area $a_{X\to X'}$.

With this the weight $w^A(X)$ can be defined between 0 and 1 in a way that $\sum_A w^A(X) = 1$ for all X and then the discrete approximation to the integral over the basin A will converge quadratically in the grid for smooth functions $f(\overrightarrow{r})$:

$$\int_{A} d^{3}r f(\overrightarrow{r}) \approx \sum_{X} V_{X} w^{A}(X) f(X). \tag{4.4}$$

The transition to Voronoi partitioned definition requires continuum probability density for the trajectories $P(\overrightarrow{r},t)$ and the probability flux at any point an time

$$\overrightarrow{j}(\overrightarrow{r},t) = P(\overrightarrow{r},t)\nabla\rho(\overrightarrow{r}). \tag{4.5}$$

With these two defined and combined, the probability distribution evolution in time can be gained from a continuity equation

$$\frac{\delta P(\overrightarrow{r},t)}{\delta t} + \nabla \cdot (P(\overrightarrow{r},t)\nabla \rho(\overrightarrow{r})). \tag{4.6}$$

With this equation it is possible to determine how the points in V_X distribute to the neighbouring volumes V_X' . Solution of this equation gives the time-integrated flux of probability from V_X to V_X' through the facet $\delta V_{X\to X'}$ as

$$J_{X \to X'} = \int_0^\infty dt \int_{\delta V_{X \to X'}} P(\overrightarrow{r}, t) \nabla \rho \cdot \hat{n}_{X \to X'} d^2 r = \dots$$

$$\dots = \frac{a_{X \to X'} l_{X \to X'}^- 1 R(\rho_X' - \rho_X)}{\sum_{X}' a_{X \to X'} l_{X \to X'}^- 1 R(\rho_X' - \rho_X)},$$

$$(4.7)$$

where R is the ramp function. From this we can get the weight representing the volume fraction of points in volume V_X whose trajectory also end in the basin A

$$w^{A}(X) = \sum_{X}' J_{X \to X'} w^{A}(X'). \tag{4.8}$$

From this equation we get that each point X is one of three possibilities:

1. A local maxima - density ρ at X is higher than at X' for all possible neighbours, thus the point corresponds to a new basin A with a weight $w^A(X) = 1$.

- 2. An interior point density ρ at X is lower than at X' for all possible neighbours X', the weights have been assigned and $w^A(X') = 1$ for the same basin $A \to \text{point } A$ belongs to basin A as well.
- 3. A boundary point weights of point between 0 and 1 for multiple basins A.

This way the algorithm improves the Henkelman method with lesser amount of error cause by finite grid (Figure 4.5) and computational scaling as well.

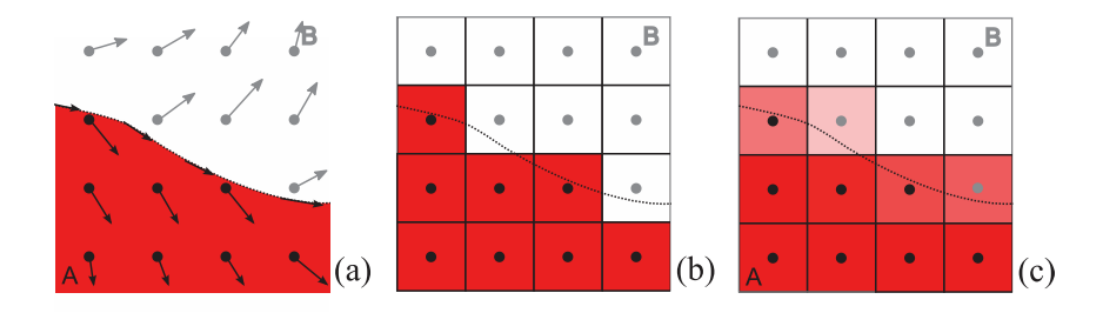


Figure 4.5: Schematic illustration of the a) zero flux surface as originally proposed by Bader, b) near grid algorithm used by Henkelman, c) weighted integration [89].

4.2.4 Optimization using internal coordinates - Gadget tool

Internal coordinates, for example bond lengths, bond angles etc. provide some advantages for structure optimization over the generally used Cartesian or fractional coordinates. A good initial guess of Hessian matrix is quite easily achievable, coupling of different modes is reduced compared to Cartesian coordinates and the handling of constraints is much simpler [87].

The structure of a periodic system is characterized by three lattice vectors in matrix \mathbf{h} and by 3N fractional coordinates \mathbf{s} . The position of atom a in the $\mathbf{L} = (l_1, l_2, l_3)$ unit cell of the solid in Cartesian coordinates is then given by linear transformation [87]:

$$r_{\alpha}^{a,\mathbf{L}_{a}} = \sum_{\beta=1}^{3} h_{\alpha\beta}(s_{\beta}^{\alpha} + l_{\beta}^{\alpha}). \tag{4.9}$$

The deformations of the structure in periodic system can arise from the change of atomic positions at the constant lattice vectors and from the deformation of lattice vectors and constant fractional coordinates. The fractional coordinates can be obtained from Cartesian by doing the inverse transformation. Variation of lattice vectors can be described by strain tensor [87]: $\epsilon_{\alpha\gamma}$

$$h'_{\alpha\beta} = \sum_{\gamma} (\delta_{\alpha\gamma} + \epsilon_{\alpha\gamma}) h_{\gamma\beta}. \tag{4.10}$$

Any change that happens to lattice vectors $h_{\alpha\beta}$ is inherently tied to a variation of the atomic Cartesian coordinates as described in Equation (4.9) thus we can describe their variation similarly by using the stress tensor again [87]

$$r_{\alpha}' = \sum_{\beta} (\delta_{\alpha\beta} + \epsilon_{\alpha\beta}) r_{\beta}. \tag{4.11}$$

The energy of the structure is invariant to six degrees of freedom out of the total 3N + 9 deformation variables - the position of the origin and the orientation of the lattice vectors. Origin position of the lattice is completely arbitrary but it is generally chosen at the basis of symmetry [87]. Rotations of the lattice can be avoided by taking the symmetric part of strain tensor as independent lattice variables. The simplest coordinate system for a periodic system will consist of 3N fractional atomic positions and nine lattice vector variations which will give this expansion [87]:

$$E(\mathbf{x} + \delta \mathbf{x}) - E(\mathbf{x}) = -\mathbf{f}^{\mathbf{t}} \delta \mathbf{x} + \frac{1}{2} \delta \mathbf{x}^{\mathbf{t}} \mathbf{F} \delta \mathbf{x} + \dots$$
 (4.12)

The vector \mathbf{f} consists of either forces or lattice vector derivatives of total energy related to the stress tensor elements depending on the relaxation scheme. There is also a contribution by the atomic forces to this stress tensor. The extended Hessian matrix \mathbf{F} built in (Equation (4.12)) contains several blocks with second derivatives of energy with respect to atomic positions, stress-strain derivatives as well as cross terms [87].

Defining internal coordinates that contain only integral degrees of freedom is done by transformation of fractional coordinates. These are generally just nonlinear functions of Cartesian coordinates. Similarly to external coordinates, internal coordinates are also determined by the three lattice vectors $\hat{q}_i = f(\{h_{\alpha\beta}\})$. The deformations in internal coordinates are related to the external by a nonlinear transformation usually approximated by Taylor expansion. By applying it to the energy expansion Equation (4.12), a relationship between external and internal force/stress components is obtained [87]:

$$\mathbf{B}^{\mathbf{t}}\varphi = \mathbf{f},\tag{4.13}$$

and between external deformations and internal distortions:

$$B\delta \mathbf{x} = \delta \xi, \tag{4.14}$$

where \boldsymbol{B} is a generalization of Wilsons's B matrix [92] for periodic systems. To avoid problems with high amount of generated integral coordinates a linear combination of primitive internal coordinates is used [93] by taking singular value decomposition of the B matrix as $\boldsymbol{B} = \mathbf{U}^{t}\mathbf{B}_{D}\mathbf{V}$, where \boldsymbol{U} and \boldsymbol{V} are unitary matrices and \boldsymbol{B}_{D} is a diagonal matrix formed from eigenvectors from nonzero eigenvalues of [87, 92]($\mathbf{B}\mathbf{B}^{t}$). Multiplicating the B matrix equation by \mathbf{U} gives the defining relationship for the delocalized internal coordinate transformation for molecules [87]:

$$\widetilde{\mathbf{B}}\mathbf{x} = \widetilde{\mathbf{q}}.\tag{4.15}$$

In the case of periodic systems the atoms are explicitly dependent on lattice vectors leading to augmented B matrix equation [87]:

$$\begin{pmatrix} \delta \mathbf{q} \\ \delta \hat{\mathbf{q}} \end{pmatrix} = \begin{pmatrix} \mathbf{B}^{qs} \mathbf{B}^{qh} \\ \mathbf{B}^{\hat{q}s} \mathbf{B}^{\hat{q}h} \end{pmatrix} \begin{pmatrix} \delta \mathbf{s} \\ \delta \mathbf{h} \end{pmatrix}, \tag{4.16}$$

where the individual blocks \mathbf{B}^{qs} , $\mathbf{B}^{\hat{q}s}$ describe the linear transformation of the atomic positions s^a_{α} while the blocks \mathbf{B}^{qh} , $\mathbf{B}^{\hat{q}h}$ describe the transformations of lattice vector components $h_{\alpha\beta}$ to atomic and lattice internal coordinates. In periodic system, an internal coordinate may depend on the Cartesian coordinates of an atom in a different unit cell, thus the \mathbf{B} matrix between fractional atomic distortions and unique internal coordinates has to be calculated as [87]:

$$B_{i,a_{\alpha}}^{qs} = \sum_{\mathbf{L}} \sum_{\beta} \frac{\partial q_i}{\partial r_{\beta}^{a,\mathbf{L}_a}} h_{\beta\alpha}.$$
 (4.17)

For the coordinates that remain in the unit cell, the \boldsymbol{B} matrix elements are the same as for non-periodic system. For several periodic copies of the same atom participating in a given internal coordinate the contributions are summed up. Proportionality between internal coordinate deformation [87] δq_i and a lattice vector distortion $\delta h_{\alpha\beta}$ can be described by these \boldsymbol{B} matrix elements [87, 92]

$$B_{i,\alpha\beta}^{qh} = \frac{\partial q_i(r_{\alpha}^{a, \mathbf{L}_a}, r_{\beta}^{b, \mathbf{L}_b}, \dots)}{\partial h_{\alpha\beta}} = \dots = \sum_{a, \mathbf{L}_a} \frac{\partial q_i}{\partial r_{\alpha}^{a, \mathbf{L}_a}} (s_{\beta}^a + l_{\beta}^a)$$
(4.18)

Cell edge lengths, volume, cell angles and other lattice internal coordinates \hat{q} have no explicit dependencies on the fractional atomic positions thus the block of the extended \boldsymbol{B} matrix is zero [87] $\boldsymbol{B}^{\hat{q}s} = 0$ [87].

Geometry constraints are achieved by modifying the \boldsymbol{B} matrix in a way that the first derivatives of the relaxed coordinates are orthogonalized with respect to each of the constrained coordinate q_c . The rows of the \boldsymbol{B} matrix \boldsymbol{B}_j are thus modified accordingly to the constrained coordinates \boldsymbol{B}_c [87]:

$$\bar{\boldsymbol{B}}_{j} = \boldsymbol{B}_{J} - \sum_{c} \frac{(\boldsymbol{B}_{j} \cdot \boldsymbol{B}_{c})}{|\boldsymbol{B}_{c}|} \frac{\boldsymbol{B}_{c}}{|\boldsymbol{B}_{c}|}.$$
(4.19)

The delocalized internal coordinates are generated from this modified matrix and are now linear combinations of either constrained or relaxed coordinates but never combination of constrained and relaxed coordinate [87]. With this, the optimization is able to proceed as if it was not constrained for the relaxed parameters. By this method, the available constraints are ratios and sums of primitive internal coordinates, norms of vectors that have components in primitive internal coordinates, lattice parameters, volume of the cell and others [87].

The relaxation algorithm employed by Gadget [87] is based on the geometrical direct inversion in the iterative subspace (DIIS) method [94]. This method uses the previously collected information from previous M relaxation steps on the potential energy surface (PES) to minimize the norm of the error vector. The vector is defined as a linear combination of gradients correspoding to delocalized internal coordinates:

$$\mathbf{r}_k = \sum_{i=k-M}^k c_i \widetilde{\varphi}_i. \tag{4.20}$$

The coefficients c_i are obtained by minimizing the lattice vector matrix under the constraint [87, 94] $\sum_{i=k-M}^{k} c_i = 1$. A new set of internal coordinates is then calculated [87, 94]:

$$\widetilde{\mathbf{q}}_{k+1} = \sum_{i=k-M}^{M} c_i \widetilde{\mathbf{q}}_i + \widetilde{\mathbf{H}}^{-1} \sum_{i=k-M}^{M} c_i \widetilde{\varphi}_i. \tag{4.21}$$

The parameter M depends heavily on the location of the structure on the PES. If the structure is close to the minimum, M should be 10 or higher. When the initial guess is poor and the landscape of the PES is not well described, then better performance is achieved by using low number of previous steps. The relaxation in itself works by comparing the ionic step produced by the DIIS method to a simple quasi-Newton step [87, 94] $\Delta \tilde{\mathbf{q}}^{QN} = \tilde{\mathbf{H}}^{-1} \tilde{\varphi}$ and the ionic step needs to meet these criteria [87, 94].

- 1. The direction of the DIIS step $\Delta \tilde{\mathbf{q}}$ deviates from the quasi-Newton step by an angle ϕ and its $\cos \phi$ is larger than 0.97, 0.84, 0.71, 0.67, 0.56, 0.49, 0.41 for two of the nine recent relaxation steps done by DIIS. For 10 or more relaxation steps this criterion is ignored:
- 2. The norm of DIIS step can only be ten times larger than the reference step.
- 3. Sum of all positive coefficients c_i can not exceed the value of 15.
- 4. The magnitude of $\frac{\mathbf{c}}{|\mathbf{r}^2|} < 10^8$.

If any of these criteria is not fulfilled the step is not accepted. The most remote vector is then removed from the iterative subspace and the whole procedure is repeated until all the criteria are fulfilled.

The main performance advantage of internal coordinates is the guess of Hessian matrix. Gadget uses a model Hessian guess constructed from force constants which are simple functions of nuclear positions from [95]:

$$k_{ij} = k_r \rho_{ij}, \tag{4.22}$$

$$k_{ijk} = k_{\phi} \rho_{ijk} \rho j k m, \tag{4.23}$$

$$k_{ijkl} = k_{\pi} \rho_{ij} \rho j k \rho_{kl}, \tag{4.24}$$

$$\rho_{ij} = \exp\left[\alpha_{ij}(r_{0,ij}^2 - r_{ij}^2)\right]. \tag{4.25}$$

These equations need 15 independent parameters for elements from the first three rows of the periodic table. From this the model Hessian is transformed into delocalized internal coordinates by the formula [87]

$$\widetilde{\mathbf{H}} = \mathbf{U}^{\mathbf{t}} \mathbf{H} \mathbf{U}. \tag{4.26}$$

As the relaxation begins the initial guess of the Hessian matrix is replaced by employing the Broyden-Fletcher-Goldfarb-Shanno algorithm to [87]

$$\widetilde{\mathbf{H}}_{k} = \widetilde{\mathbf{H}}_{k-1} \left(\frac{\Delta \widetilde{\varphi}_{k} \Delta \widetilde{\varphi}_{k}^{t}}{\Delta \widetilde{\varphi}_{k-1}^{t} \Delta \widetilde{\mathbf{q}}_{k}} + \frac{\widetilde{\mathbf{H}}_{k-1} \Delta \widetilde{\mathbf{q}}_{k-1} \Delta \widetilde{\mathbf{q}}_{k-1}^{t} \widetilde{\mathbf{H}}_{k-1}}{\Delta \widetilde{\mathbf{q}}_{k-1}^{t} \widetilde{\mathbf{H}}_{k-1} \Delta \widetilde{\mathbf{q}}_{k-1}} \right), \tag{4.27}$$

where $\Delta \widetilde{\varphi}_k = \widetilde{\varphi}_k - \widetilde{\varphi}_{k-1}$ is the change of gradients tied to the relaxation step [87] $\Delta \widetilde{\mathbf{q}}_k = \widetilde{\mathbf{q}}_k - \widetilde{\mathbf{q}}_{k-1}$. For the selected examples the Gadget with this relaxation method outperforms the optimizer included in VASP by a factor of 2 - 10 [87].

The Gadget tool, as used for VASP, is an external tool written in Python. It reads the geometry, energy and gradients from the VASP output and sets up internal coordinates. From these it estimates optimal moves for atoms and calculates new set of lattice parameters and their respective Cartesian coordinates. After this, it starts a new VASP calculation and repeats until convergency is reached. In calculations the Gadget was used to put constraints on all the angles in the unit cells to keep them constant. Then specifically, for the hcp structure to keep the c/a ratio and the fcc structure all lattice parameters stay within the given ratios.

4.2.5 Application of UMLIPs

The application of UMLIPs for CoCrNi is a static prediction via the CHGNet [59] model to obtain energetics, forces and magnetic moments and compare them to the already done DFT calculations. Afterwards, if the prediction describes the DFT results well, a combination of CHGNet and Phonopy could be used to obtain harmonic approximations for otherwise computationally very costly calculations - approximately 1290 displacements for a classical Phonopy displacement workflow. This workflow would then contain only CHGNet predictions into Phonopy Force Sets. The idea is the same as the normal Phonopy workflow except instead of DFT calculations the CHGNet static prediction is run on the displaced structures. To do this one only needs the relaxed structures from DFT, *i. e.* the CONTCAR file.

The second application is the GRACE [67] UMLIP combined with MD simulations to study the temperature evolution of the fcc and hcp stability. The MD simulations were run via LAMMPS within the NPT ensemble with Nose-Hoover thermostat and barostat [52]. The time step was set to 0.001 ps and the heating was done within 20000 steps resulting in 20ps long simulation. The GRACE universal model used was the OMAT-2L to properly represent the semi-locality present in HEAs [67]. The crystal lattice is checked in Ovito by its common neighbour analysis [53] on the exported trajectories of atoms from the MD runs. Additionally, the radial distribution function RDF was computed from the resulting trajectories. Since multiple temperatures were explored, the thermal expansion was obtained. To evaluate the fcc - hcp relative stability enthalpies were calculated within the temperature runs and the value of enthalpy was taken as time averaged. This enthalpy contains the simulation box volume, pressure and total energy [52]:

$$H = E_{tot}^{MD} + pV. (4.28)$$

To check for annihilation of chemical SRO, a script was written to check if any of the atomic switched positions.

4.3 Results

4.3.1 Phase stability

The phase stability of the calculated structures was evaluated by calculating their mixing enthalpy H_{mix} from the pure elements according to Equation (3.52). The results can be found in Table 4.3 and in Figure 4.6. The spin-polarised calculations always result in lower mixing enthalpy than the non-spin-polarised calculations which was an expected result as the alloy has a Curie temperature of 4 K [11, 96] and was also in agreement with previously published calculations [71, 73, 74, 97]. Also, according to the previous DFT calculations, the hcp structures proved to be more stable than fcc except for the case of Ni ordered cells that will be described later. The fcc structure was less influenced by the small differences in orderings between the different randomly ordered cells and did not react to Co nor Ni ordering as their mixing enthalpies were in line with the randomly ordered cells. The biggest change in H_{mix} was for the Cr ordered where the value lowered by 3.55 kJ/mol in comparison to the average of all the other spin-polarised fcc structures. In some previous publications [73, 74] similar trends for Cr ordering were also perceived.

Short-range ordering had much higher influence on the hcp structures. The variance between the resulting values (without the Cr ordered cells as they were a specific outlier)

| Structure | H_{mix} in kJ/mol | | | | | | | | | |
|-----------|---------------------|------------|----------------------|--------------------|------|----------------------|--|--|--|--|
| Structure | , | Spin-polar | rised | Non-spin-polarised | | | | | | |
| | fcc | hcp | $\Delta H_{hcp-fcc}$ | fcc | hcp | $\Delta H_{hcp-fcc}$ | | | | |
| 1 | 8.75 | 8.05 | -0.70 | 9.64 | 8.99 | -0.65 | | | | |
| 2 | 8.50 | 7.50 | -1.00 | 9.13 | 8.11 | -1.02 | | | | |
| 3 | 8.56 | 8.00 | -0.56 | 9.10 | 8.95 | -0.15 | | | | |
| Cr-o | 5.02 | 4.46 | -0.56 | 5.19 | 4.47 | -0.72 | | | | |
| Со-о | 8.65 | 7.82 | -0.83 | 9.06 | 8.44 | -0.62 | | | | |
| Ni-o | 8.41 | 8.78 | 0.37 | 9.08 | 9.75 | 0.67 | | | | |

Table 4.3: Mixing enthalpy of calculated structures.

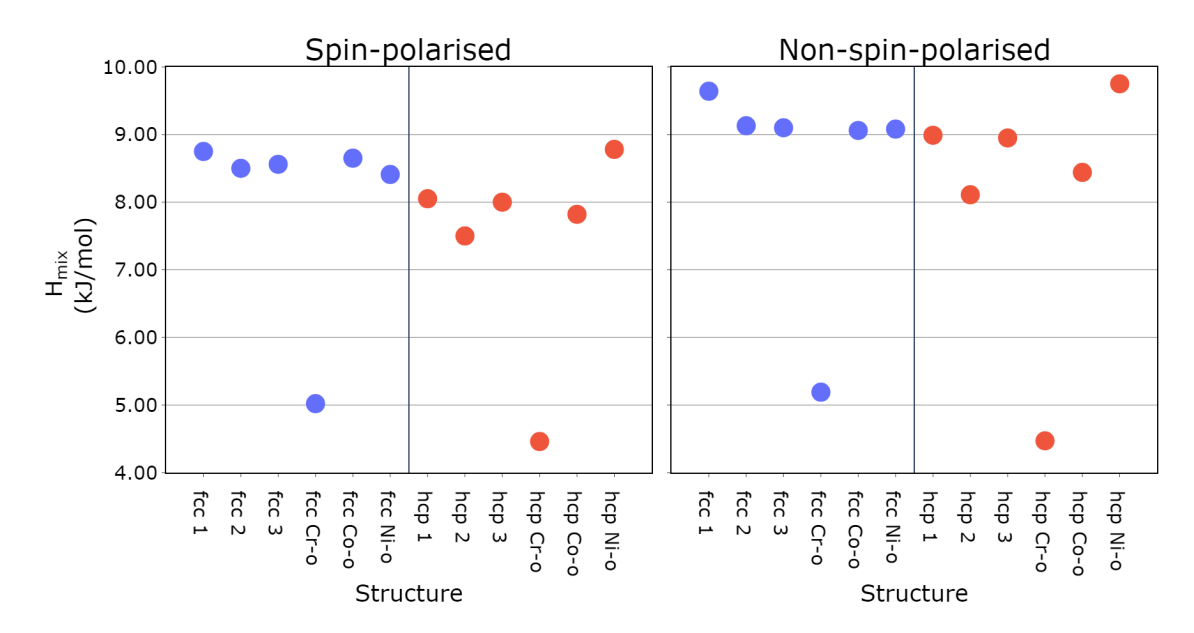


Figure 4.6: Mixing enthalpies of the CoCrNi calculated structures.

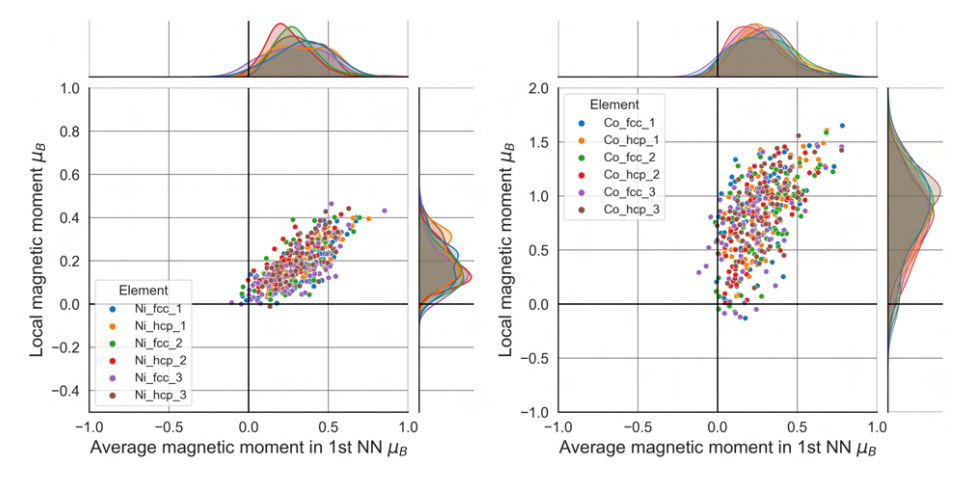
of H_{mix} was about 0.178 kJ/mol compared to the 0.014 kJ/mol for fcc. The Cr ordering caused a similar drop of H_{mix} as in fcc with size of 3.57 kJ/mol and still resulting in hcp being the more favourable structure. However, the $\Delta H_{hcp-fcc} = -0.56 \text{ kJ/mol}$ for this case was one of the two lowest of all received for spin-polarised calculations. This ordering was experimentally observed by Inoue et al. via atom probe tomography [98] as well as a very similar model proposed by Hsiao et al. [80]. The highest stability disregarding the Cr-o structure was received for the hcp 2 structure as there was a slight deviation of some W-C short range order parameters from complete randomness, specifically for Ni. The hexagonal structure dependence on Ni becomes even more clear with the Ni-o result. In this case, the hcp ends up being so destabilised by the Ni ordering that it becomes the less favourable structure compared to the fcc structure with $\Delta H_{hcp-fcc} = 0.37$ kJ/mol. Looking at the SRO values in Table 4.1 the Ni ordered structure has less Ni bonds while the structure 2 has a negative value of W-C parameter indicating some form of clustering. This means that clustering of Ni stabilises the hcp structure for CoCrNi alloy while minimizing the bonds between Ni atoms destabilises hop structure quite significantly. The Co ordering did not seem to cause any specific effects and both fcc and hcp structures seem indifferent to it.

By not including the spin-polarization the values of mixing enthalpy increased for all cells with hcp again being more influenced structure with average difference of 0.68 compared to 0.55 for fcc. The trends were the same for the non-spin-polarised calculations with only one exception in cells with number 3. Compared to the spin-polarised calculation, the difference between hcp and fcc is only $\Delta H_{hcp-fcc} = -0.15 \text{ kJ/mol}$ compared to $\Delta H_{hcp-fcc} =$ -0.56 kJ/mol in spin-polarised. This higher difference could be caused by the differences between the SRO parameters for hcp and fcc as well as some higher SRO in the 2nd NN shells, especially for Cr - Cr and Co - Co. As the hcp 3 follows the same trends of other hcp structures with their increase of H_{mix} the culprit is probably fcc 3 with the lowest increase of H_{mix} between spin-polarised and non-spin-polarised. This hints at some magnetic interaction reducing the stabilisation by introducing the spin-polarization. Other two notable differences were for the Ni-o and Cr-o structures. For the Cr ordered structure, the inclusion of spin-polarization did not do much in case of phase stability, as the difference is only 0.01 kJ/mol which was very interesting considering that for all the other structures hcp was the more impacted one. For the Ni-o there seems to be an effect on fcc structure as it lies more in line with the other randomly ordered ones. It is possible that the Cr ordering in the Ni-o structure, as there will always be some because of the limited possibilities to occupy lattice sites thanks to the Ni ordering, is causing higher stabilisation when spinpolarization is included as the $\alpha_{\rm Cr-Cr}=0.16$ for this structure. This was in the direction of the stabilisation effect of Cr ordering. Taking into account the hcp Cr-o results this shows higher influence of Ni than Cr on the hexagonal structures by including the spinpolarization.

4.3.2 Magnetic moments

The local magnetic moments were studied to reveal the effect of including spin-polarization beyond just phase stability and to explain some of the differences found in Section 4.3.1. Magnetic moments were extracted by using the Bader method described in Section 4.2.3 but there was not a big difference between these values and those from VASP OUTCAR file. First analysis was done similarly as in [11], in other words looking for dependencies between local magnetic moments of atoms on average magnetic moments in the 1st NN. The values of magnetic moments were not considered as absolute so the spin up and spin down properties were preserved. The randomly ordered structures had very similar trends.

In all three structures, Ni seemed to increase its magnetic moment up to $0.5\,\mu_B$ together with increasing average magnetic moment in its 1st NN, that was for both fcc and hcp. There was just a slightly higher distribution for Ni in hcp 2 around $0.18\,\mu_B$ average magnetic moment in 1st NN compared to the other structures and the local magnetic moment values were thus present with much narrower distribution (red curves in Figure 4.7a). Cobalt had similar trend with some difference in reaching higher values of local magnetic moments. Although, there was some difference in distribution of magnetic moments in fcc 3. Both fcc and hcp in cells 1 and 2 had quite compact distribution visible as overlapping distribution functions in Figure 4.7b but there was difference in the fcc and hcp 3. The magnetic moments for hcp 3 reached higher values as the peak of the distribution (brown curve in Figure 4.7b) for local magnetic moments is around $1.10\,\mu_B$. To the contrary, the fcc 3 had lower values of magnetic moments with the peak around $0.70\,\mu_B$ with a higher spread of values compared to the hcp 3 and all the other structures as well. This was probably tied to the difference in their mixing enthalpy as the fcc 3 structure seems to have suppressed magnetic moments while the hcp 3 seems to be affected the other way with



(a) Ni magnetic moment distribution. (b) Co magnetic moment distribution.

Figure 4.7: Ni and Co local to average in 1st NN magnetic moments in randomly ordered structures.

higher distribution in higher values. There were also a few atoms with very low but still spin down magnetic moments for the fcc structures.

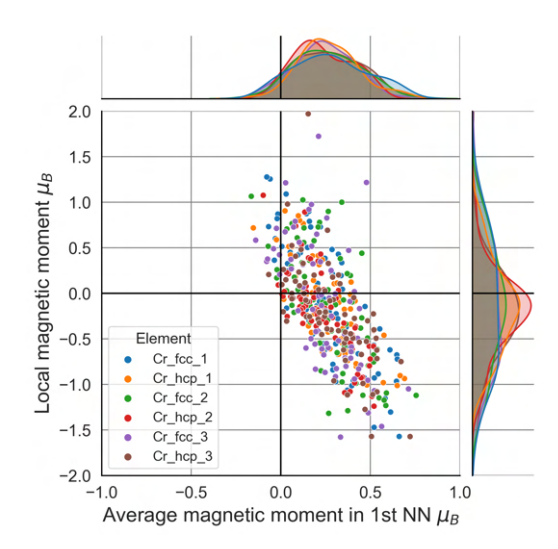
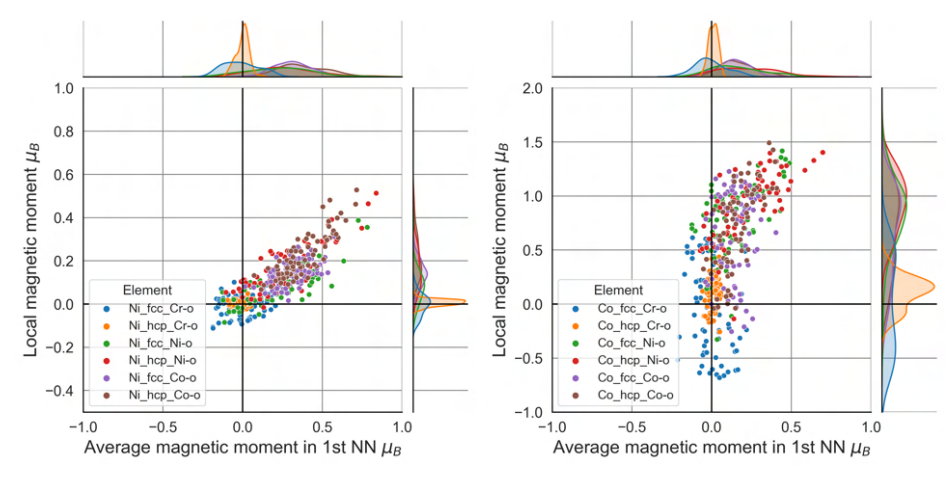


Figure 4.8: Cr magnetic moment distribution in randomly ordered structures.

The Cr magnetic moments result in a similar way. There was a slight difference between the cells 2 compared to others, hcp 2 and fcc 2 magnetic moment distributions were more centered closer to 0 compared to all the other structures. Other fcc and hcp cells had very similar distributions of local magnetic moments with fcc 1 and fcc 3 resulting in quite uniform distribution over all the received magnetic moments. Hexagonal structures had their distribution more centered in lower magnetic moment values with the peaks around $-0.20\,\mu_B$. Looking at the structures 3, it was hard to see any notable difference like for Co atoms, there was slightly broader distribution of the magnetic moments in fcc with few moments reaching slightly higher values but nothing extremely different from the fcc 1 structure and that the values were more concentrated around the average magnetic moment of $0.25\,\mu_B$.



(a) Ni magnetic moment distribution. (b) Co magnetic moment distribution.

Figure 4.9: Co and Ni Local to average in 1st NN magnetic moments in ordered structures.

The ordered structures result in quite different distributions with the biggest difference in Cr-o indicating that Cr has highest effect on magnetism of this alloy. Nickel magnetic moments in Cr-o structures were suppressed to values near zero in fcc and basically zero in hcp, as the peaks of local magnetic moments (orange in Figure 4.9a) for fcc were at $0.02 \mu_B$. For the fcc structure, some Ni magnetic moments even turned to spin down but considering the average magnetic moment distribution (blue distribution function in Figure 4.9a) for them, they probably just aligned ferromagnetically with their 1st NN. The other two ordered structures had similar distributions to the randomly ordered structures, although that may also be just an effect of generally small magnetic moment of Ni. Co magnetic moments for Cr-o were again suppressed comapred to the randomly ordered structures, especially in hcp. The distribution of Co magnetic moments in Cr-o was again concentrated around zero with peak around $0.10\,\mu_B$ but the average magnetic moment distribution is peaking barely above zero. In contrast, Co magnetic moments in Cr-o fcc were very spread out in comparison to hcp and the randomly ordered structures. There were many atoms with spin-down magnetic moment and basically two maxima of distributions (blue distribution function in Figure 4.9b) around $\pm 0.50 \,\mu_B$ and minimum around zero. The other two ordered structures result in similar distribution to the randomly ordered structures.

For the Cr in Cr-o structures, there was again similar trends as previously for Co and Ni. Magnetic moments in hcp Cr-o were again located closer to zero and had lower values (in between $-0.55\,\mu_B$ and $0.55\,\mu_B$) compared to fcc Cr-o. All the magnetic moments hcp Cr-o being so suppressed would explain such a small difference in mixing enthalpy for the non-spin-polarised calculation of this structure. Similarly to Co again, Cr magnetic moments distribution (blue in Figure 4.10) in Cr-o structure had minimum around zero and two maxima around $-0.50\,\mu_B$ and $0.80\,\mu_B$ with slightly higher occupancy around the upper maximum. Interestingly, in Co-o the hcp magnetic moments were also quite low while the fcc magnetic moments were similar to randomly ordered structures. For the Ni-o structures the distribution in fcc was similar to Cr-o with even more distinctive minimum around zero while hcp had mostly uniform distribution.

Other trends were visible when looking at the dependencies of local magnetic moment on the composition of 1st NN shell. For the purpose of analysis and readability, the magnetic moment values were used in absolute values. All the randomly ordered structures resulted

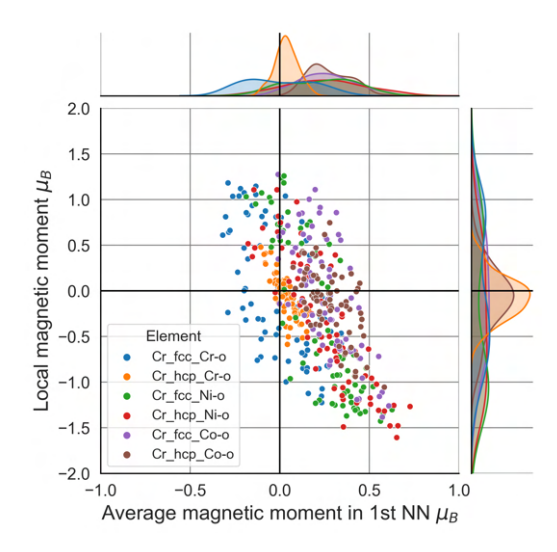


Figure 4.10: Cr magnetic moment distribution in ordered structures.

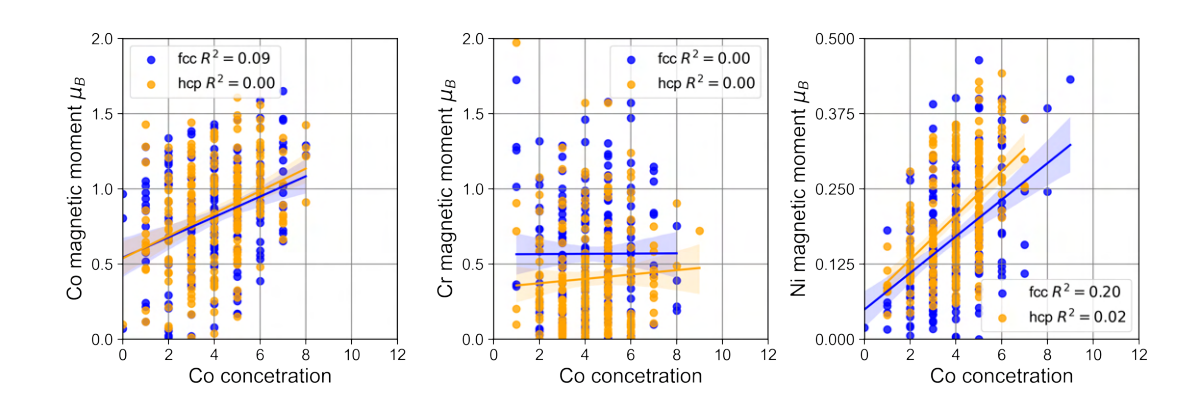


Figure 4.11: Magnetic moment dependence on Co in 1st NN shell.

in very similar trends. There was no dependence of magnetic moment on Co concentration in 1st NN shell (Figure 4.11) except slight dependence in fcc for Ni magnetic moment with $R^2 = 0.20$ while in hcp this dependence is not present, likely because of higher spread of values.

More interesting results were found for the concentration of Cr in 1st NN shell (Figure 4.12). Magnetic moments of all elements shown dependence on the Cr concentration in 1st NN. Most pronounced dependence was for Co magnetic moments in hcp with $R^2 = 0.83$ and in fcc with $R^2 = 0.73$ meaning with increased amount of Cr in 1st NN the magnetic moment of Co decreased. Same trend was found for Ni only with higher spread of values $R^2 = 0.59$ and $R^2 = 0.63$ for hcp and fcc, respectively. The least pronounced dependence was for Cr on itself in 1st NN with quite low values of R^2 compared to the other two elements. The dependence was still there and it was still visible that with higher amount of Cr in 1st NN the magnetic moment lowers as well. This is probably tied to the fact that it is not possible to arrange into antiferromagnetic orderings and thus magnetic frustration lowering the magnetic moments.

Lastly, the dependencies on Ni concentration in 1st NN shell were quite small (Figure 4.13). The most profound one was for Cr magnetic moment in fcc with the value of

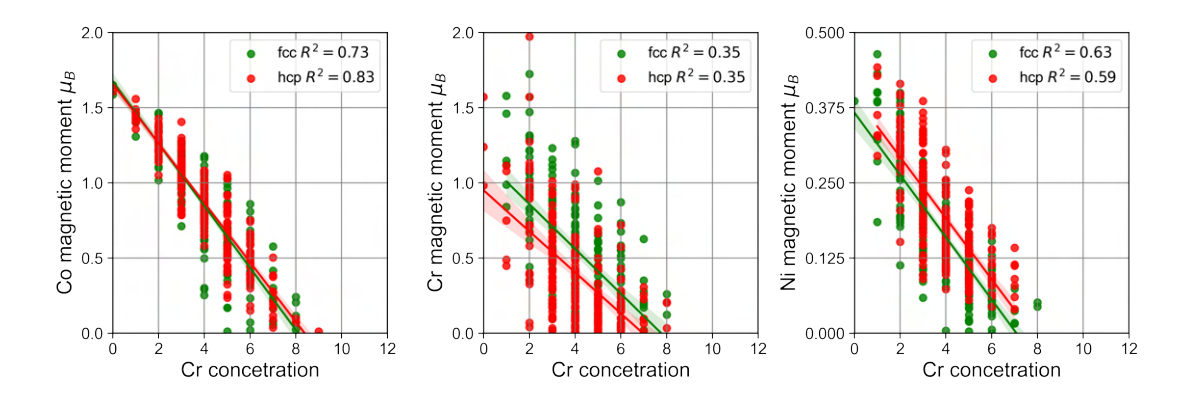


Figure 4.12: Magnetic moment dependence on Cr in 1st NN shell.

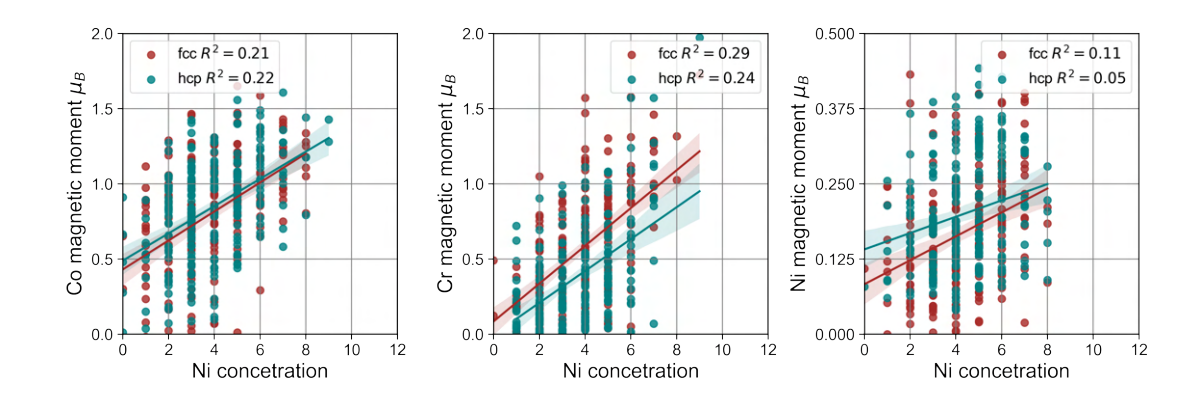


Figure 4.13: Magnetic moment dependence on Ni in 1st NN shell.

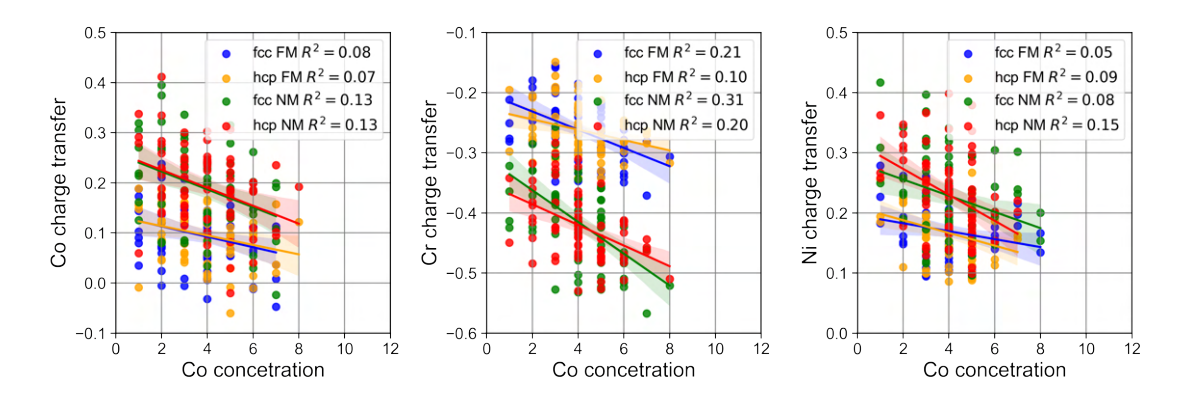
 $R^2=0.29$ followed by hcp with $R^2=0.24$. In these cases, magnetic moment was increasing with higher amounts of Ni in 1st NN. Even lesser dependence was found for Co magnetic moments but the same trend of increasing magnetic moments with increased concentration was present. The ordered structures were not analysed as the values were not spread to create any kind of dependence tied to the ordering.

4.3.3 Charge transfer

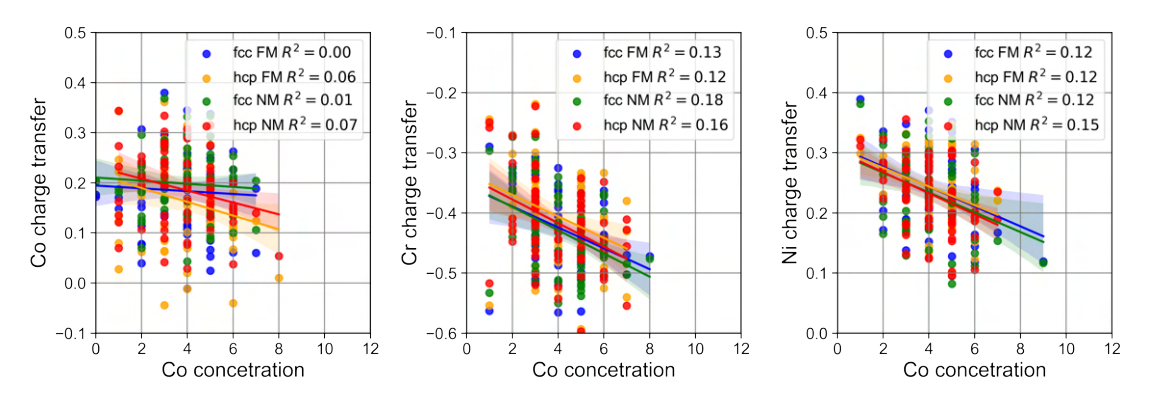
The results of Bader analysis [89, 91] show charge transfer ongoing between the elements. There were similar dependencies of the charge transfer on the 1st NN as the magnetic moments. There was also a difference between the cells 1 and 3. For all the values of charge transfer in cells 1 the charge transfer was always lower in spin-polarised (FM) calculations than in non-spin-polarised (NM). On the contrary, the cells 3 had about the same amount of charge transfer in both spin-polarised and non-spin-polarised calculations with the spin-polarised calculation resulting in higher amounts of charge transfer compared to the cells 1.

No high dependence of charge transfer was present on Co concentration for both cells (Figure 4.14), only a small dependence for fcc 1 in non-spin-polarised state for Cr with $R^2 = 0.31$. In fcc 3 the R^2 value was smaller but still the highest of all received. The trend seems to be that the charge transfer on Cr was increasing with increasing amout of

Co in 1st NN. For the other two elements the trend is decreasing meaning less charge was transfered, in their case accepted, the more Co was in the 1st NN shell.



(a) Co charge transfer dependence on 1st NN composition in cells 1.

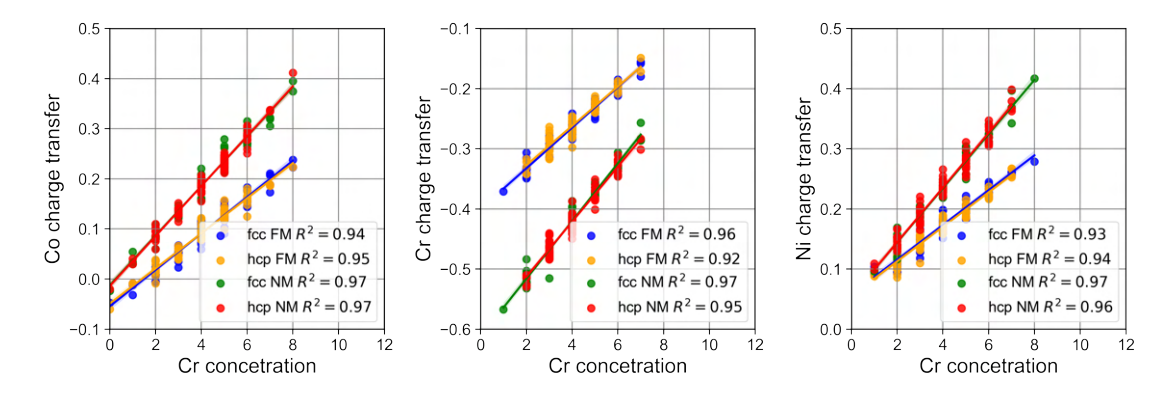


(b) Co charge transfer dependence on 1st NN composition in cells 3.

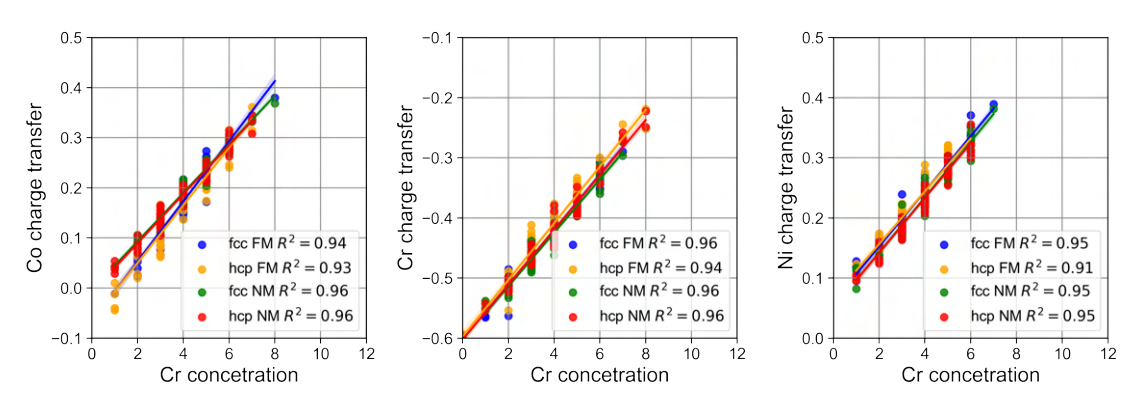
Figure 4.14: Co charge transfer dependence on 1st NN composition.

The most interesting were again the dependencies on Cr in 1st NN shell. The dependencies for both sets of cells 1 and 3 are basically linear for all elements. All of the dependencies had the R^2 value above 0.90 with the lowest value received for spin-polarised hcp 1 $R^2 = 0.91$, which was still quite a high value. The charge transfer minimises with increase of Cr concentration in 1st NN for Cr atoms, as the more Cr atoms there were, the less charge was released. For Co and Ni it was the other way around meaning they had accepted more charge with more Cr in their 1st NN. This agrees with XANES measurements done by Tan et al. [83] in which Cr is shown as the element with the most flexible electronic structure. The differences between the cells 1 and 3 were also more pronounced as the fcc 3 and hcp 3 Cr charge transfer basically overlap.

There was some dependence of charge transfer on the amount of Ni in the 1st NN shell mostly for Co and Ni (Figure 4.16). Following the previous trends, with higher Ni concentration in 1st NN shell Co and Ni charge transfer lowered while Cr increased its amount of released electrons. The dependence was more pronounced than for Co concentration, but not as pronounced as Cr highlighting Cr as the most important actor in charge transfer in this alloy.



(a) Cr charge transfer dependence on 1st NN composition in cells 1.

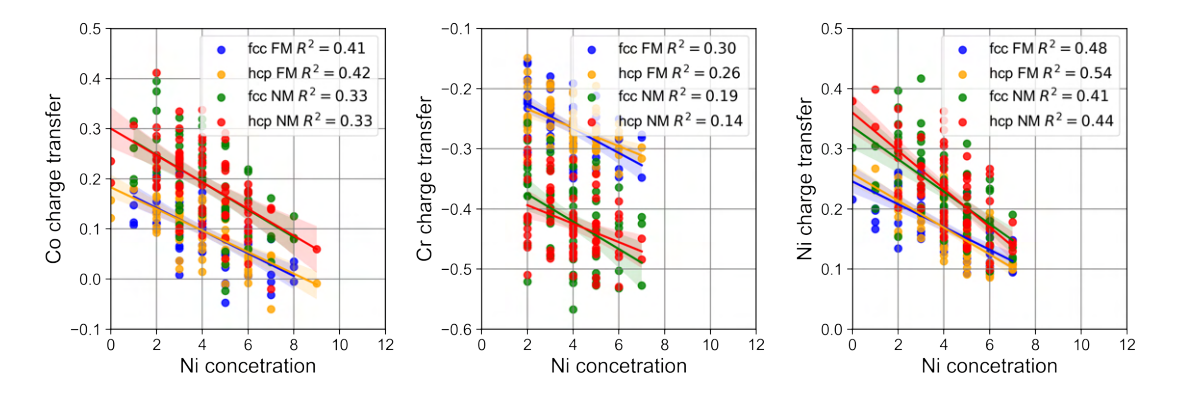


(b) Cr charge transfer dependence on 1st NN composition in cells 3.

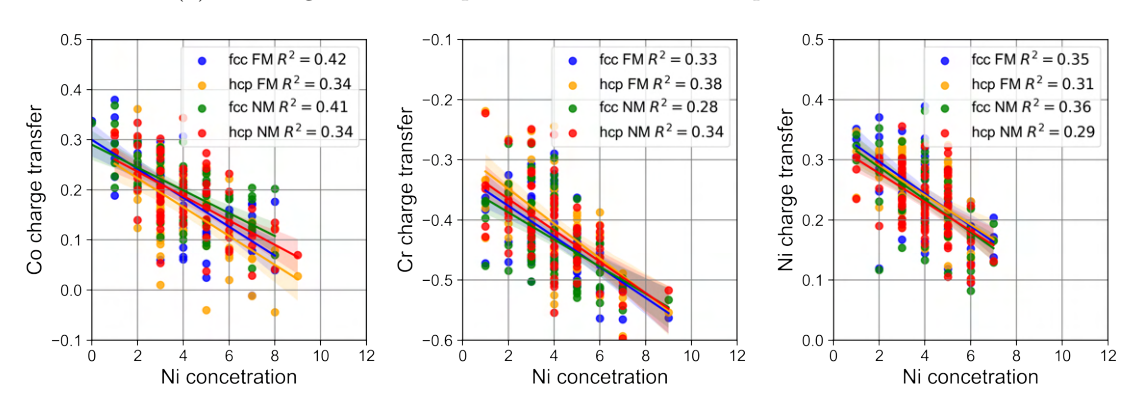
Figure 4.15: Cr charge transfer dependence on 1st NN composition.

The increase of charge transfer in cells 3 could provide some explanation as to why the magnetic moments in the fcc were suppressed. Another difference between cells 3 and 1 was the fact that Co has released some electrons in both spin-polarised calculations for cells 1 but for the cells 3 it only did so for a few cases in hcp,. Otherwise it always acted as an acceptor, this could also influence the magnetism in a way. Higher amount of charge transferred from Cr could cause the lower values of magnetic moments but it is interesting that this effect was not present in the hexagonal structure, it could be explained by different plane stacking and thus a higher influence of 2nd NN shell for which there was a difference in Cr - Cr and Co - Co ordering between fcc 3 and hcp 3 with the lesser amount of bonds of both in hcp 3. For the ordered structures the charge transfer was following the same trends as cells 1 for the specific values of composition in 1st NN. As again the spread of values was limited by the ordering, the dependencies were not really visible.

Linking the charge transfer to magnetic moment other clear dependencies appear. Here, the magnetic moment values were taken as absolute, so that the analysis would be possible. Co magnetic moment was nearly linearly dependent on the amount of charge transferred, with the lesser amount of charge Co released the higher magnetic moment it had. Second in dependencies was Ni with same trends of higher charge transfer resulting in lower magnetic moment. For Ni, the dependencies were not as clear and linear as Co with higher spread



(a) Ni charge transfer dependence on 1st NN composition in cells 1.

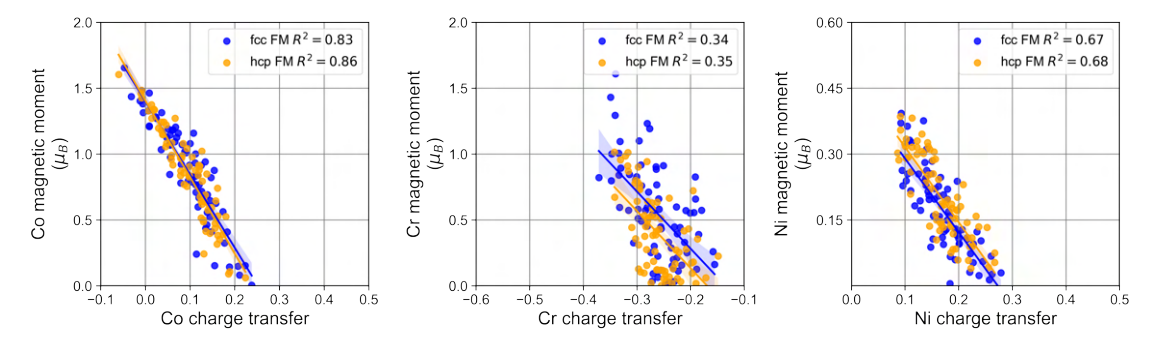


(b) Ni charge transfer dependence on 1st NN composition in cells 3.

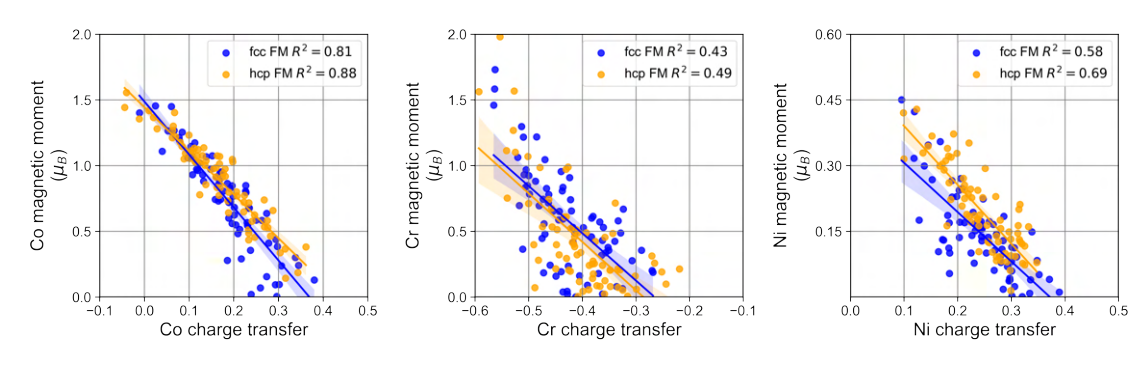
Figure 4.16: Ni charge transfer dependence on 1st NN composition.

 $R^2=0.67$ in fcc and $R^2=0.67$ in hcp for cells 1 and $R^2=0.58$ in fcc and $R^2=0.69$ in hcp.

The cubic fcc 3 had higher spread of values compared to the fcc 1. The magnetic moment values were also quite different between fcc 3 and hcp 3, as mentioned in Section 4.3.2. Cr did not really have a clear dependence as the spread of values is quite high in all cells. However, there were similar trends of higher magnetic moment with higher amount of magnetic moment released. Together with the dependence of charge transfer on the amount of Cr in 1st NN shell this could provide an explanation into how phase stability is influenced by Cr. For the Cr-o structure the charge transfer was very similar to cells 1 and as well for both fcc and hcp structures and for both FM and NM calculations. Co has accepted 0.12 to 0.18 electrons, Ni accepted slightly more, between 0.24 and 0.18. Lastly, Cr had released 0.30 to 0.38 electrons. These values are approximately equal to the values of FM calculations of cells 1 for those specific concentration values. The magnetic moment values not exceeding 1.30 μ_B for fcc is again in line with what is shown for Cr magnetic moment in Figure 4.17a. Same goes for Co and its magnetic moment values for fcc being under 0.75 μ_B . The suppresion of magnetic moments in hcp can not be explained purely by these as for hcp 1 this effect did not appear.



(a) Magnetic moment dependence on charge transfer in cells 1.



(b) Magnetic moment dependence on charge transfer in cells 3.

Figure 4.17: Magnetic moment dependence on charge transfer.

4.3.4 UMLIP comparison to DFT

Firstly, the energies from DFT and CHGNet prediction are compared. As can be seen in Figure 4.18 there is quite an error. CHGNet overestimates the stability of all structures by nearly 0.2 eV/atom. It is interesting to see that there really is not much of a difference between the error in hcp and fcc structures (Figure 4.19). The better agreement for Cr-o structures is simply caused by their lower energies from DFT. CHGNet puts them with similar energies to all the other structures, thus the lower energy from DFT puts them closer to these values. Applying the CHGNet to the pure elements it was possible to obtain a mixing enthalpy from just ML prediction (although in reality these are easy calculations and would not need this approach). It is expected that since the energies of the HEA structures are so much different, the accuracy of mixing enthalpy is also not going to be very accurate. Looking at both approaches (Section 4.3.4), e. q. mixing enthalpy only from CHGNet or from CHGnet energies for HEA and DFT from elements, it is visible that this model is not doing great for this material. Reaching root mean square error (RMSE) values of 18 kJ/mol for the apporach of including DFT energies for elements means that this approach is unusable and it is safer to use the CHGNet energies for elements as well. Even then, the error reaches values of 8 kJ/mol and is proposing stability where DFT shows positive values of mixing enthalpy. Sadly, as a lot of the necessary data for retraining was on a hard drive that failed, it cannot be refitted to improve accuracy.

Trained forces depend on the energies so with that big errors of the UMLIP for the energy one would expect quite big errors for forces as well. This turned out to be true as

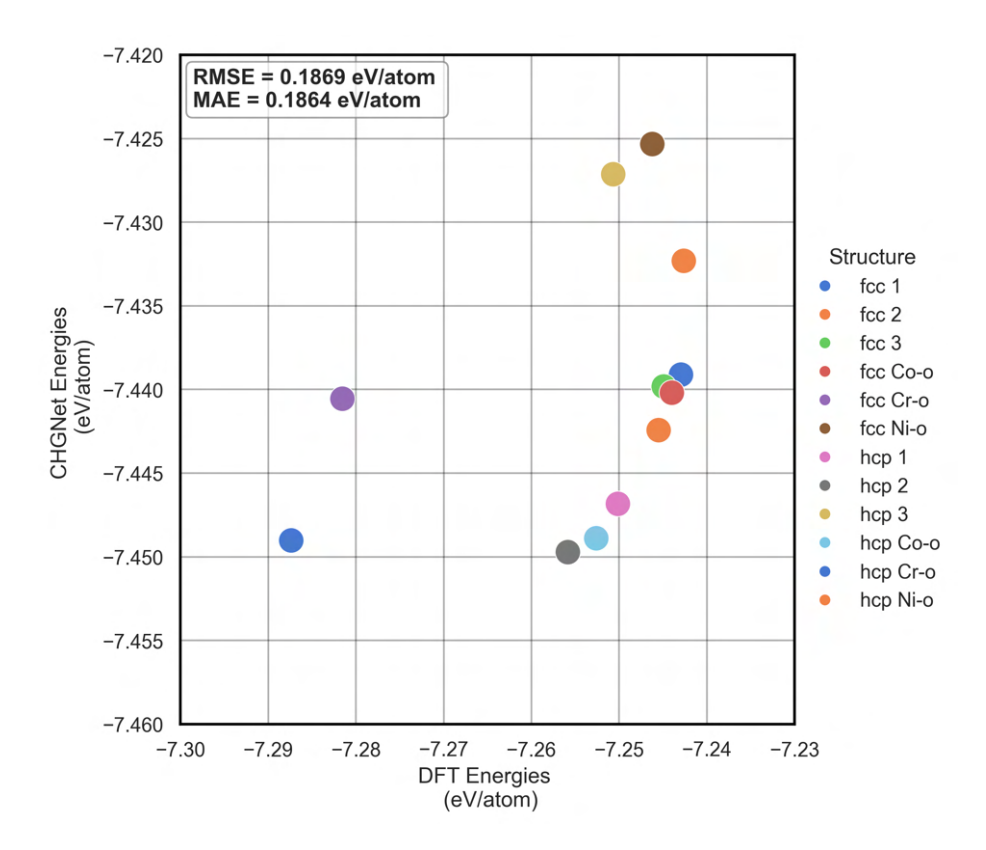


Figure 4.18: Comparison between energies obtained via DFT and via CHGNet UMLIP.

| Element | DFT Energy (eV/atom) | CHGNet Energy (eV/atom) |
|---------|----------------------|-------------------------|
| Co | -7.0368 | -7.0279 |
| Cr | -9.4971 | -9.5370 |
| Ni | -5.4670 | -5.7445 |

Table 4.4: Energy values for elements obtained via DFT and CHGNet.

the forces result in RMSE of 0.2 eV/Å. Looking at the validation reported in the MPTraj [59] of 0.008 eV/Å from CoCrNi the obtained error is of orders of magnitude higher. Looking at the MPTraj dataset [59] the settings used for obtaining the data in the dataset give the reason for this high error. The force convergence criterion was set to 0.02 eV/Å [59]. This value is few orders higher than what was used for DFT calculations for CoCrNi. For the energies, the situation is slightly different as there the convergence criterion was 10^{-6} eV [59] which is the same as was used in the DFT calculations. It may be that the CHGNet can not really deal with the HEA as the dataset may not include many of them and thus the model struggles with extrapolation and thus sufficient refitting would improve performance. On the other hand, with errors in forces like these, it makes little sense to try and use Phonopy to obtain phonons as those depend quite heavily on well converged forces [44, 45].

Last part that the model is trained on are the magnetic moments. As was described in Section 3.7.1 the magnetic moments training is independent of the energies and forces so that could mean improvement of predictions. Especially if one considers that the magnetic moments in this alloy depend on charge on ions quite reasonably as was described in previous results. As was mentioned in the description, the model cannot predict the orientation so

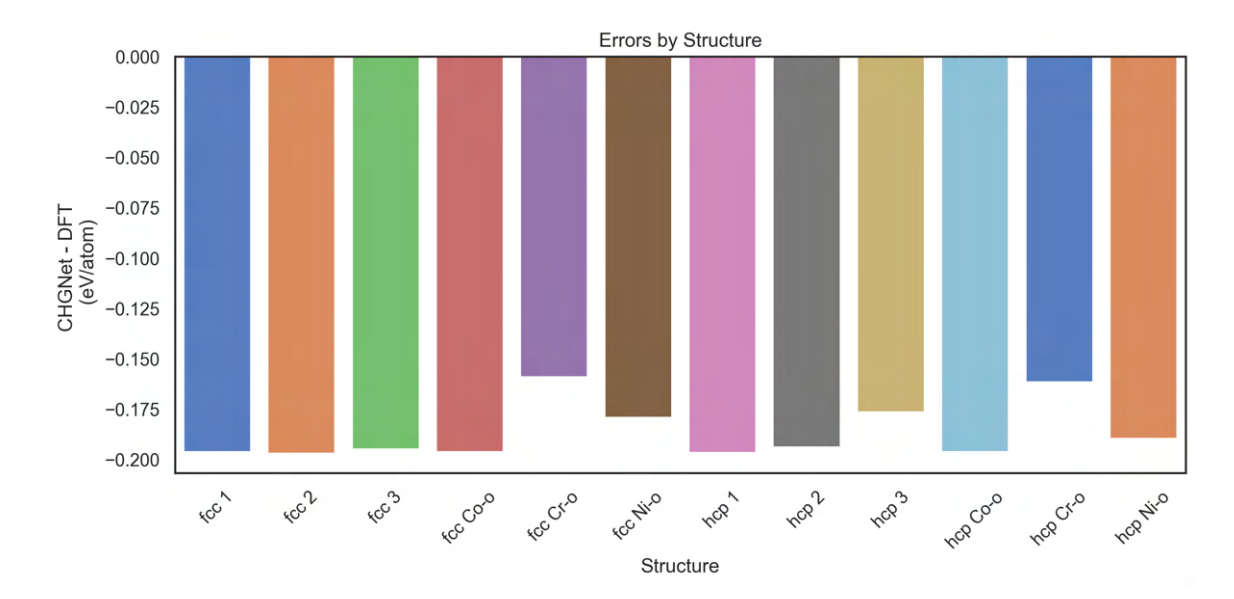
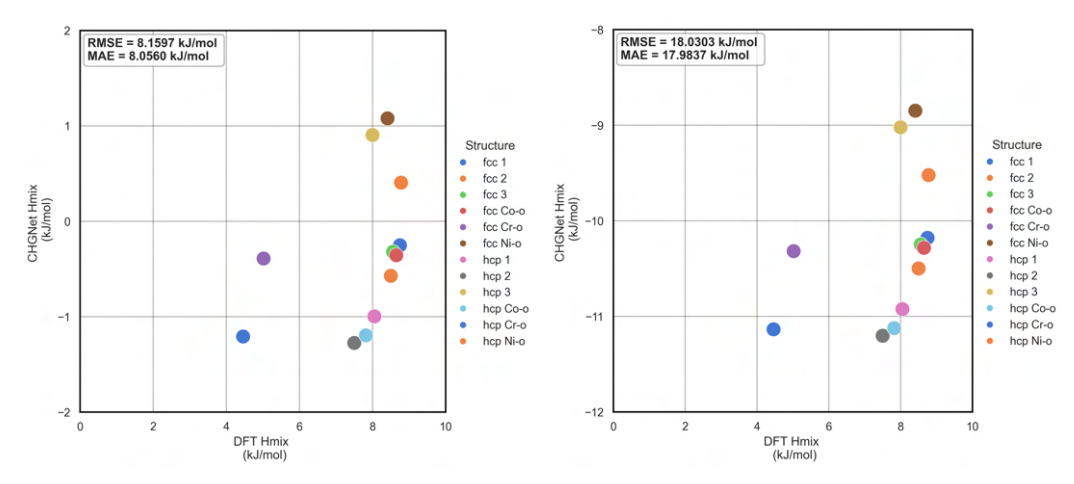


Figure 4.19: Errors obtained for all the calculated structures.

the values from DFT calculation have to be included in absolute values. Reported errors from the CHGNet publication [59] are $0.032~\mu_B$ but from the DFT on CoCrNi it was, again, by an order of magnitude higher. Looking at the Figure 4.24 it can be seen that the majority of errors arise from the Ni ordered structures as well as the hcp Cr ordered structure. This hints at a possibility of the model to somehow correctly predict the disordered structure out of the box. The ordered structure, which will probably not be included that often in the training dataset, represents quite a struggle. Especially, the hcp Cr ordered, which as was described in Section 4.3.2, has magnetic moments frustrated to values very close to zero. What is surprising is the very high error in the Ni ordered structures. There is probably a significant part in the training dataset where in some alloys containing some Cr or Co together with Ni have quite low magnetic moment. Otherwise, for the random solutions, this model could be used even without pre-training to get at least an idea of the sizes of magnetic moments. With the accuracy levels even without any refit, it probably would not need many structures to correct this model. These structures would have to be mainly the ordered ones.



- (a) CHGNet elements energy prediction.
- (b) CHGnet with DFT elements energy.

Figure 4.20: CHGnet energy predictions.

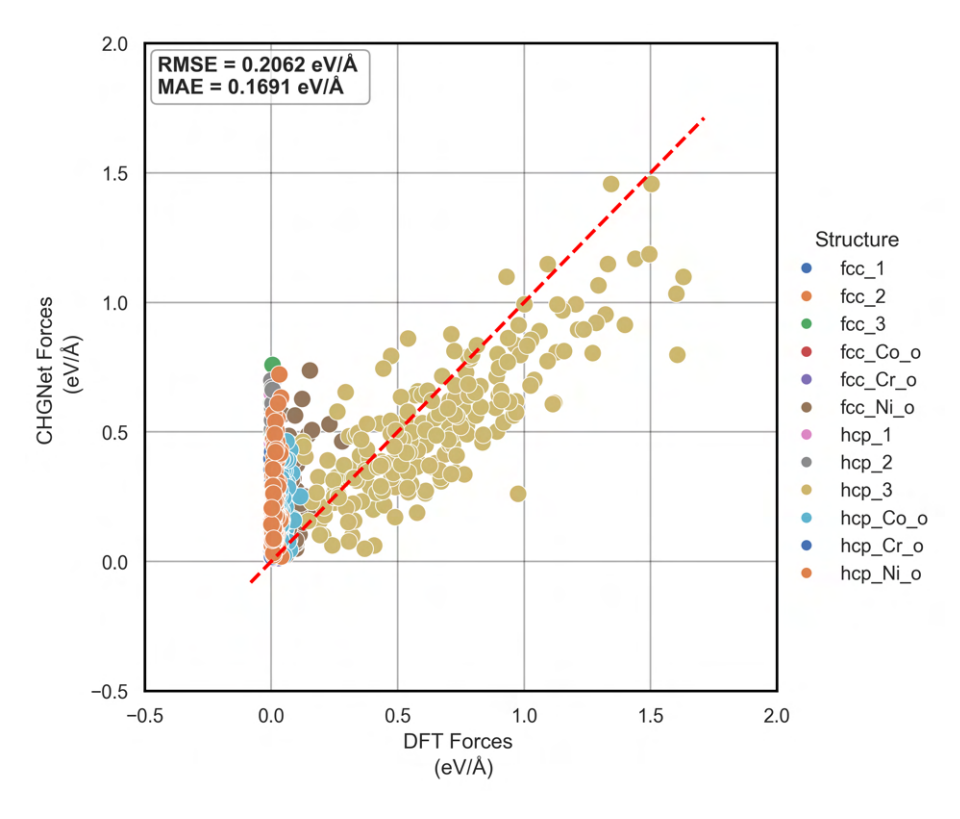


Figure 4.21: Comparison between forces obtained via DFT and via CHGNet UMLIP.

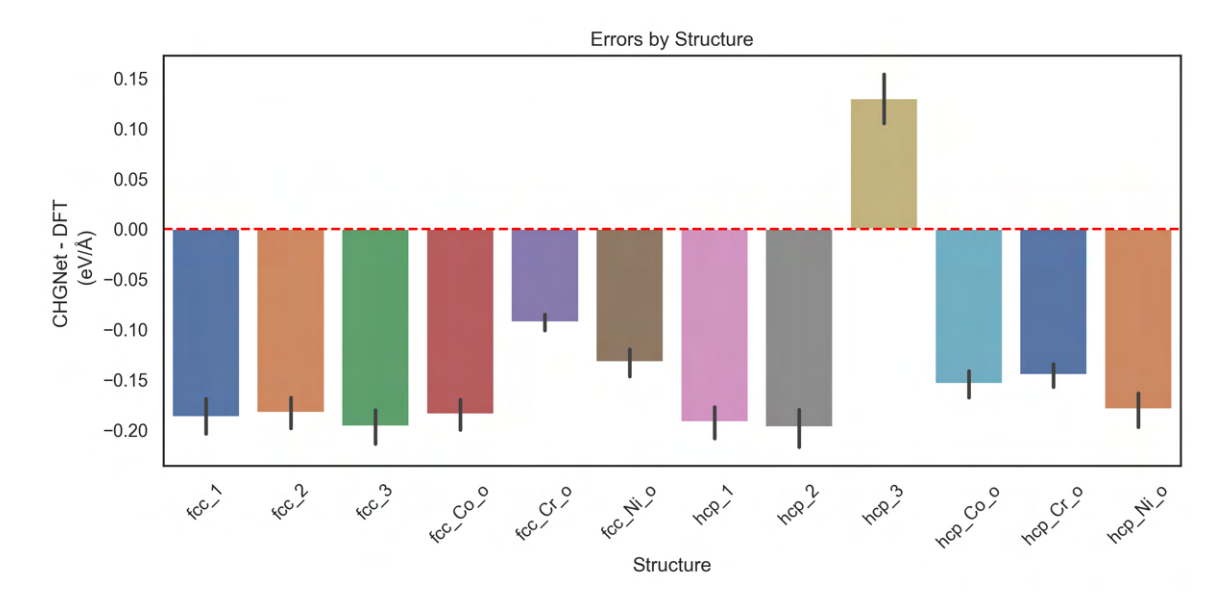


Figure 4.22: Errors obtained for forces for all the calculated structures.

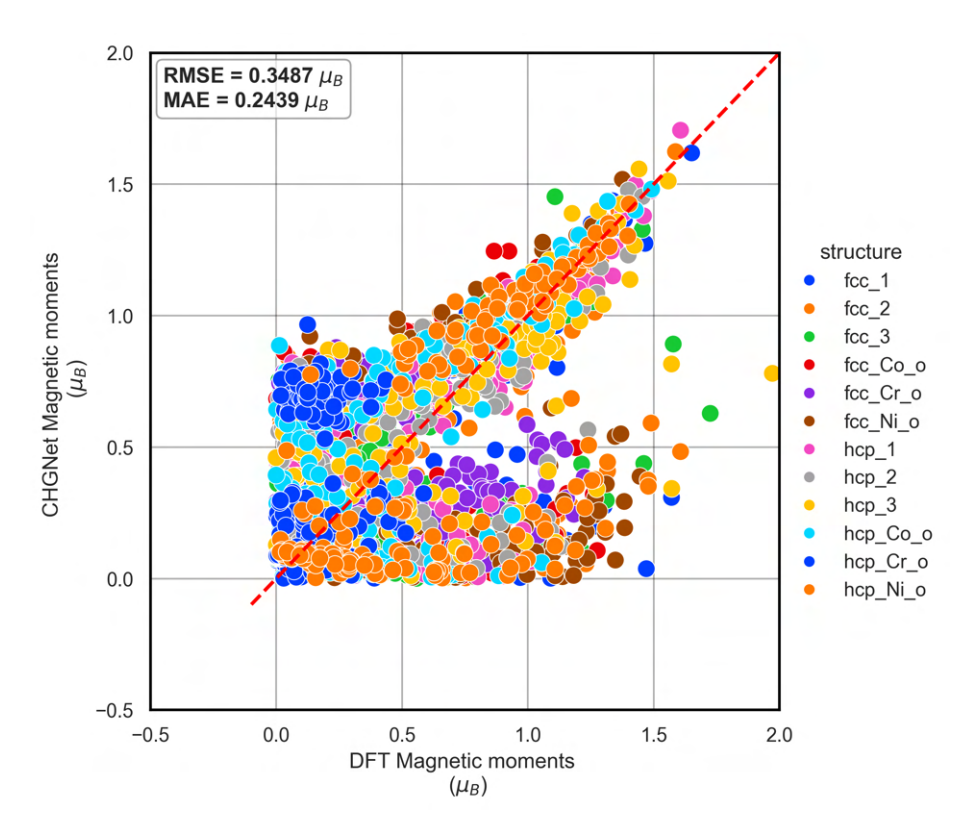


Figure 4.23: Comparison between magnetic moments obtained via DFT and via CHGNet UMLIP.

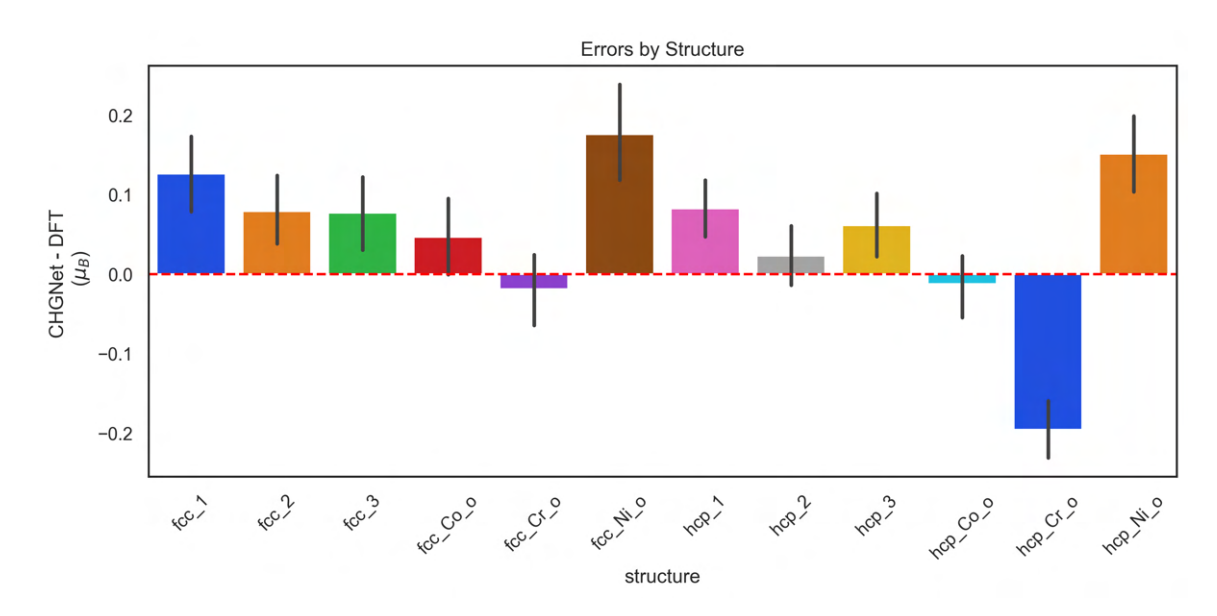


Figure 4.24: Errors obtained for magnetic moments for all the calculated structures.

4.3.5 MD runs with GRACE

The relative stability between fcc and hcp can be seen in Figure 4.25. The fcc always results in slightly lower enthalpy, but both structures have very similar values. This confirms the experimentally observed fcc structure as the more stable one already at 200 K. On the other hand, the enthalpy differences are quite small which is partially in agreement with experimentally observed and previously calculated low stacking fault energy [12, 69, 71]. Considering the model was not refitted at all, these are quite good results. The MD runs at 900 K for fcc have very similar radial distribution function to the results obtained by Foley et al. by EAM potential [99]. More importantly, even at higher temperatures the radial distribution function does not change too much, hinting at chemical SRO not disappearing, as can be seen in Figure 4.26. At 1100 K the common neighbour analysis finds some changes to the fcc structure. Around 11% of atoms switch to the "Other" count, meaning some displacement is happening from the original fcc cell. The analysis script did not observe any atomic type switches on positions, so this is purely a local deformation of nearest neighbours, not necessarily a change in SRO. This is also confirmed by a visual check, where the structure does not really change over all the trajectories. It may be possible that at longer simulation times or maybe using multiple fixes, i. e. starting the simulation from higher temperature to give the system more energy for faster transformation would reveal more.

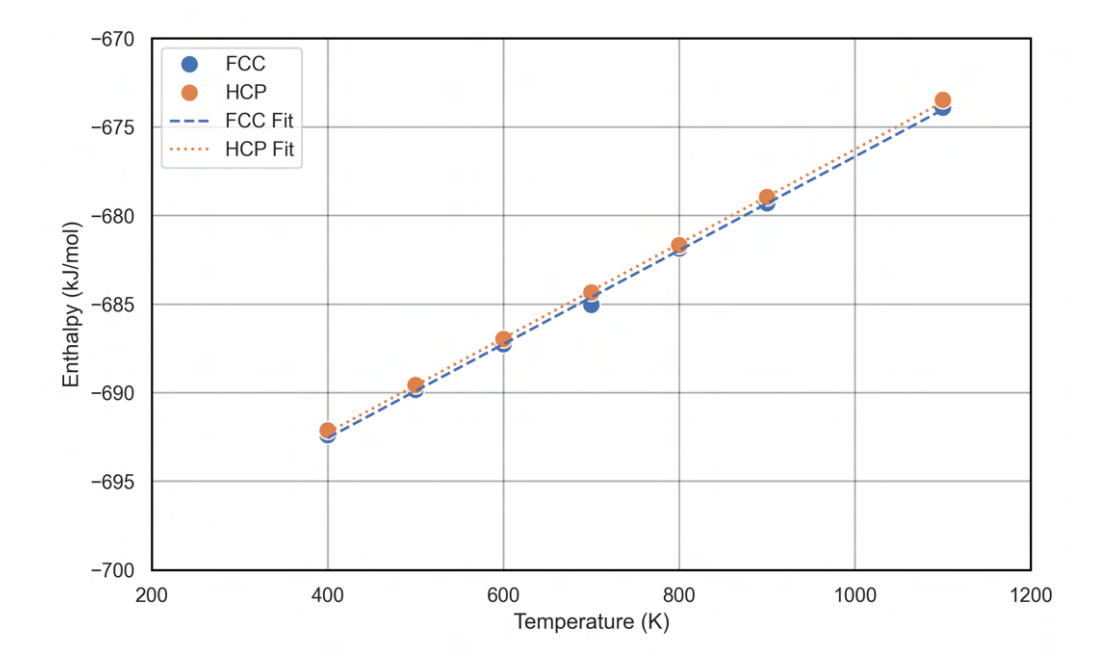
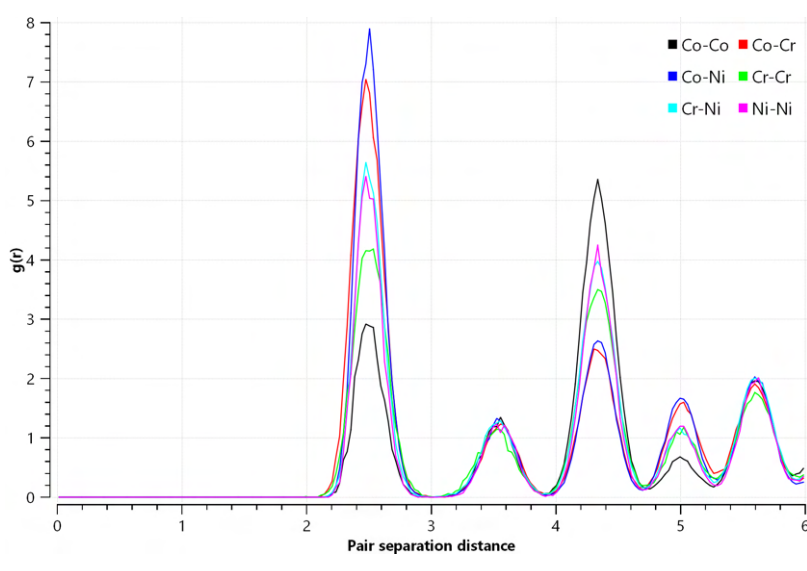
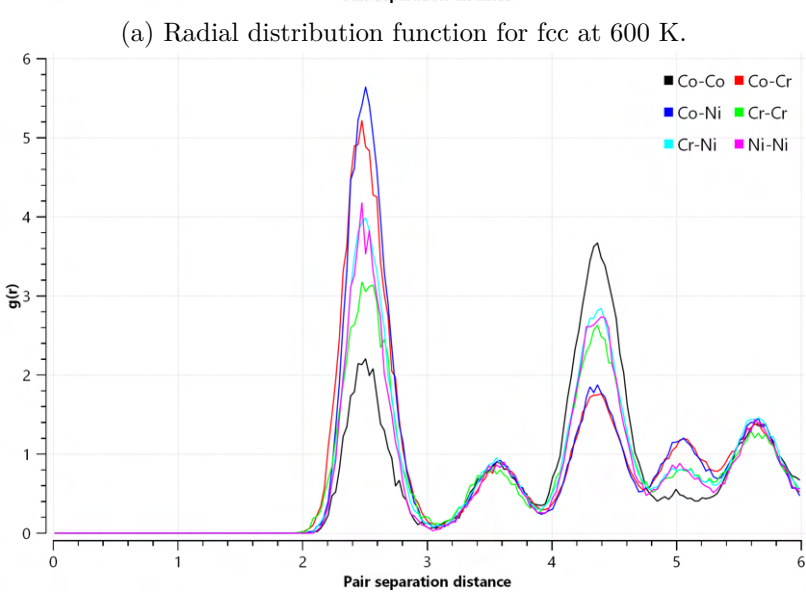


Figure 4.25: Enthalpy obtained from MD runs.

For the hexagonal phase the situation was mostly the same. The RDF peaks were slightly different at higher temperatures. The third and 4th peak at 600 K merge into one at 1100 K. This could be explained by looking at the common neighbour analysis, specifically at its render. The approximately 11% change from hcp to "Other" count was observed in hcp in the same way as fcc. Same situation was for the atomic swaps, no atoms have changed their positions completely so again it is just local distortion. Only when looking at the structure visually some differences were clearly visible. In fcc (green atoms) the change

to other (white atoms), visible in Figure 4.30a), was mostly small clusters or single atoms that were displaced. Meanwhile for hcp, visible in Figure 4.30b), the displacement (white atoms) was more tied together into larger clusters. Additionally, very small fractions of bcc local neighbourhoods (blue atoms) were observed. Here it would be even more interesting to observe longer simulation runs to observe what would happen.





(b) Radial distribution function for fcc at 1100 K.

Figure 4.26: Radial distribution function for fcc.

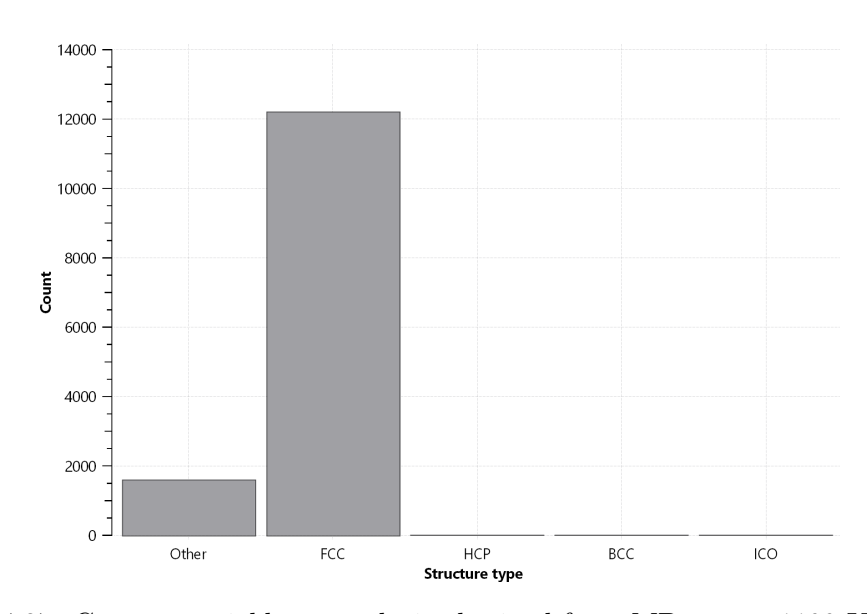
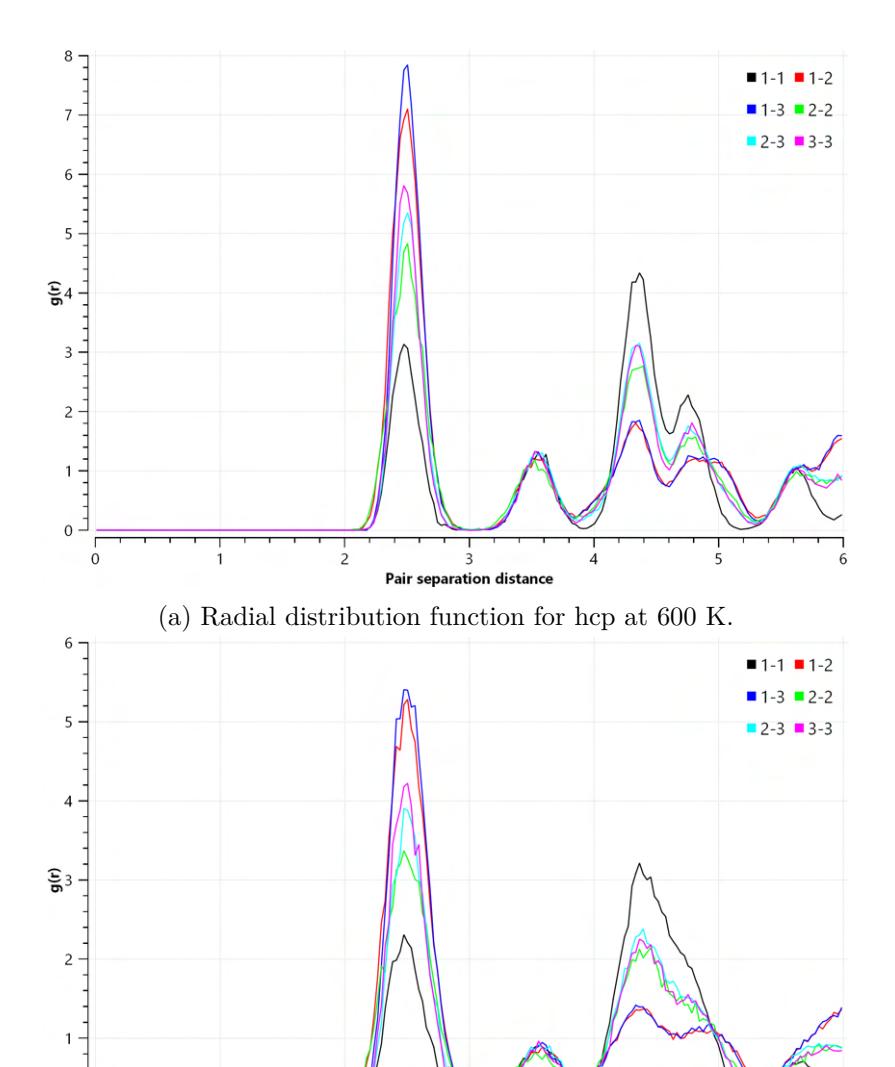


Figure 4.27: Common neighbour analysis obtained from MD run at 1100 K for fcc.



(b) Radial distribution function for hcp at 1100 K.

Figure 4.28: Radial distribution functions for hcp.

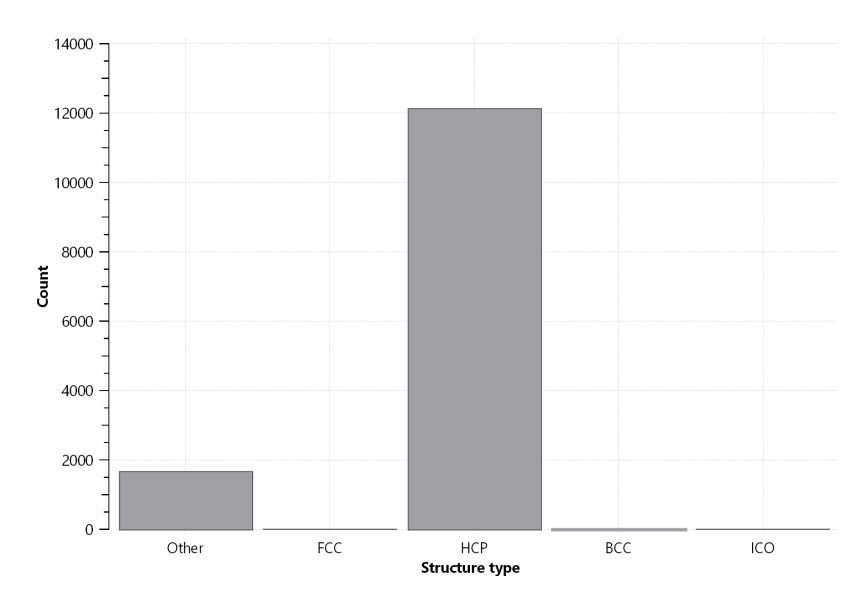
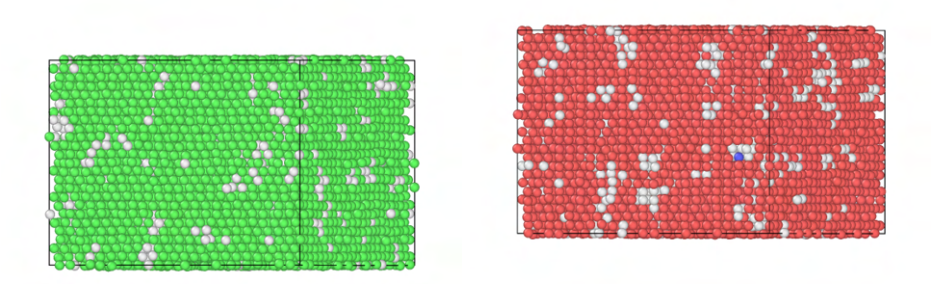


Figure 4.29: Common neighbour analysis obtained from MD run at 1100 K for hcp.



(b) CNA visualisation for hcp at 1100 (a) CNA visualisation for fcc at 1100 K. K.

Figure 4.30: CNA visualisations, fcc structure is green, hcp is red, white are the displaced atoms, blue is some displacements into bcc structure.

5. YMn₂ calculations

5.1 Motivation and literature review

This intermetallic is an interesting compound to study because of its abnormal lattice expansion at Néel temperature of 100 K. The compound crystallizes in a cubic C15 Laves phase with two Y atoms at 8a $(\bar{4}3m)$ positions and four Mn atoms at 16d $(\bar{3}m)$ positions. It is also possible to find it in C14 Laves phase which is less stable than C15 [100]. Its magnetic ordering is still unclear as there are conflicting reports. The reported states range from simple antiferromagnet [17] to helimagnetic structure [18, 101] with quite high q vector of 430 Å[18, 102] and also double-axial spin structure [102]. The abnormal lattice expansion is tied to the antiferromagnetic to paramagnetic phase transition at Néel temperature and results in about 5% volume increase when cooling down from the paramagnetic state [16, 103, 104]. There is also a small tetragonal distortion present at the transformation at 100 K according to Nakamura and Shiga [102] and Cywinski [18] of 5% as well. The hexagonal C14 Laves phase type does not exhibit this behaviour [100]. The magnetic moment is concentrated only on the Mn atoms with the value of $2.7\mu_B$ reported by both previous experimental measurements and theoretical calculations [16, 105–108]. The magnetic state itself is very sensitive to any chemical changes as just 3% substitution of Y by Sc changes the magnetic moments [109]. Other elemental substitutions have similar drastic effects on the magnetism of this compound. Interestingly, another Y and Mn binary compound Y_6Mn_{23} has anomalous thermal expansion above Curie temperature as well except in opossite direction. For the Y₆Mn₂₃ the abnormal expansion occurs above Curie temperature in the paramagnetic state from 500 K [110].

There were attempts to use the volume expansion as a means for hydrogen storage [106, 107, 111] and there were some interesting findings about the magnetism. DFT calculations by Pajda et al. [112] were done using full-potential linear muffin-tin orbitals without spin-orbit coupling for a calculation cell of 6 atoms with further hydrogen added into it to calculate the hydrides. The hydrogen compensates the growth of magnetic moments on Mn atoms and keeps them around $2.6 \,\mu_B$ through hybridization of H with Mn atoms. If placed into a different spot the hydrogenated alloy can even become slightly ferrimagnetic. In deuterized YMn₂D₆, the phase transition at Néel temperature is surpressed completely [100]. For concentrations of hydrogen higher than 0.75 the magnetic ordering changes to ferromagnetic [113, 114].

Chen et al. [108] did DFT + U calculations through VASP for YMn₂ as well as other rare-earth RMn₂ compounds and received the mixing enthalpy $H_{mix} = -11.3$ kJ/mol for C15 antiferromagnetic configuration. Their selected U and J parameters were 1.7 and 0.95 eV respectively [108]. They have received a slightly higher value of magnetic moment (3.3 μ_B) compared to previously reported 2.7 μ_B . Iwasaki et al. [115] employed the Korringa-Kohn-Rostoker Green's function method to caculate the different antiferromagnetic structures with both LDA and GGA potentials. Their results predict a [0 0 0] antiferromagnetic ordering to be more stable than one of the experimentally observed [0 0 1] antiferromagnetic structures.

Pulkkinen et al. in 2020 did meta-GGA calculations with SCAN functional on pure Mn [19]. In their results SCAN has successfully managed to describe complicated magnetic ordering of α -Mn (4 different antiferromagnetic sublattices). They have also shown SCAN's ability to predict basically similar density of states to GGA + U method in collinear mag-

netism setting allowing the bypass of empirical U and J parameters and showing that the SCAN functional can describe the Coulomb interactions well.

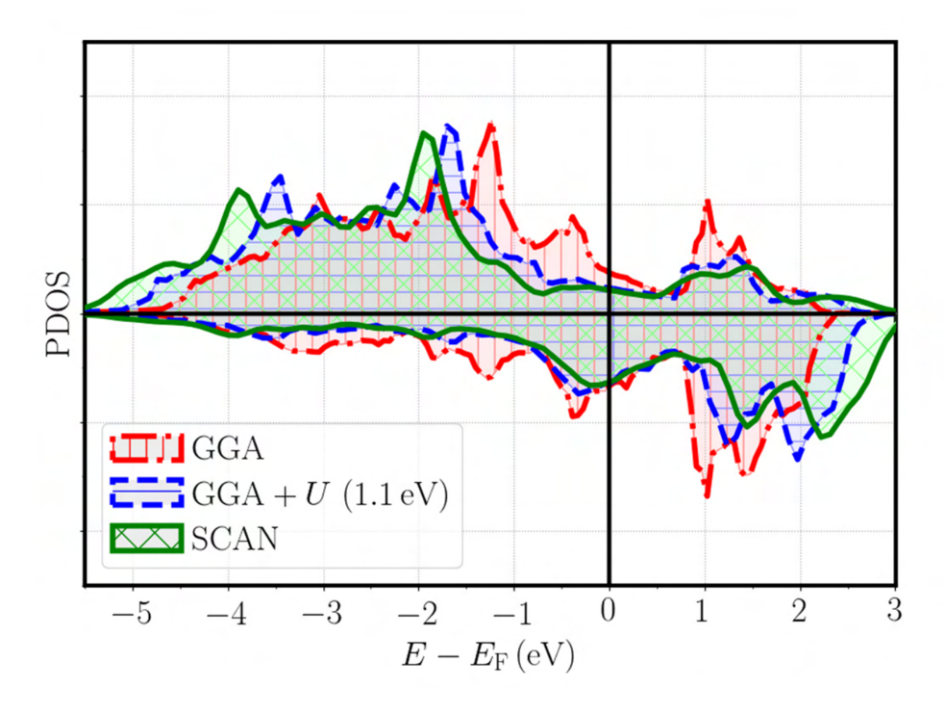


Figure 5.1: Comparison between densities of states via GGA, GGA+U and SCAN for pure Mn, taken from [19].

5.2 Methods and models

5.2.1 Models

To simulate the compound, a conventional C15 Layer unit cell was used with 24 atoms, 16 Mn and 8 Y atoms. The various magnetic structures that were generated contained a ferromagnetic ordering (FM) and 7 different antiferromagnetic orderings. The initial magnetic moments were all set up along the [0 0 1] direction. One was generated to have as much of antiferromagnetic ordering as possible (AFM1), two were generated from previously experimentally measured and proposed orderings (AFM2, AFM3) [17] and then three with randomised magnetic moments generated by sqsgenerator [49] to obtain different ordering than pure antiferromagnetic with various levels of ferrimagnetism (AFM4, AFM, AFM6). Another experimentally observed ordering was added as the AFM7 structure from [101] but it was only considered for the metaGGA calculations. The two orderings AFM2 and AFM3 were basically the same structure in case of spin-up and spin-down setup but with a different axis of magnetization. This means that AFM2 direction of magnetization was [0 0 1] and AFM3 would have to be magnetized along [1 0 0] direction to be completely equal. For AFM6 the magnetic moments were basically randomly distributed between Mn atoms with spin-up and spin-down. This was achieved by using the sqsgenerator on just the Mn sublattice without Y atoms. For the sake of simplicity, half of the Mn atoms were replaced with some other element, so that the values of W-C parameters received from sqsgenerator were immediately correct. With Mn atoms representing the spin-up state and element X

representing the spin-down states, i.e. $\alpha_{MnMn} = \alpha_{Mn\uparrow\uparrow}$ and $\alpha_{MnX} = \alpha_{Mn\uparrow\downarrow}$. The received W-C parameters can be found in Table 5.1 and their visualisation can be seen in Figure 5.2 with spin-up being the red arrows and spin-down yellow, the crystallographic direction [0 0 1] is shown as the black arrow. There were no constraints implemented on magnetic moments. Lastly, the non-spin-polarised calculations were done as well for full reference.

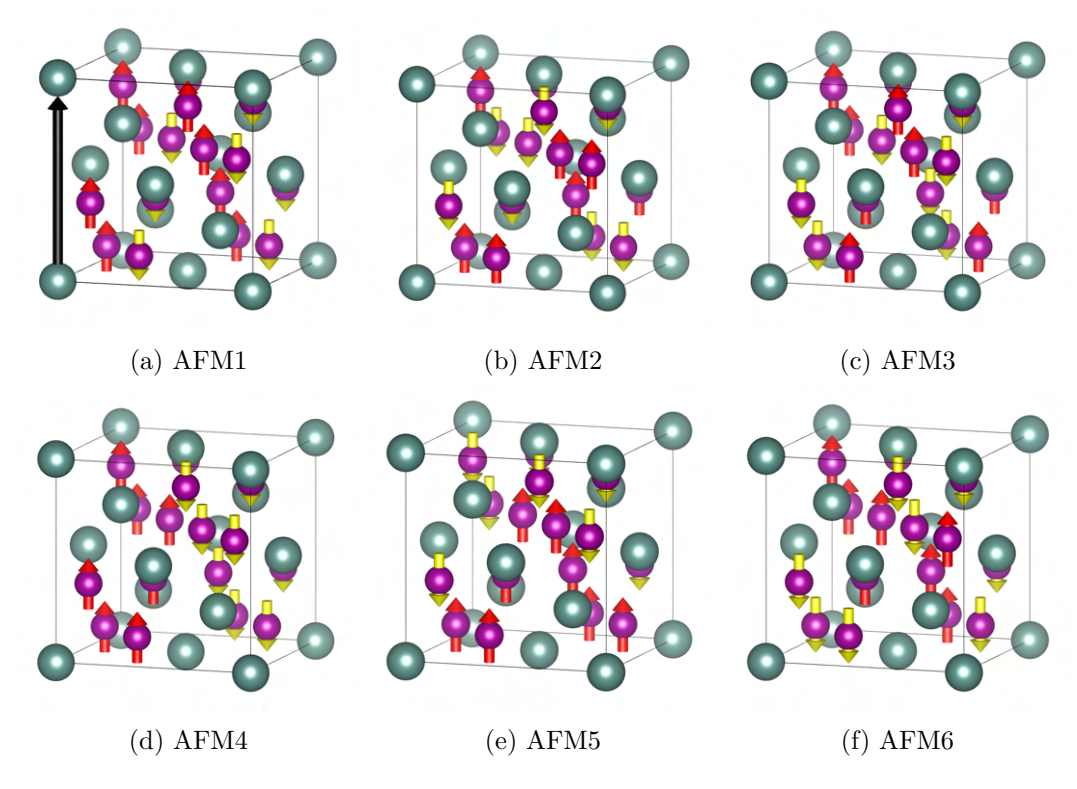


Figure 5.2: Different antiferromagnetic orderings used for YMn₂ calculations, purple atoms are Mn, turquoise atoms are Y, black vector highlights the [0 0 1] crystallographic direction.

| Magnetic ordering | 1st NN | | 2nd NN | | 3rd NN | |
|-------------------|---------------------------------|-------------------------------|---------------------------------|-------------------------------|---------------------------------|-------------------------------|
| | $\alpha_{Mn\uparrow\downarrow}$ | $\alpha_{Mn\uparrow\uparrow}$ | $\alpha_{Mn\uparrow\downarrow}$ | $\alpha_{Mn\uparrow\uparrow}$ | $\alpha_{Mn\uparrow\downarrow}$ | $\alpha_{Mn\uparrow\uparrow}$ |
| AFM1 | -0.333 | 0.667 | -0.333 | 0.667 | 1.000 | 0.000 |
| AFM2 | -0.333 | 0.667 | 0.333 | 0.333 | -0.333 | 0.667 |
| AFM3 | -0.333 | 0.667 | 0.333 | 0.333 | -0.333 | 0.667 |
| AFM4 | 0.333 | 0.333 | -0.333 | 0.667 | -0.333 | 0.667 |
| AFM5 | 0.167 | 0.417 | -0.333 | 0.667 | 0.000 | 0.500 |
| AFM6 | 0.000 | 0.500 | 0.000 | 0.500 | -0.333 | 0.667 |

Table 5.1: Warren-Cowley parameters for different magnetic orderings.

For metaGGA calculations, the pure α -Mn was calculated as well to validate the results of [19]. For this, the conventional unit cell containing 58 Mn atoms was used. The α -Mn crystallizes in $I\overline{4}3m$ space group. Furthermore, there are 4 different magnetic sublattices making the mangetic structure quite complicated, magnetic structure I is nearly antiferromagnetic in the [0 0 1] direction on the corners of the cell and on the middle atom, II which is mostly antiferromagnetic in [0 0 1] direction but the spins are canted, III is divided into

IIIa and IIIb and is mostly oriented in the (0 0 1) plane and IV, which is also divided into IVa and IVb. All of these can be seen on a Figure 5.3.

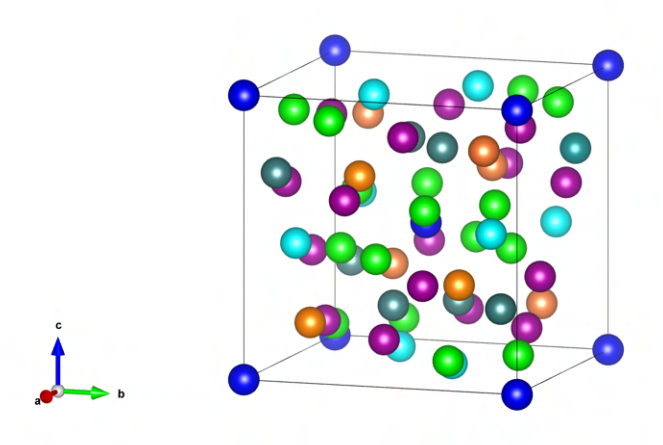


Figure 5.3: The α -Mn crystal lattice with the magnetic sublattices differentiated by colours, dark blue is the I, orange is the II, light blue and purple are the IIIa and IIIb respectively and finally, dark green and dark blue are the IVa and IVb sublattices.

5.2.2 GGA calculations

The PAW PBE [84, 85] functionals were used as they gave same accuracy as the PAW PBEsol [30] but the calculations were faster. Other considered functionals were the LDA and GGA PW91. The cutoff energy was set to 500 eV. The integration over Brillouin zone was done on a k-point mesh of 7x7x7 [86]. The magnetic moments were computed firstly as collinear and then as non-collinear with spin-orbit coupling enabled. Switch to non-collinear calculations was done after the collinear calculations failed in recognizing the AFM2 and AFM3 as the same, more on this further in the results. The spin-orbit coupling was then enabled because of the information in [102] which describes spin-orbit coupling as strong in this material because of high received susceptibility from nuclear magnetic resonance and neutron scattering.

To compare the stabilities of the different magnetic orderings, the energy-volume curves were calculated with range of volume $300\,\text{Å}^3-520\,\text{Å}^3$. Afterwards, the results were fitted with Birch-Murnaghan equation of states (EOS) of 4th order by the means of the Gibbs2 code [116, 117]. Magnetic moments were analysed from the VASP output files (OUTCAR). To get the equillibrium values of magnetic moments a static calculation was then run again for the minimum received from energy-volume curves.

5.2.3 Meta-GGA calculations

Multiple functionals were chosen as possibilities for the calculations, starting from SCAN functional because of its ability to correctly describe magnetism in α -Mn [19], it was of interest to use its deorbitalized version SCAN-L as well [34]. Then the family of R²SCAN and its two different deorbitalized versions, R2SCAN-L and OFR2 [32, 118]. The Tao-Mo functionals were also considered with their deorbitalized versions [119].

Firstly, pure α -Mn was calculated via SCAN functional to validate the successful description on our hardware/software combination and to observe behaviour of different settings. Afterwards, the other functionals were run as well. The initial magnetic moments were set just ferromagnetic in the [0 0 1] direction to observe the functionals ability to find the correct magnetic state. If it failed an approximate antiferromagnetic ordering was set to help the functional find the correct state. This was done because sometimes the optimization algorithm can miss antiferromagnetic solutions if initial ferromagnetism is set [8]. Full relaxation was allowed (ISIF = 3) with the convergence criterion for forces being 10^{-4} eV/Å. The Methfessel-Paxton [6, 7] smearing method was used with the parameter SIGMA = 0.2. Planewave cutoff was set to 550 eV as in the works of Pulkkinen et al. [19]. Non-collinear magnetic description is a necessity as well as the spin-orbit coupling. It is preferable to turn off symmetry (ISYM = 0) for the first few steps as it helps with performance of these calculations. It has to be mentioned these calculations were very computationally costly and after consulting the HPC support (at the IT4I supercomputing centre) the SCALAPACK package usage was turned off for calculations on supercomputer Karolína (LSCALAPACK = .FALSE.). Even then, the calculations on supercomputer Karolína had to be run on 32 nodes with quite low cpus per node (32) as the memory usage was enormous. Setting up the kpoints was also quite a struggle as the settings used by Pulkkinen et al. [19] were over our computational possibilities. We first started with the kpoint mesh of 8x8x8 (the first run still with symmetry enabled) which worked fine until the magnetic symmetry breaking multiplied the number of irreducible kpoints. This resulted in a memory bottleneck and the mesh had to be reduced to 6x6x6 which still results in 216 irreducible kpoints. Later calculations were run on LUMI supercomputer, which has higher memory per node, which allowed much more efficient calculations but the settings were kept the same to keep comparability, except the usage of SCALAPACK, which was enabled again. All the necessary settings mentioned in section Section 3.1.2 were also enabled (LASPH = .TRUE. and LMIXTAU = .TRUE.). Additionally, the pure Yttrium in hcp lattice was calculated with the successful functionals to obtain mixing enthalpy.

The YMn₂ calculations were run with the same functionals as the α -Mn to see if there is any difference between ability to correctly describe Mn and this Mn rich compound. They were again run on both IT4I Karolína HPC and LUMI HPC. Same settings as for pure Mn were used except for few. The energy cutoff was set to 600 eV and the kpoints were this time controlled via the KSPACING setting, which was set to 0.12 Å⁻¹. The use of symmetry was turned on again, as there should not be any huge break of symmetry that the calculation would benefit from, if we consider just antiferromagnetism as possible solution. The computational cost was again higher than for GGA but it was nowhere near the pure Mn calculations. The results were just structural optimizations, not energy - volume curves, as that would still be too computationally expensive. At this point we were interested if any of the metaGGA functionals would change the energy balance obtained by GGA or result in any of the experimentally observed orderings as the most stable. As the computational resources were running out, the workflow changed into doing just structure optimizations of AFM1, AFM2 and AFM7 structure.

5.3 Results

5.3.1 GGA results

Collinear calculations

The results from collinear calculations can be seen in Figure 5.4. It can be seen that AFM1 and AFM3 have very similar energies. Most importantly, the AFM2 and the non-spin-polarised NM calculations are basically equal for all GGA calculations. The magnetic moments for AFM2 were also reduced to zero thus the whole calculation was acting as non-magnetic. As was mentioned in the methods (Section 5.2.1) the AFM2 and AFM3 are equal structures and since VASP does not input any axis into collinear calculation, just takes the difference between spin-up and spin-down electron densities [8], this shows a failure in description of this system. It is probably caused by the spin-orbit coupling not being included and thus the switch to non-collinear calculations has to be made. Surprisingly, the lattice parameters and magnetic moments for AFM1 and AFM3 were very similar to the experimental ones.

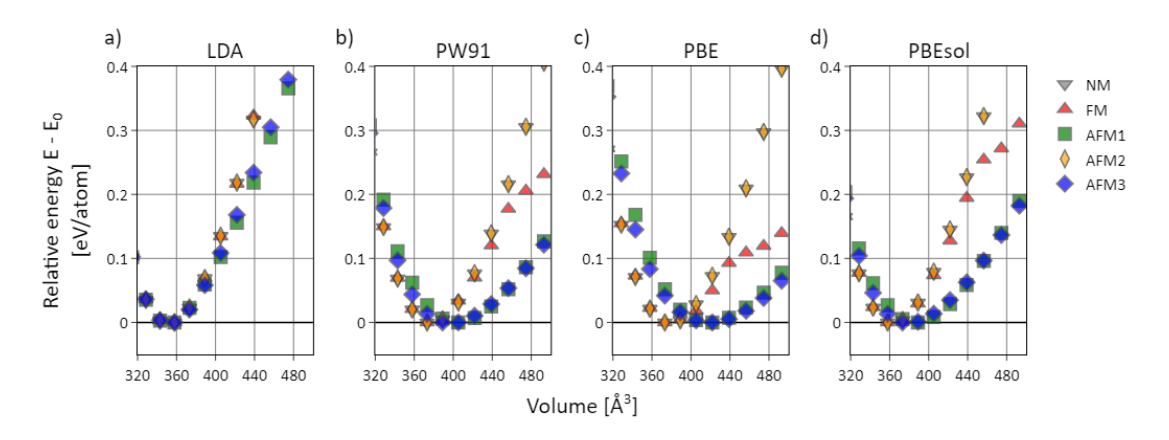


Figure 5.4: Results from collinear calculations.

Non-collinear calculations

The resulting energy-volume curves show the AFM1 ordering as the most stable. Slightly less stable were AFM2 and AFM3 which resulted in basically equal energetics and volumes between each other and were also just 0.014 eV higher than AFM1 with their equillibrium volume lower by just 0.309 Å^3 , i. e. lattice parameter difference of 0.002 Å. All of these results in about 3 % difference from experimental measured lattice parameter of 7.73 Å [16, 120] showing PBE potential slightly overestimating the lattice parameter for this compound. The other generated AFM structures had quite different results. Even though their equillibrium energy is quite similar to AFM2 and AFM3, their equillibrium volumes result in much smaller values. Biggest difference was for AFM4 where the equillibrium volume was smaller by 15.458 Å^3 . The non-spin-polarised calculation results in a smaller volume by 39.0375 Å^3 , which equals to around 9.35 % volume difference. That value is too high compared to the experimentally observed difference of 5 %.

The ferromagnetic ordering had an interesting effect in its energy volume curve around $450\,\text{Å}^3$ (7.663 Å) which corresponds to around 2.710 Å in Mn - Mn interatomic distance.

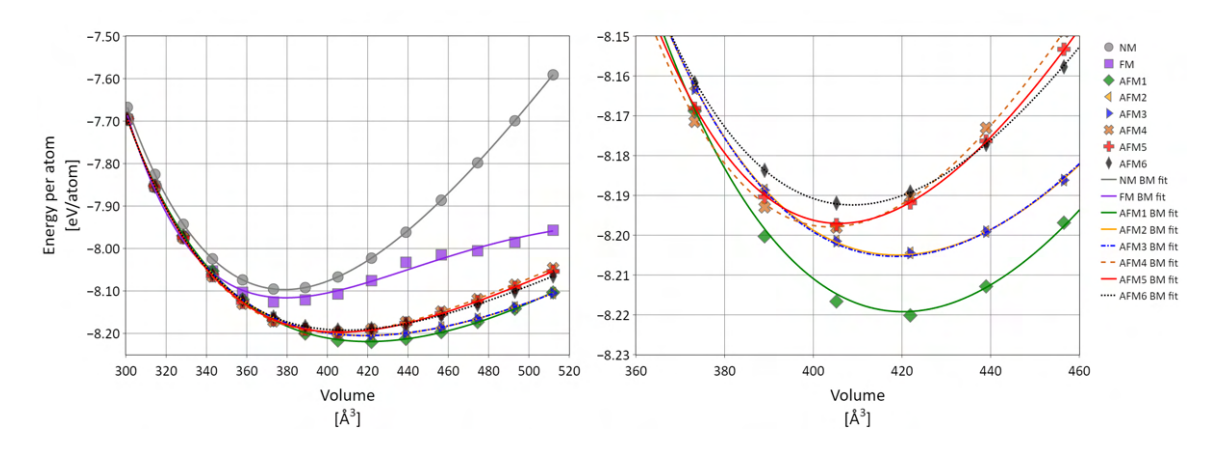


Figure 5.5: YMn₂ energy-volume curves with Birch-Murnaghan equation of states fit.

According to Voiron and Wada et al. [121, 122] there is a critical value of Mn - Mn interatomic distance in rare-earth RMn₂ compounds of around 2.7 Å above which the Mn retains its large magnetic moment while below it collapses. This would be in agreement with our results. This instability has caused the Birch-Murnaghan fit to be quite unreliable as it could not deal with such a change in curvature. All results from the fit can be found in Table 5.2. Comparing the equillibrium volumes and energies from gained results shows a hint of a trend of decreased equillibrium volume with increased randomness of magnetic moments for the AFM calculation Figure 5.6. The smallest obtained volume was for ordering AFM4 which had the highest W-C parameters for both same spin and opposite spin Mn atoms in 1st NN. This structure had the magnetic moments in one way in one half of the cell and the other half had them in the other way as can be seen in Figure 5.2d. The ordering AFM6 with the most random distribution of opposite spin Mn atoms had a slightly higher volume as well as lower stability compared to other AFM orderings. Percentage difference of volume between this structure and AFM1 would be 2.28 % which still does not equal to the experimentally measured difference between the AFM and NM state but it is much closer than taking the non-spin-polarised state as the paramagnetic state. This could hint at the possible necessity of using a completely random order of magnetic moments to model the paramagnetic state.

| Magnetic | Equilibrium energy per atom | Equilibrium volume | Lattice parameter | Bulk Modulus | Average magnetic moment in [0 0 1] |
|----------|-----------------------------------|--------------------|----------------------|-----------------|---------------------------------------|
| ordering | eV/atom | $ {A}^3$ | Å | GPa | μ_B |
| AFM1 | -8.22 | 417.41 | 7.47 | 60.22 | 2.57 |
| AFM2 | -8.20 | 417.10 | 7.47 | 51.05 | 2.54 |
| AFM3 | -8.20 | 417.70 | 7.48 | 52.12 | 2.55 |
| AFM4 | -8.20 | 401.95 | 7.38 | 75.16 | 2.07 |
| AFM5 | -8.20 | 404.58 | 7.40 | 70.62 | 2.15 |
| AFM6 | -8.19 | 407.88 | 7.42 | 62.42 | 2.25 |
| FM | -8.13 | 379.58 | 7.24v | 92.99 | 0.49 |
| NM | -8.10 | 378.37 | 7.23 | 140.06 | |

Table 5.2: Values from Birch-Murnaghan equation of states fit.

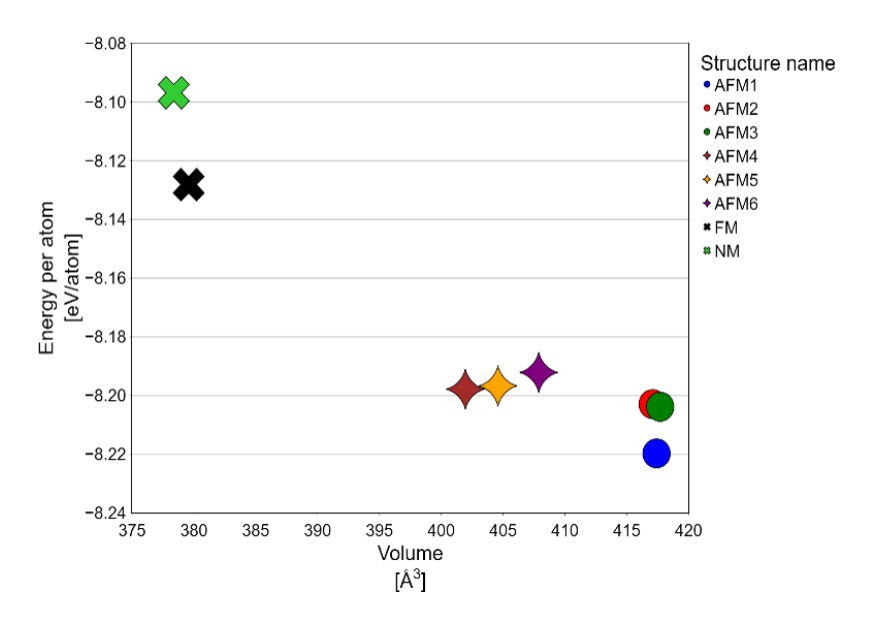


Figure 5.6: YMn₂ equillibrium energies and volumes.

The average magnetic moment values in Table 5.2 were taken in absolute values. There were 4 different sites in the unit cells with same size of magnetic moment but for some structures with different spin orientation. The received values were again in quite good agreement with previously published values of $2.7 \mu_B$, [17, 108, 115], especially considering the simulation of antiferromagnetic ordering and not the helimagnetic from which those values were reported. Absolute majority of the magnetic moment was oriented along the [0] 0 1 direction even after the relaxation with only very small parts in other two perpendicular crystallographic directions. Interestingly, there was quite a difference between AFM2 and AFM3 which were otherwise nearly the same. The AFM2 ordering results in some magnetic moment in [1 0 0] direction $(0.045 \,\mu_B)$ and no magnetic moment in [0 1 0], while the AFM3 has similar values but in both [1 0 0] and [0 1 0]. The values were quite small but it was still interesting to see a difference in what are otherwise completely the same structures. Examining the whole volume range, the magnetic moment in [0 0 1] direction was, as expected, steadily increasing with increase of volume. It appears to be saturating and the differences between structures minimise with larger volumes. Other two directions are mostly stable throughout the whole volume range except for AFM6, where, surprisingly, the moments decrease with increase of volume. There was also the interesting effect in AFM1, where some moments between $320 - 360 \,\text{Å}^3$ had values around $0.145 \,\mu_B$ in the [0 1 0 direction, with increase of volume this effect disappeared and for the equilibrium volume the values were around $0.020 \,\mu_B$.

It has to be noted though that none of the approaches currently describe the ground state observed by experiments. It may be caused by the complications of GGA functionals to describe Mn magnetic structures without the empirical U correction as the compound is still quite Mn rich. The inclusion of Y which can act as an f-electron element may even worsen this problem. Considering the results of Pulkkinen et al. [19] this sparked hope that maybe the metaGGAs could be the answer that gives the experimentally observed orderings as the ground state.

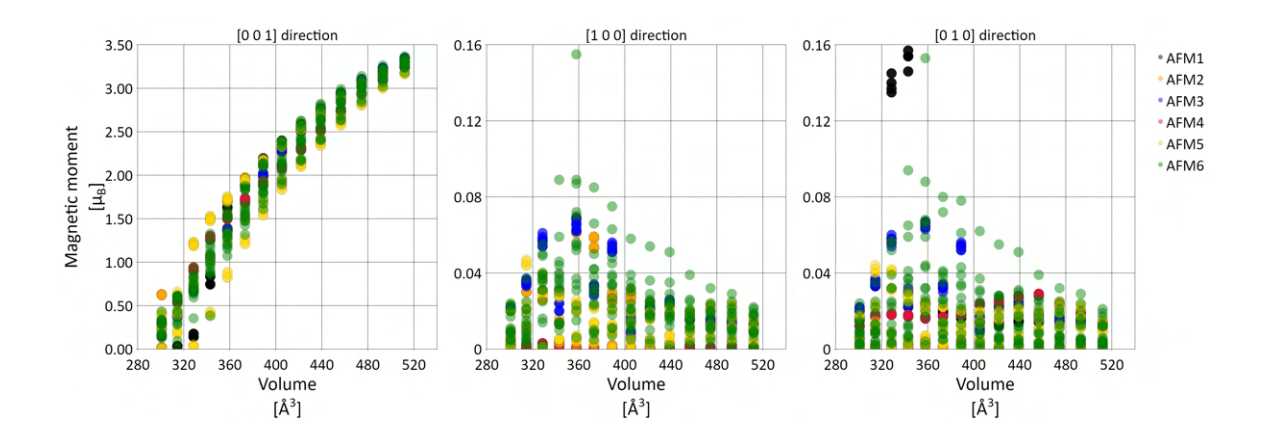


Figure 5.7: Magnetic moments dependence on volume.

5.3.2 Meta-GGA results - α -Mn

The successful α -Mn calculation were done with the SCAN and r^2 SCAN functional. SCAN functional even managed to correctly change the initial ferromagnetic ordering into the complicated antiferromagnetic structure. The r^2 SCAN was started from already an antiferromagnetic set up representing the proper sublattice positions.

Surprisingly, the deorbitalized versions of both SCAN and r²SCAN, the SCAN-L, OFR2 and r²SCAN-L, completely failed. Neither setting the initial moments as antiferromagnetic nor as the results from previous SCAN calculations helped and the calculations did not converge. Changing the algorithm to ALGO = All, the simultaneous update of all orbitals, which VASP wiki [8] mentions as possible solution to convergency problems and was used by Mejia-Rodriguéz in their work [42], did not help either. It also has to be mentioned that using this algorithm consumes further memory, so its usage for already heavily memory consuming calculation like this one is quite limited. It may be possible that with increased cutoff energy and ALGO = All the calculations would converge but the computational cost was too high. Although, one testing calculation was run with the SCAN-L and cutoff of 700 eV with the recommended algorithm but with reduced kpoints and yet the convergence was still not achieved.

5.3.3 Meta-GGA results - YMn₂

The functional performance was similar to the α -Mn. The Tao-Mo functional failed completely and the deorbitalized functionals have convergency issues for YMn₂ as well. SCAN and r²SCAN both converged for AFM1 but r²SCAN had worse computational performance as it took way longer to converge. The issues may again arise from not enough kpoints as it was found while working with these functionals on other project. r²SCAN is much more sensitive to the number of kpoints. Having α -Mn calculated via SCAN allows us to calculate the mixing enthalpy in relation to Mn ground state. With the experimentally proposed structure by [101] AFM7 exhibits the lowest mixing enthalpy of -12.28 kJ/mol.

It has to be mentioned that SCAN calculations for AFM structures result with a slight tetragonality as reported by Nakamura and Shiga [18, 104, 120] but no tetragonality is found in the non-spin-polarised calculation. The tetragonality differs between the AFM orderings and for the AFM1, it is not in the [0 0 1] direction, but in [0 1 0] direction

even though the moments are mostly oriented along the [0 0 1] direction. There are some magnetic moment in [0 1 0] direction as well, 0.022 or 0.016 μ_B in both negative and positive values. Interestingly, the AFM2 results in tetragonality in [1 0 0] direction, this time with no moments in other directions except the [0 0 1]. The AFM2 results in higher stability than AFM1 but is still not as stable as AFM7. On the other hand, the AFM7 results in tetragonality in the [0 0 1] direction as was observed in experiments. The value of tetragonality also agrees with experimental results of 0.5% [18, 104, 120] but it is in the opposite direction. Here the [0 0 1], or c lattice parameter, was reduced instead of extended. This could just be caused by the relaxation algorithm as the lattice parameter values are in near perfect agreement with experimental data. Thus the additional AFM7 exp. V calculation was performed, This calculation does nothing else than "switching" around the lattice parameters, so that the tetragonal distortion is in the correct way, i. e. extension in the [0 0 1] direction. Only internal coordinates were allowed to relax for this calculation (ISIF = 2). The resulting mixing enthalpy is slightly lower, -12.31 kJ/mol and the tetragonality is slightly extended. The magnetic moments are very similar, for the experimental volume the moments are slightly larger, which makes sense as the volume is also slightly larger, but the orientation is just in [0 0 1] direction with only extremely small parts in other two directions (in orders of 0.001 μ_B). The resulting moments for all structures are overestimated over experiment, which is worse than GGA PBE. On the other hand, it is a known behaviour of the SCAN functional [31, 40].

| Magnetic | Mixing enthalpy | Volume | a | c | a/c | Avg. magnetic moment in [0 0 1] |
|-------------|--------------------|---------------|------|------|-------|--|
| ordering | $\mathrm{kJ/mol}$ | ${\rm \AA}^3$ | Å | Å | Å | μ_B |
| AFM1 | -10.47 | 445.75 | 7.71 | 7.50 | 1.029 | 3.356 |
| AFM2 | -10.97 | 460.16 | 7.70 | 7.73 | 0.997 | 3.538 |
| AFM7 | -12.28 | 459.04 | 7.70 | 7.74 | 0.994 | 3.300 |
| AFM7 exp. V | -12.31 | 460.68 | 7.74 | 7.69 | 1.007 | 3.510 |
| NM | 41.78 | 366.64 | 7.16 | 7.16 | 1.00 | _ |

Table 5.3: Results from SCAN.

6. Goals

6.1 CoCrNi calculations

The CoCrNi calculations are finished and published in the paper [2] from Section 8.1. Further phonon calculations on selected HEA systems are planned to address their thermodynamic stability. Similar short-range ordering analysis for those systems is planned as well.

6.2 YMn₂ calculation

The plan is to try and find a dependence of the energy on the ordering of magnetic moments. Before that, the calculation of pure elements to evaluate the H_{mix} and compare it with available literature to evaluate the accuracy of the PAW PBE approach is planned. If the accuracy is insufficient then it will be necessary to use DFT + U or hybrid potentials for future calculations. The helimagnetic structure as a whole is not planned to calculate as it would require a computational cell 57 times larger than used now to represent the whole spiral, which would mean thousands of atoms. On the other hand, the double-axial spin structure can be calculated. If the PAW PBE approach will show correct mixing enthalpies, multiple calculations need to be done in ranges of $\alpha_{Mn\uparrow\uparrow}$ and $\alpha_{Mn\uparrow\downarrow}$ either generated through the sqsgenerator [49] to better represent the paramagnetic phase or hand-made to model all possible antiferromagnetic orderings. To try and explain the volume expansion non-spin-polarised phonon calculations of similar compounds will be done (for example YAl₂) to see if similar effects appear.

7. Conclusions

The main goals of this thesis were to describe the magnetism at ab initio level in the systems CoCrNi, YMn₂ and additionally, pure α -Mn. The first part of this thesis is focused on the CoCrNi system and contains not only ab initio calculations but molecular dynamics runs employing universal machine learning potential GRACE. The other part is focused on the pure α -Mn as well as the YMn₂ systems calculated via multiple different functionals. The main conclusions of the first part of the thesis are as follows:

- Ab initio calculations of the CoCrNi alloy provide unique insights into its phase stability and magnetic structure as well as the short-range ordering. It was correctly described as more stable in the spin-polarised state rather than in the non-spin-polarised state. The dependence on the short-range ordering was evaluated through calculations on multiple structures with different levels of Warren Cowley short-range order parameters. A specific ordered structures were created by hand that minimized the amount of the ordered element in 1st NN to 2, which was inspired by trying to get antiferromagnetic ordering for Cr. These Cr ordered structures result in the highest stability for both fcc and hcp structures but also minimizes the effect of including spin-polarization on phase stability. Interestingly, it was found that Ni ordering influences the phase stability of the hcp structure while having no effect on the fcc. This effect was so strong that it actually destabilized the hcp Ni ordered structure relatively to the fcc Ni structures.
- Magnetic moment analysis revealed trends that depend on 1st NN elements. Firstly, it was revealed in the Cr ordered structures that the distribution of moments is significantly different for all elements compared to the randomly ordered structures. Antiferromagnetic ordering was much more present in the fcc Cr ordered structure, caused by the Co moments flipping their spin to accommodate the Cr. Meanwhile, in the hcp Cr ordered structure the magnetic moments were reduced heavily. Further analysis of the concentration of elements in 1st NN revealed quite strong dependence on the amount of Cr for all elements. Mostly pronounced for Co, but present for all the others, the moments reduced with increased content of Cr in their 1st NN, probably caused by the inability to satisfy the antiferromagnetic magnetic structure that Cr prefers.
- Furthermore, the same analysis of 1st NN was employed on the Bader charges where even more pronounced dependencies were found. Nearly linear dependence was found charge transfer of all elements on the amount of Cr in their 1st NN. Here, the more Cr was found in 1st NN, the more charge was transferred. In case of Cr it meant more charge was given while for Ni and Co the more charge was accepted. It has to be mentioned that Co sometimes released some of its charge, which could be tied to Ni in its 1st NN. More importantly, these charge transfer values were in agreement with elements Pauling electronegativities.
- Relating the charge transfer to magnetic moment revealed quite strong dependencies as well. Thus revealing that the magnetic moment is just a result of the ongoing charge transfers dependence. The data revealed that with higher amounts of charge transfer for Co and Ni the magnetic moment decreased while for Cr it increased.

- Comparison between CHGNet universal machine learning potential to the DFT results revealed unsatisfactory results for the machine learned potential. The errors in energies, and thus mixing enthalpies, were so high that any prediction was highly unreliable. The original idea to use the CHGNet predicted forces for further phonon calculations, which require accurate forces, had to be discarded after observing the root mean squared error of 0.2 eV/Å. In regards of magnetic moment prediction the model fared better. Here it was mostly the ordered structures that proved difficult for the model to predict, otherwise the agreement was not so bad and it could be usable in initial predictions of magnetic moment sizes.
- The molecular dynamics were run with the GRACE (Graph Atomic Cluster Expansion) universal machine learning model. Its performance was quite solid in comparison to specifically trained Embedded Atom Method potential. It also predicts fcc stable above room temperatures rather than hcp. The relative difference between the two phases reveals very small differences, which is in agreement with very low stacking fault energies for this material. It was not possible to observe the annihilation of chemical short-range ordering but there was observed local distortion of the lattice at 1100 K runs so it may have been just because too short simulation time. The distortion was also different between the two structures, where in fcc it was mostly single atoms or doublets/triplets while in hcp it was bigger clusters.
- Another system that was planned to be investigated was the FeCoNi alloy but throughout PhD studies a lot of publications were already published with similar analysis that was planned. Combined with the failure of CHGNet for predicting correct forces for further phonon calculations, it was decided to not pursue this problem further.

The main conclusions of the second part, the system YMn₂ together with α -Mn:

- Total number of 7 different antiferromagnetic structures were explored. Collinear magnetic calculations failed in description of magnetic moments, so a switch to non-collinear magnetic calculations had to be made. From these energy volume curves were obtained and revealed an error of GGA PBE functional. All of the experimentally observed magnetic structures resulted in higher energies than a generated one, this structure had as much antiferromagnetic ordering as was possible. Even though, the agreements in sizes of magnetic moments to experiments was very good. But the fact that experimental structures were not the stable ones meant finding other solutions.
- One of the possible solutions would be to use a step up on the Jacobs ladder of exchange correlation functionals, the metaGGA functionals. This was prompted by a publication, in which the SCAN metaGGA functional has correctly calculated the complicated magnetic structure of α-Mn, which was previously impossible to obtain just by DFT. They have also shown that SCAN mostly reproduces the otherwise used Hubbard +U correction as well. Since the time of that publication a new version of metaGGAs was developed, the deorbitalized metaGGAs, which shown further increase in magnetic moment accuracies. This combined into this list of used metaGGA functionals: SCAN, r²SCAN, the deorbitalized versions SCAN-L, r²SCAN-L, OFR2 as well as the Tao-Mo functional.
- The chosen functionals were used for calculation of pure α -Mn as well as the YMn₂. Out of all chosen functionals, only the SCAN and r²SCAN and Tao-Mo did not

encounter convergency issues. The Tao-Mo functional resulted in unphysical zero magnetic moments, as well as extremely small volumes, so it was discarded from further calculations. The failure of deorbitalized functionals may have been caused by not enough kpoints or too low cutoff energy set, but with the computational cost of these calculations, it was not really possible to increase them, especially the number of kpoints. On the other hand, SCAN and $\rm r^2SCAN$ functionals did not only coverge, but converged into the correct complicated antiferromagnetic structures of α -Mn. With these results, it was possible to calculate the mixing enthalpy of YMn₂ in relation to the Mn ground state as well.

- The metaGGAs functionals were further reduced to just SCAN for all of the YMN₂ calculations. Reason being that $\rm r^2SCAN$ while accurate it had worse performance and with limited computational time it was critical to not use too much of it. This also meant that instead of energy volume curves just structure optimization was done on 3 magnetic structures, two experimentally observed and the AMF1 that was the most stable in GGA PBE calculations. This time though, the AFM1 was the least stable antiferromagnetic structure. The experimentally observed AFM7 resulted in lowest mixing enthalpy, as well as nearly perfect agreement of calculated volume to the experimental one. There is one caveat, the overestimation of magnetic moments by nearly 1 μ_B but it is also an expected behaviour of the functionals. Most importantly, the experimentally observed ground state was now obtained from DFT without the need for Hubbard corrections or hybrid functionals.
- The metaGGA functionals have also managed to reproduce the tetragonality observed in experiments. There was a caveat to this as well, the tetragonality value of AFM7 was nearly exact as experimental, except in the other direction, *i. e.* the [0 0 1] was compressed instead of extended. Doing a calculation on the exact experimental tetragonality while allowing only atomic coordinates relaxation results in even slightly lower mixing enthalpy. It has to be noted that the energies are very similar and the optimization that was used could struggle to find the global minimum.

The results obtained in this thesis offer some further research into their respective topics. For the CoCrNi alloy, the most interesting would be refitting the GRACE potential to improve its accuracy or running longer molecular dynamics runs to try and find the fcc-hcp phase transition, or at least the annihilation of the chemical short-range ordering. It also shows how even the out of the box version of GRACE potentials is usable for HEAs, in comparison to CHGNet for example, so one can safely use it for other HEA systems.

For the YMn₂, the anomalous thermal expansion still remains unexplained but if it is tied to the antiferromagnetic phase, this work produced the experimentally observed ground state usable for further thermal dependence calculations. One of the options could be either quasi-harmonic approximation to obtain phonon contributions, here one has to be careful to correctly represent the magnetic symmetry, which may end up in quite high amounts of displacements. Another option could be to obtain the interaction parameters from the ground state antiferromagnetic structure by constructing Wannier orbitals. These could then be fed into a spin dynamics code that employs the Landau-Lifshits-Gilbert equation like Spirit or VAMPIRE to run their simulations on multiple lattice constants to observe the behaviour.

8. Publications and other activities

8.1 Publications

- I. Moravčík, M. Zelený, A. Dlouhý, H. Hadraba, A. G. Moravčíková, P. Papež, O. Fikar, I. Dlouhý, D. Raabe, Z. Li. "Impact of interstitial elements on the stacking fault energy of an equiatomic CoCrNi medium entropy alloy: theory and experiments". Science and Technology of Advanced Materials 23.1 (2022), pp. 376–392. DOI: 10.1080/14686996.2022.2080512.
- P. Papež, M. Zelený, M. Friák, I. Dlouhý. "The effect of spin-polarization, atomic ordering and charge transfer on the stability of CoCrNi medium entropy alloy". Materials Chemistry and Physics 304.127783 (2023). DOI: 10.1016/j.matchemphys.2023.127783.
- M. Friák, O. Zobač, Z. Chlup, O. Fikar, P. Papež, M. Zelený, A. Kroupa. Materials properties of defect-stabilized off-stoichiometric τ-phase Al₂Ge₂Mg, Intermetallics, 169, 108294 (2024) DOI: 10.1016/j.intermet.2024.108294.

8.2 Other activities

8.2.1 Conferences

- DPG, Spring Meeting of the Condensed Matter Section, Regensburg, Germany, 16. 21. 3. 2025 Poster: Ab initio calculations of defects in the Mg₂Ge intermetallic., P. Papež, M. Friák, M. Zelený.
- Multiscale Materials Modeling conference, Prague, Czech Republic, 22. 27. 9. 2024
 Talk: The impact of spin-polarization, atomic ordering and charge transfer on the stability of medium-entropy CoCrNi alloy., P. Papež, M. Zelený, M. Friák, I. Dlouhý.,
- DPG Spring Meeting, Berlin, Germany, 17. 22. 3. 2024 Talk: The impact of spin-polarization, atomic ordering and charge transfer on the stability of CoCrNi alloy,
 P. Papež, M. Zelený, M. Friák and I. Dlouhý, and poster: Ab initio study of phase stability of YMn₂ with different magnetic orderings, P. Papež, M. Friák and I. Turek
- Intermetallics, Bad Staffelstein, Germany, 1. 6. 10. 2023 Poster: Competing magnetic structures in YMn₂, P. Papež, M. Friák and I. Turek
- DPG Spring Meeting, Regensburg, Germany, 4. 9. 9. 2022 poster Ab initio study of point defects in disordered systems, P. Papež, M. Friák, M. Zelený"

8.2.2 Workshops and schools

- Machine Learning for Materials Discovery workshop at Aalto University, Espoo, Finland, 5. 8. 5. 2025
- Graph Atomic Cluster Expansion (GRACE) Hands-on workshop on development, validation and application of GRACE models at Ruhr-Universität Bochum, Germany, 12. - 14. 3. 2025

- Annual MSIT Workshop International Seminar on the Evaluation of Heterogeneous Multicomponent Equilibria at Castle Ebernburg, Bad Münster, Germany 16. - 21. 1. 2025
- MSIT Winter School on Materials Chemistry aat Schloss Ringberg, Tegernsee, Germany, 21. 26. 1. 2024

8.2.3 Research stays

3. 5. 2024 - 31. 7. 2024 - Montanuniversität Leoben, Leoben, Austria

Bibliography

- J. M. D. Coey. Magnetism and Magnetic Materials. Cambridge University Press, 2010. ISBN: 9780511845000. DOI: 10.1017/CB09780511845000.
- [2] S. Blundell. *Magnetism in Condensed Matter*. Oxford University Press, 2001. ISBN: 0198505914.
- [3] Ch. Kittel. *Introduction to Solid State Physics*. Ed. by Stuart Johnson. Eight. John Wiley & Sons, Inc., 2005. ISBN: 978-0-471-41526-8.
- [4] E. B. Tadmor and R. E. Miller. *Modelling Materials*. Cambridge University Press, 2011. ISBN: 978-0-521-85698-0.
- [5] R. M. Martin. *Electronic Structure: Basic Theory and Practical Methods*. Cambridge University Press, 2004. ISBN: 0521782856.
- [6] G. Kresse and J. Furthmüller. "Efficient iterative schemes for ab initio total-energy calculations using a plane-wave basis set". In: *Physical Review B* 54.16 (1996), pp. 11169–11186. DOI: 10.1103/PhysRevB.54.11169.
- [7] G. Kresse and D. Joubert. "From ultrasoft pseudopotentials to the projector augmented-wave method". In: *Physical Review B* 59.3 (1999), pp. 1758–1775. DOI: 10.1103/PhysRevB.59.1758.
- [8] The VASP Manual VASPwiki. https://www.vasp.at/wiki/index.php/The_VASP_Manual.
- [9] B. Cantor et al. "Micorstructural development in equiatomic multicomponent alloys". In: *Materials Science and Engineering: A* 375 377 (2004), pp. 213–218. DOI: 10.1016/j.msea.2003.10.257.
- [10] J. W. Yeh et al. "Nanostructured High-Entropy Alloys with Multiple Principal Elements: Novel Alloy Design Concepts and Outcomes". In: *Advanced Engineering Materials* 6.5 (2004), pp. 299–303. DOI: 10.1002/adem.200300567.
- [11] Y. Ikeda et al. "Impact of interstitial C on phase stability and stacking-fault energy of the CrMnFeCoNi high-entropy alloy". In: *Physical Review Materials* 3.11 (2019), p. 113603. DOI: 10.1103/PhysRevMaterials.3.113603.
- [12] I. Moravčík et al. "Impact of interstitial elements on the stacking fault energy of an equiatomic CoCrNi medium entropy alloy: theory and experiments". In: Science and Technology of Advanced Materials 23.1 (2022), pp. 376–392. DOI: 10.1080/14686996.2022.2080512.
- [13] B. Cantor. "Multicomponent high-entropy Cantor alloys". In: *Progress in Materials Science* 120 (2021), p. 100754. DOI: 10.1016/j.pmatsci.2020.100754.
- [14] D. B. Miracle and O. N. Senkov. "A critical review of high entropy alloys and related concepts". In: *Acta Materialia* 122 (2017), pp. 448–511. DOI: 10.1016/j.actamat. 2016.08.081.
- [15] B. S. Murphy et al. *High-Entropy Alloys*. 2nd ed. Elsevier, Amsterdam, 2019. ISBN: 9780128160688. DOI: 10.1016/C2017-0-03317-7.
- [16] M. Shiga, H. Wada, and Y.Nakamura. "Magnetism and Thermal Expansion Anomaly of RMn₂ (R = Y, Gd, Tb, Ho and Er)". In: *Journal of Magnetism and Magnetic Materials* 31 34 (1983), pp. 119–120. DOI: 10.1016/0304-8853(83)90179-8.

- [17] Y. Nakamura, M. Shiga, and S. Kawano. "Antiferromagnetism of YMn₂ intermetallic compound". In: *Physica B* 120 (1983), pp. 212–215. DOI: 10.1016/0378-4363(83) 90376-5.
- [18] R. Cywinski, S. H. Kilcoyne, and C. A. Scott. "Magnetic order and moment stability in YMn₂". In: *Journal of Physics: Condensed Matter* 3.3 (1991), pp. 6473–6488. DOI: 10.1088/0953-8984/3/33/023.
- [19] A. Pulkkinen et al. "Coulomb correlation in noncollinear antiferromagnetic α-Mn".
 In: Physical Review B 101 (2020), p. 075115. DOI: 10.1103/PhysRevB.101.075115.
- [20] D. Hobbs, J. Hafner, and D. Spišák. "Understanding the complex metallic element Mn. I. Crystalline and noncollinear magnetic structure of α -Mn". In: *Physical Review B* 68.014407 (2003). DOI: 10.1103/PhysRevB.68.014407.
- [21] F. L. Thiemann et al. "Introduction to machine learning potentials for atomistic simulations". In: *Journal of Physics: Condensed Matter* 37 (2025), p. 073002. DOI: 10.1088/1361-648X/ad9657.
- [22] D. A. Porter, K. E. Easterling, and M. Y. Sherif. *Phase Transformations in Metals and Alloys.* 3rd ed. Tayor & Francis Group, 2014. ISBN: 978-1-4398-8357-0.
- [23] D. R. Askeland, P. P. Fulay, and W. J. Wright. The Science and Engineering of Materials. Ed. by Hilda Gowans. 6th ed. Cengage Learning, 2010. ISBN: 978-0-495-29602-7.
- [24] A. R. Paul, M. Mukherjee, and D. Singh. "A Critical Review on the Properties of Intermetallic Compounds and Their Application in Modern Manufacturing". In: Crystal Research and Technology 57.3 (2021), p. 2100159.
- [25] J. M. Cowley. "An Approximate Theory of Order in Alloys". In: *Physical Review* 77.5 (1950), pp. 669–675.
- [26] S. Curtalo et al. "AFLOW: An automatic framework for high-throughput materials discovery". In: *Computational Materials Science* 58 (2012), pp. 218–226. DOI: 10.1016/j.commatsci.2012.02.005.
- [27] S. P. Ong et al. "Python Materials Genomics (pymatgen): A Robust, Open-Source Python Library for Materials Analysis". In: *Computational Materials Science* 68 (2013), pp. 314–319. DOI: 10.1016/j.commatsci.2012.10.028.
- [28] M. Šob. Multiscale Materials Modelling: Fundamentals and Applications. Ed. by Z. X. Guo. Woodhead Publishing, 2007. ISBN: 1845690710.
- [29] J. P. Perdew and K. Schmidt. "Jacob's Ladder of Density Functional Approximations for the Exchange-Correlation Energy". In: AIP Conference Proceedings 577 (2001), pp. 1–20. DOI: 10.1063/1.1390175.
- [30] J. P. Perdew et al. "Restoring the Density-Gradient Expansion for Exchange in Solids and Surfaces". In: *Physical Review Letters* 100.13 (2009), p. 136406. DOI: 10.1103/PhysRevLett.100.136406.
- [31] J. Sun, A. Ruszinszky, and J. P. Perdew. "Strongly Constrained and Appropriately Normed Semilocal Density Functional". In: *Physical Review Letters* 115 (2015), p. 036402. DOI: 10.1103/PhysRevLett.115.036402.
- [32] J. W. Furness et al. "Accurate and Numerically Efficient r²SCAN Meta-Generalized Gradient Approximation". In: *Physical Chemistry Letters* 11 (2020), pp. 8208–8215. DOI: 10.1021/acs.jpclett.0c02405.

- [33] A. P. Bartók and J. R. Yates. "Regularized SCAN functional". In: *The Journal of Chemical Physics* 150 (2019), p. 161101. DOI: 10.1063/1.5094646.
- [34] D. Mejia-Rodriguez and S. B. Trickey. "Deorbitalization strategies for meta-generalized-gradient-approximation-exchange-correlation functionals". In: *Physical Review A* 96 (2017), p. 052512. DOI: 10.1103/PhysRevA.96.052512.
- [35] I. A. Abrikosov et al. "Recent progress in simulations of the paramagnetic state of magnetic materials". In: Current Opinion in Solid State and Materials Science 20 (2016), pp. 85–106.
- [36] A.V. Ruban and V.I. Razumovsky. "Spin-wave method for the total energy of paramagnetic state". In: *Physical Review B* 85.17 (2012), p. 174407.
- [37] B. Alling, T. Marten, and I. A. Abrikosov. "Effect of magnetic disorder and strong electron correlations on the thermodynamics of CrN". In: *Physical Review B* 82.18 (2010), p. 184430.
- [38] R. Kingsbury et al. "Performance comparison of r²SCAN and SCAN metaGGA density functionals for solid materials via an automated, high-throughput computational workflow". In: *Physical Review Materials* 6 (2022), p. 013801. DOI: 10.1103/PhysRevMaterials.6.013801.
- [39] H. Liu et al. "Assesing r²SCAN meta-GGA functional for structural parameters, cohesive energy, mechanical modulus, and thermophysical properties of 3d, 4d and 5d transition metals". In: *The Journal of Chemical Physics* 160 (2024), p. 024102. DOI: 10.1063/5.0176415.
- [40] V. Sokolovskiy et al. "Meta-GGA SCAN functional in the Prediction of Ground State Properties of Magnetic Materials: Review of the Current State". In: *Metals* 13 (2023), p. 728. DOI: /10.3390/met13040728.
- [41] F. Tran et al. "Orbital-free approximations to the kinetic-energy density in exchange-correlation MGGA functionals: Tests on solids". In: *The Journal of Chemical Physics* 149 (2018), p. 1441050. DOI: 10.1063/1.5048907.
- [42] D. Mejia-Rodriguez and S. B. Trickey. "Deorbitalized meta-GGA exchange-correlation functionals in solids". In: *Physical Review B* 98 (2018), p. 115161. DOI: 10.1103/PhysRevB.98.115161.
- [43] Y. Zhang et al. "Advances and Challenges of SCAN and r²SCAN Density Functionals in Transition-Metal-Compounds". In: Wiley Interdisciplinary Reviews: Computational Molecular Science 15 (2025), e70007. DOI: 10.1002/wcms.70007.
- [44] A. Togo et al. "Implementation strategies in phonopy and phono3py". In: J. Phys. Condens. Matter 35 (2023), p. 353001. DOI: 10.1088/1361-648X/acd831.
- [45] A. Togo. "First-principles Phonon Calculations with Phonopy and Phono3py". In: J. Phys. Soc. Jpn. 92.1 (2023), p. 012001. DOI: 10.7566/JPSJ.92.012001.
- [46] P. Borlido et al. "Exchange-correlation functionals for band gaps of solids: benchmark, reparametrization and machine learning". In: npj Computational Materials 6 (2020), p. 96. DOI: 10.1038/s41524-020-00360-0.
- [47] T. Aschebrock and S. Kümmel. "Ultranonlocality and accurate band gaps from a meta-generalized gradient approximation". In: *Physical Review Research* 1 (2019), p. 033082. DOI: 10.1103/PhysRevResearch.1.033082.

- [48] A. Zunger et al. "Special Quasirandom Structures". In: *Physical Review Letters* 65.3 (1990), pp. 353–356. DOI: 10.1103/PhysRevLett.65.353.
- [49] D. Gehringer, M. Friák, and D. Holec. "Models of configurationally-complex alloys made simple". In: Computer Physics Communications 286 (2023), p. 108664.
- [50] M. E. Tuckerman and G. J. Martyna. "Understanding Modern Molecular Dynamics: Techniques and Applications". In: *The Journal of Physical Chemistry B* 104 (2 1999), pp. 159–178. DOI: 10.1021/jp992433y.
- [51] M. P. Allen and D. J. Tildesley. *Computer Simulation of Liquids*. 2nd. Oxford University Press, 2017.
- [52] A. P. Thompson et al. "LAMMPS a flexible simulation tool for particle-based materials modeling at the atomic meso and continuum scales". In: *Computer Physics Communications* 271 (2022), p. 108171. DOI: 10.1016/j.cpc.2021.108171.
- [53] A. Stukowski. "Visualization and analysis of atomistic simulation data with OVITO—the Open Visualization Tool". In: *Modelling and Simulation in Materials Science and Engineering* 18.015012 (2009). DOI: 10.1088/0965-0393/18/1/015012.
- [54] J. Behler and M. Parinello. "Generalized neural-network representation of high-dimensional potential energy surfaces". In: *Physical Review Letters* 98 (2007), p. 146401.
 DOI: 10.1103/PhysRevLett.98.146401.
- [55] A. P. Bartók et al. "Gaussian approximation potentials: the accuracy of quantum mechanics without the electrons". In: *Physical Review Letters* 104 (2010), p. 136403. DOI: 10.1103/PhysRevLett.104.136403.
- [56] R. Jinnouchi et al. "Descriptors representing two- and three-body atomic distributions and their effects on the accuracy of machine-learned inter-atomic potentials". In: *The Journal of Chemical Physics* 152 (23 2020), p. 2341020. DOI: 10.1063/5.0009491.
- [57] R. Jinnouchi, F. Karsai, and G. Kresse. "On-The-Fly machine learning force field generation: Application to melting points". In: *Physical Review B* 100 (2019), p. 014105. DOI: 10.1103/PhysRevB.100.014105.
- [58] R. Drautz. "Atomic cluster expansion for accurate and transferable interatomic potentials". In: *Physical Review B* 99 (2019), p. 249901. DOI: 10.1103/PhysRevB.99.014104.
- [59] B. Deng et al. "CGHNet as a pretrained universal neural network potential for charge-informed atomistic modelling". In: *Nature Machine Intelligence* 5 (2023), pp. 1031–1041. DOI: 10.1038/s42256-023-00716-3.
- [60] J. Schmidt et al. "Machine-Learning-Assisted Determination of the Global Zero-Temperature Phase Diagram of Materials". In: Advanced Materials 35 (22 2023), p. 2210788. DOI: 10.1002/adma.202210788.
- [61] J. Schmidt et al. "Crystal graph attention networks for the prediction of stable materials". In: Science Advances 7 (49 2021). DOI: 10.1126/sciadv.abi7948.
- [62] Luis Barroso-Luque et al. Open Materials 2024 (OMat24) Inorganic Materials Dataset and Models. 2024. arXiv: 2410.12771 [cond-mat.mtrl-sci]. https://arxiv.org/abs/2410.12771.

- [63] P. Žguns, I. Pudza, and A. Kuzmin. "Validating Universal Machine Learning Interatomic Potentials Agaisnt Experimental EXAFS Data: Case of Layered WS₂ and MoS₂". Conference Presentation at Machine Learning for Materials Discovery 2025, Espoo, Finland.
- [64] Ilyes Batatia et al. "MACE: Higher Order Equivariant Message Passing Neural Networks for Fast and Accurate Force Fields". In: Advances in Neural Information Processing Systems. Ed. by Alice H. Oh et al. 2022. https://openreview.net/forum?id=YPpSngE-ZU.
- [65] J. Riebesell et al. "A framework to evaluate machine learning crystal stability predictions". In: Nature Machine Intelligence 7 (2025), pp. 836–847. DOI: 10.1038/s42256-025-01055-1.
- [66] A. H. Larsen et al. "The atomic simulation environment—a Python library for working with atoms". In: *Journal of Physics: Condensed Matter* 29.27 (2017), p. 273002. DOI: 10.1088/1361-648X/aa680e.
- [67] A. Bochkarev, Y. Lysogorskiy, and R. Drautz. "Graph Atomic Cluster Expansion for Semilocal Interactions beyond Equivariant Message Passing". In: *Physical Review X* 14 (2024), p. 021036. DOI: 10.1103/PhysRevX.14.021036.
- [68] M. Rinaldi et al. "Non-collinear Magnetic Atomic Cluster Expansion for Iron". In: (2023). arXiv: 2305.15137v1.
- [69] S. Zhao, G. M. Stocks, and Y. Zhang. "Stacking fault energies of face-centered cubic concentrated solid solution alloys". In: Acta Materialia 134 (2017), pp. 334–345. DOI: 10.1016/j.actamat.2017.05.001.
- [70] J. Q. Zhao et al. "FCC-to-HCP Phase Transformation in CoCrNi_x Medium-Entropy Alloys". In: Acta Metallurgica Sinica (English Letters) 33 (2020), pp. 1151–1158. DOI: 10.1007/s40195-020-01080-6.
- [71] Y. Ikeda, B. Grabowski, and F. Körmann. "Ab initio phase stabilities and mechanical properties of multicomponent alloys: A comprehensive review for high entropy alloys and compositionally complex alloys". In: *Materials Characterization* 147 (2019), pp. 464–511. DOI: 10.1016/j.matchar.2018.06.019.
- [72] Y. Y. Tan et al. "Lattice distortion and magnetic property of high entropy alloys at low temperatures". In: *Journal of Materials Science & Technology* 104 (2022), pp. 236–243. DOI: 10.1016/j.jmst.2021.07.019.
- [73] F. Walsh, M. Asta, and R. O. Ritchie. "Magnetically driven short-range order can explain anomalous masurements in CrCoNi". In: *Proceedings of the National Academy of Sciences* 118.13 (2021), e2020540118. DOI: 10.1073/pnas.2020540118.
- [74] J. Ding et al. "Tunable stacking fault energies by tailoring local chemical order in Cr-CoNi medium-entropy alloys". In: *Proceedings of the National Academy of Sciences* 115.36 (2018), pp. 8919–8924. DOI: 10.1073/pnas.1808660115.
- [75] H. S. Oh et al. "Engineering atomic-level complexity in high-entropy and complex concentrated alloys". In: *Nature Communications* 10.2090 (2019). DOI: 10.1038/s41467-019-10012-7.
- [76] R. Zhang et al. "Short-range order and its impact on the CrCoNi medium-entropy alloy". In: *Nature* 581 (2020), pp. 283–287. DOI: 10.1038/s41586-020-2275-z.

- [77] L. Zhou et al. "Atomic-scale evidence of chemical short-range order in CrCoNi medium-entropy alloy". In: *Acta Materialia* 224.117490 (2022). DOI: 10.1016/j.actamat.2021.117490.
- [78] F. X. Zhang et al. "Local Structure and Short-Range Order in a NiCoCr Solid Solution Alloy". In: *Physical Review Letters* 118.205501 (2017). DOI: 10.1103/PhysRevLett.118.205501.
- [79] G. Tang et al. "Quantifying chemical fluctuations around medium-range orders and its impact on dislocation interactions in equiatomic CrCoNi medium entropy alloy". In: *Materials & Design* 225.111572 (2023). DOI: 10.1016/j.matdes.2022.111572.
- [80] H. W. Hsiao et al. "Data-driven electron-diffraction apporach reveals local short-range ordering in CrCoNi with ordering effects". In: *Nature Communications* 13.6651 (2022). DOI: 10.1038/s41467-022-34335-0.
- [81] J. Wang et al. "Chemical medium-range order in a medium-entropy alloy". In: *Nature Communications* 13.1021 (2022). DOI: 10.1038/s41467-022-28687-w.
- [82] V. P. Bacurau et al. "Comprehensive analysis of ordering in CoCrNi and CrNi2 alloys". In: *Nature Communications* 15.7815 (2024). DOI: 10.1038/s41467-024-52018-w.
- [83] Y. Y. Tan et al. "Chemical composition dependent local lattice distortions and magnetism in high entropy alloys". In: *Intermetallics* 129.107050 (2021). DOI: 10.1016/j.intermet.2020.107050.
- [84] P. E. Blöchl, C. J Först, and J. Schimpl. "Projector augmented wave method: ab initio molecular dynamics with full wave functions". In: *Bulletin of Materials Science* 26 (2003), pp. 33–41. DOI: 10.1007/BF02712785.
- [85] J. P. Perdew, K. Burke, and M. Ernzerhof. "Generalized Gradient Approximation Made Simple". In: *Physical Review Letters* 77.18 (1997), pp. 3865–3868. DOI: 10. 1103/PhysRevLett.77.3865.
- [86] M. Methfessel and A. T. Paxton. "High-precision sampling for Brillouin-zone integration in metals". In: *Physical Review B* 40.6 (1989), pp. 3616–3621. DOI: 10.1103/PhysRevB.40.3616.
- [87] T. Bučko, J. Hafner, and J. G. Ángyán. "Geometry optimization of periodic systems using internal coordinates". In: *The Journal of Chemical Physics* 122 (2005), p. 124508.
- [88] R. F. W. Bader. Atoms in Molecules: A Quantum Theory. Oxford University Press, 1990. ISBN: 9780198558651.
- [89] M. Yu and D. R. Trinle. "Accurate and efficient algorithm for Bader charge integration". In: *The Journal of Chemical Physics* (2011).
- [90] J. W. Zwanziger. "Computation of NMR observables: Consequences of projector-augmented wave sphere overlap". In: *Solid State Nuclear Magnetic Resonance* 80 (2016), pp. 14–18.
- [91] G. Henkelman, A. Arnaldsson, and H. Jónsson. "A fast and robust algorithm for Bader decomposition of charge density". In: *Computational Materials Science* 36 (2006), pp. 354–360.
- [92] E. B. J. Wilson, J. C. Decius, and P. C. Cross. *Molecular Vibrations: The Theory of Infrared and Raman Vibrational Spectra*. McGraw-Hill, New York, 1955, 1955.

- [93] J. Baker, A. Kessi, and B. Delley. "The generation and use of delocalized internal coordinates in geometry optimization". In: *The Journal of Chemical Physics* 105 (1996), p. 192.
- [94] Ö. Farkas and H. B. Schlegel. "Methods for optiizing large molecules Part III. An improved algorithm for geometry optimization using direct inversion in the iterative subspace (GDIIS)". In: *Physical Chemistry Chemical Physics* 4 (2002), pp. 11–15.
- [95] R. Lindh et al. "On the use of a Hessian model function in molecular geometry optimizations". In: *Chemical Physics Letters* 24.4 (1995), pp. 423–428.
- [96] K. Jin et al. "Tailoring the physical properties of Ni-based single-phase equiatomic alloys by modifying the chemical complexity". In: Scientific Reports 6.20159 (2016). DOI: 10.1038/srep20159.
- [97] C. Niu et al. "Magnetically-driven phase transformation strengthening in high entropy alloys". In: *Nature Communications* 9.1363 (2018). DOI: 10.1038/s41467-018-03846-0.
- [98] K. Inoue, S. Yoshida, and N Tsuji. "Direct observation of local chemical ordering in a few nanometer range in CoCrNi medium-entropy alloy by atom probe tomography and its impact on mechanical properties". In: *Physical Review Materials* 5.085007 (2001). DOI: 10.1103/PhysRevMaterials.5.085007.
- [99] D. L. Foley et al. "Diffuse electron scattering reveals kinetic frustration as origin of order in CoCrNi medium entropy alloy". In: *Acta Materialia* 268.119753 (2024). DOI: 10.1016/j.actamat.2024.119753.
- [100] R.S Liu et al. "Calorimetric properties of C14 and C15 YMn₂ and YMn₂(H, D)₆". In: *International Journal of Hydrogen Energy* 36 (2011), pp. 2285–2290. DOI: 10. 1016/j.ijhydene.2010.11.037.
- [101] R. Ballou et al. "Helimagnetism in the Cubic Laves Phase YMn2". In: *Journal of Magnetism and Magnetic Materials* 70.1-3 (1987), pp. 129–133.
- [102] H. Nakamura and M. Shiga. "NMR and neutron scattering of the frustrated metallic compound YMn₂". In: *Journal of Alloys and Compounds* 326 (2001), pp. 157–165. DOI: 10.1016/S0925-8388(01)01250-6.
- [103] H. Yamaoka et al. "Electronic structure of YMn₂ and Y₀ \cdot 96 Lu₀ \cdot 04 Mn₂ studied by x-ray emission spectroscopy". In: *Physical Review B* 80 (2009), p. 115110. DOI: 10.1103/PhysRevB.80.115110.
- [104] Y. Nakamura. "Magnetovolume Effects in Laves Phase Intermetallic Compounds". In: Journal of Magnetism and Magnetic Materials 31 34 (1983), pp. 829–834. DOI: 10.1016/0304-8853(83)90702-3.
- [105] H. Nakada et al. "Magnetic properties and Fermi surface of YMn2". In: Journal of Magnetism and Magnetic Materials 262 (2003), pp. 374–381. DOI: 10.1016/S0304– 8853(03)00067-2.
- [106] V. Paul-Boncour et al. "Structural and magnetic phase diagram of YMn_{2-x}Fe_x(H,D)_y compounds ($5 \le y \le 5$ synthesized under high H or D gaseous pressure)". In: Journal of Alloys and Compounds 691 (2017), pp. 884–892. DOI: 10.1016/j.jallcom. 2016.08.258.

- [107] H. Sugiura et al. "High pressure studiues of YMn₂ Laves phase and its deuterides". In: Journal of Alloys and Compounds 367 (2004), pp. 230–234. DOI: 10.1016/j.jallcom.2003.08.043.
- [108] X. Q. Chen an W. Wolf, R. Podloucky, and P. Rogl. "Density functional study of structural and phase stabilities of RMn₂ Laves phases (R = Sc, Y, Lu, Ti, Zr, Hf)". In: Journal of Alloys and Compounds 383 (2004), pp. 228–231. DOI: 10.1016/j.jallcom.2004.04.066.
- [109] R. Ballou, E. Lelievre-Berna, and B Fák. "Spin Fluctuations in $(Y_0 \cdot 97 \, \text{Sc}_0 \cdot 03) \, \text{Mn}_2$: A Geometrically Frustrated, Nearly Antiferromagnetic, Itinerant Electron system". In: *Physical Review Letters* 76.12 (1996), pp. 2125–2128. DOI: 10.1103/PhysRevLett. 76.2125.
- [110] E. Gratz et al. "Anomalous thermal expansion in YMn_2 , Y_6Mn_{23} and YMn_{12} ". In: *Physica B* 237 238 (1997), pp. 474–475. DOI: 10.1016/S0921-4526(97)00160-9.
- [111] H. Shen et al. "AB₂-type rare earth-based compounds with C-15 structure: Looking for reversible hydrogen storage materials". In: *Journal of Rare Earths* 42 (2024), pp. 803–816. DOI: 10.1016/j.jre.2023.09.004.
- [112] M. Pajda et al. "First-principles calculations of the magnetic properties of YMn₂ and its hydrides". In: *Journal of Physics: Condensed Matter* 8 (1996), pp. 3373–3384. DOI: 10.1088/0953-8984/8/19/012.
- [113] H. Fujii, M. Saga, and T. Okamoto. "Magnetic, crystallographic and hydrogen absorption properties of YMn₂ and ZrMn₂ hydrides". In: *Journal of the Less-Common Metals* 130 (1987), pp. 25–31. DOI: 10.1016/0022-5088(87)90083-X.
- [114] H. Figiel et al. "Hydrogen induced phase transitions in YMn₂". In: Journal of Alloys and Compounds 274 (1998), pp. 29–37. DOI: 10.1016/S0925-8388(98)00566-0.
- [115] S. Iwasaki et al. "First-principles calculations of YMn₂". In: Journal of the Physical Society of Japan 81 (2012), SB032. DOI: 10.1143/JPSJS.81SB.SB032.
- [116] A. Otero-de-la-Roza and Victor Luaña. "Gibbs2: A new version of the quasi-harmonic model code. I. Robust treatment of the static data". In: Computer Physics Communications 182.8 (2011), pp. 1708–1720. DOI: 10.1016/j.cpc.2011.04.016.
- [117] A. Otero-de-la-Roza, D. Abbasi-Peréz, and Victor Luaña. "Gibbs2: A new version of the quasiharmonic model code. II. Models for solid-state thermodynamics, features and implementation". In: *Computer Physics Communications* 182.10 (2011), pp. 2232–2248. DOI: 10.1016/j.cpc.2011.05.009.
- [118] A. D. Kaplan and J. P. Perdew. "Laplacian-level meta-generalized gradient approximation for solid and liquid metals". In: *Physical Review Materials* 6 (2022), p. 083803. DOI: 10.1103/PhysRevMaterials.6.083803.
- [119] J. Tao and Y. Mo. "Accurate Semilocal Density Functional for Condensed-Matter Physics and Quantum Chemistry". In: *Physical Review Letters* 117 (2016), p. 073001. DOI: 10.1103/PhysRevLett.117.073001.
- [120] I. Y. Gaidukova et al. "On the nature of the phase transition in YMn₂". In: *Journal of Magnetism and Magnetic Materials* 72 (3 1988), pp. 357–359. DOI: 10.1016/0304-8853(88)90234-X.
- [121] J. Voiron et al. "Magnetism instability under pressure in RMn₂ compounds". In: Journal of Applied Physics 69.8 (1991), pp. 5678–5679.

[122] H. Wada et al. "Stability of Mn moments and spin fluctuations in RMn_2 (R:Rare earth)". In: Journal of Magnetism and Magnetic Materials 70 (1987), pp. 134–136. DOI: 10.1016/0304-8853(87)90380-5.